Experimental study of multi-gigabit copper data communication over surface wave links

Ilana Toledano

Department of Engineering
University of Cambridge

The dissertation is submitted for the degree of
Doctor of Philosophy

Murray Edwards College 20 July 2021

Declaration

I hereby declare that except where specific reference is made to the work of others, the contents of this dissertation are original and have not been submitted in whole or in part for consideration for any other degree or qualification in this, or any other university. This dissertation is my own work and contains nothing which is the outcome of work done in collaboration with others, except as specified in the text and Acknowledgements. This dissertation contains fewer than 65,000 words including appendices, bibliography, footnotes, tables and equations and has fewer than 150 figures.

Ilana Toledano
July 2021

Acknowledgements

To begin with, I would like to thank my supervisor Dr Michael Crisp who guided me throughout the research. Their knowledge, motivation and patience have given me true interest in the topic and thrive to keep the research going. I could not have asked for a better advisor for my doctorate study.
Apart from my main supervisor, I would like to express my gratitude to Prof. Ian White, my former PhD supervisor, and Prof. Richard Penty who have both given me great insights and expertise in my research.
I would also like to acknowledge those individuals who participated in my research project with whom we had very regular meetings during the first lockdown and allowed me to progress my research throughout the pandemic. I am grateful for all their advice on my results, work direction and publications.
I particularly remember my fellow labmates with whom I have shared countless tea and coffee breaks without which I would not have had such an amazing time in my research group. They have made my work environment so welcoming, allowing ample opportunities to support each other.
I am also grateful to the IPES (Integrated Photonics and Electronic Systems) CDT for funding my MRes and my PhD and allowing me to start my research career, meet my PhD supervisors and building a true interest within a research community from monthly seminars to social events. As well as my College, Murray Edwards which has been a home to me throughout my PhD, it has been a true pleasure to be a part of this wonderful college, and its MCR where I have made many encounters and friends which have supported me as fellow PhD students.
And most of all, I am grateful to my parents, siblings, friends and particularly my boyfriend who have supported me from even before I started the PhD and encouraged me in this journey. They gave me enough moral support, joy, encouragement and motivation to accomplish my personal goals.

Abstract

With increasing data throughput requirements, copper network access over twisted pairs is reaching data rate limitations. Fibre-to-premises deployment is however much slower, costly and time consuming than previously anticipated [1].

In the following research, we are exploring the potential of using surface wave mode transmission over existing cable networks, which may allow a significant increase in data rates whilst keeping the installation time and cost low. A characterisation of surface wave transmission was carried in comparison with the widely deployed G.fast standard.

Surface waves, derived by Arnold Sommerfeld, have been defined as a low attenuation, low dispersion and very wideband electromagnetic mode transmission.

In order to test surface waves' potential, a proof-of-concept experimental setup was built. The setup consisted in data generation and processing, surface wave launchers design as well as choosing the wired link (in this case DW11 cable). Several experimental transmission parameters were investigated such as the modulation, equalisation, bandwidth and carrier frequency with the aim of achieving high data throughput.

Furthermore, capacity models were built to predict surface wave transmission performance in various scenarios. Because of the lab dimension restrictions, a novel surface wave capacity calculation was developed to estimate data rates over an extrapolated channel response (using two length experimental responses), and obtain longer link realistic capacity estimates.

Data rates of over 12 Gb/s were experimentally demonstrated on a 6.1 m DW11 surface wave link, with a BER of 2.25 $\times 10^{-5}$, the signal was an OFDM modulated 64QAM transmission with 2080 MHz bandwidth and 2.1 GHz carrier frequency.

In the extrapolation simulation, a DW11 surface wave link of 100 m predicted up to 14 Gb/s and at 50 m up to 35 Gb/s for high modulation and bandwidth transmission.

Compared to the G.fast data rates (up to 2 Gb/s up to 50 m) [2], the results obtained tend to indicate that surface wave communications may have potential for future twisted pair access network technologies.

Contents

List of Figures

List of Tables

1 Introduction

Fibre-to-the-Premises/Home (FTTP/H) was announced to cover millions of UK premises before 2020, however the numbers and deadlines failed to meet the expectations [55]. Indeed, fast fibre to the domicile is an increasingly more attractive idea for the population, due to the exponential demand in internet traffic with IOT (connected devices), cloud storages, 5G and to the development of Terabit data rates.

Providers quickly realised that installing optical fibre to locations with already existing equipment was not only very expensive but also more demanding in terms of time and labour than initially planned [1].

Currently the fastest and most reliable telecommunication medium is the optical fibre. This is due to its low attenuation over a wide band and high frequencies (optical domain), allowing long ranges and high data throughputs. As well as a very secure communication (optical signals cannot be detected without breaking the fibre) and high resistance from electromagnetic or radio frequency interference. At the end of many Ethernet connections there is still a “last-mile” of older and slower copper links, as the red lines show in figure 1. While being slower and having higher attenuation, these links remain the cheapest delivery type and have the added benefit of already being installed.

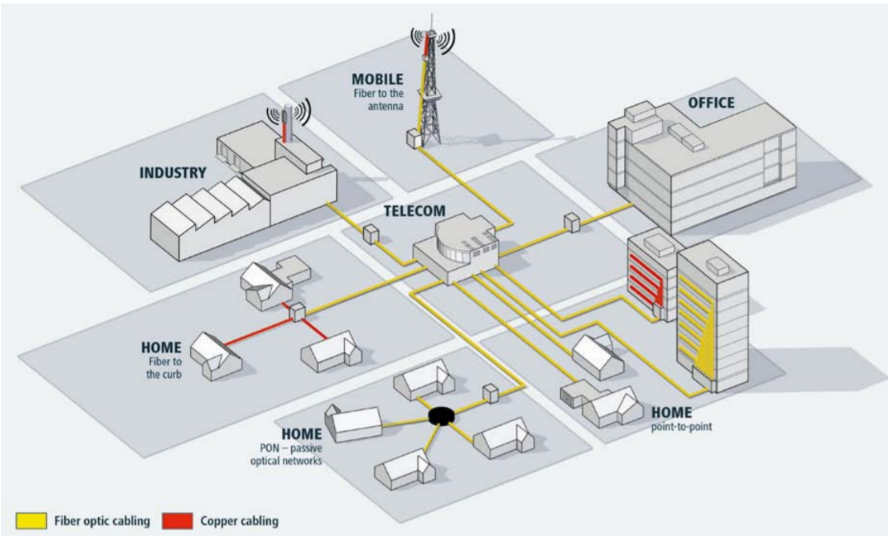

Figure 1: Internet link delivery types (Fibre vs Copper) [3]

The majority of copper connections currently linking domestic properties to the internet are twisted pair wire bundles. High speed data is transmitted to a distribution point through the fibre network known as FTTdp (fibre to the distribution point), which is located either in the street or in the underground of large buildings. Their distance is in the order of 500 to 100 metres away from the premises and is getting shorter with time [2].

Originally Ethernet connection was through coaxial cables, and from 1984 migrated to twisted pair lines, which evolved both in structure and available bit rate (throughput) throughout the years [56].

The current solutions to transmit broadband signals via copper cables are either ADSL2+ or VDSL2, which respectively deliver rates of 25 Mb/s up to 1 km and up to 200 Mb/s for lengths below 300 m. These values correspond to downstream data rates (upstream rates are lower). Beyond theses distances the data rates decrease with the available power and therefore reach similar throughputs as older standards [57] [58] [59]. Due to the decrease in copper link employment and the resulting excess capacity, techniques with wider bandwidths and higher data rates have been utilised, such as ITU-T G.fast which was deployed in 2016 [60]. G.fast operates over a 106 or 212 MHz band rather than up to 35 MHz for VDSL, and supports data rates of up to 200 Mb/s for 500 m coverage and 2 Gb/s for 100 m [59].

In order to access such data rates new installations are required in each distribution point with twisted pair already linked to the premises. These installations are less costly and time consuming than installing underground fibre links to each premise.

Even though G.fast was a jump from the previous technologies, it still struggles to get close to fibre speeds (currently up to 10 Gb/s but upgradable to 50 Gb/s) and unlike fibre communications, highly reduces with longer lengths [2]. The data rate is mostly limited by the operating bandwidth as DSL (Digital Subscriber Line) has increasing loss with frequency, resulting in a low channel power to crosstalk level ratio even with the use of vectoring [2].

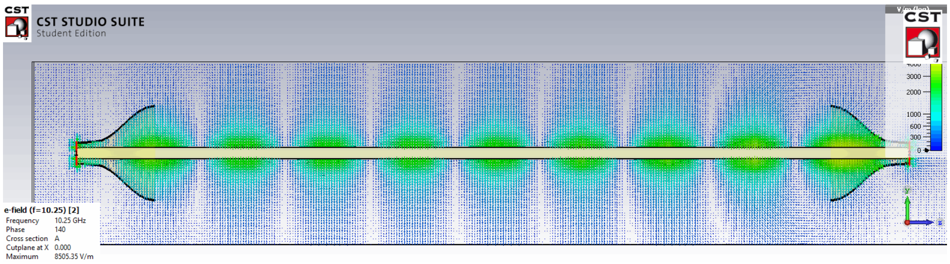

Figure 2: Surface wave electric field simulation over a single copper wire (CST Microwave)

A possible solution would come from a technology which was derived over a century ago: Sommerfeld waves [61]. It was later extended by Goubau and can also be called a surface wave (SW). It is defined as a “guided wave propagation on cylindrical conductors such as copper, aluminium, or stainless steel” and “has been found to provide low attenuation, moderate field extent, and high power-handling capability at millimetre and terahertz wavelengths” [62]. The wave is actually guided on the conductor-to-dielectric interface and its field propagates in the TM_{01} mode.

At the time of the Goubau model extension in 1950, surface waves were already of interest for television broadcasting [63]. However, equipment was limited in frequency hence being affected by the setup bulkiness and the extent of the SW field.

Rather than using the conventional transmission line mode, surface waves can be launched as waveguide modes on the surface of existing twisted pairs infrastructures (unshielded cables).

Surface wave modes have been defined as low attenuation transmissions and therefore have the potential of very large bandwidths even at high frequencies and increase the current bit rate over existing Ethernet copper links. Due to the structure of twisted pairs, one of their basic property is their ”immunity” to electromagnetic (EM) field interference, simultaneous data transmission of DSL and surface waves could even be attempted.

Prior to the start of the project, two industries had already investigated in exploiting surface waves for telecommunications In 2017, from Prof. Cioffi (ASSIA) suggested that surface waves, using existing pairs as waveguides, could reach Terabit DSL on the milimetre to sub-milimitre wavelengths [64]. The technique for such high transmission rate would be vectoring, exciting one propagation mode on each wire which itself excites other modes using the symmetry of the wire (in the bundle), vectoring would use the crosstalk from one mode to another to reconstruct the tranmsitted signal. Using this method, data rates of 1 Tb/s have been predicted for 100 m links and, 100 and 10 Gb/s for 300 and 500 metres [11].

Another company, AT&T, have oriented their research towards high speed wireless delivery with a project called “AirGig” [65]. To do so they are exploiting the ubiquitous outdoor power cables as surface wave transmission media by adding antennas over them and transmitting high speed internet and possibly use relays as Wi-Fi antenna hotspots. Since the early 2010s they have continuously registered patents and updated them on this technology [66].

As is suggested from these two initial industrial approaches, surface wave modes can also have other applications and transmission media. As shown in figure 1, many other parts of the access network is composed of copper cabling. But similar to AT&T’s work, they could also be launched on non twisted pair (TP) wires such as either outdoor or even indoor power cables.

Other possible applications in telecommunications would then be data centres, distributed antenna systems (DAS), small cell networks, 5G etc. Since copper wires are ubiquitous they have a high potential for low cost propagation.

Besides data communications, surfaces waves have been used for shorter length THz applications, such as THz biosensing [67] [29]. They have lower attenuation than free wave and allow characterisation at higher frequency ranges.

All of these experiments established further understanding of surface waves over ranges of sub GHz to THz frequencies.

Surface waves however include a few drawbacks due to their physical properties:
- a large radial propagation of the lateral field (affecting signal crosstalk and security)
- high losses at bends (difficult to plan for already existing cabling networks)
- little readily available TM_{01} mode launching technology.

All of which are frequency dependent and can be adapted when designing for specific situations.

In this thesis, we aim to provide insights into the propagation behaviour of surface waves for data communications considering a single twisted pair cable link, with a focus on frequency generation, data modulation and processing techniques. A proof-of-concept single input single output (SISO) surface wave transmission system was built in order to explore the capabilities and capacity of surface wave transmission modes as a data communication system for G.fast and DSL upgrade. We aimed at looking at data rate limits and the reach of the link looking at various frequency ranges, bandwidths, modulations and other data generations parameters primarily through experiments and when limited by setup devices (or characteristics), through simulations.

In order to fit the application requirements, the link would be required to operate over 50-200 m lengths, demonstrate similar or higher rates compared to G.fast standard and fit within official regulations such as power and crosstalk. Furthermore, a specific cable structure was chosen, BT's drop wire 11 (DW11), consisting of a single twisted pair and 3 steel strength members [40].

By the end of the first year, this PhD was part of a collaboration with BT, Huawei, Cambridge University's Department of Physics and Department of Astrophysics. Some of the research scope and applications were defined by the industrial collaborators. Experimental results were shared throughout the collaboration for feedback and improvement. Any work that was produced either by other members of the research group or the research project will be mentioned clearly in the thesis.

Our focus on this project was on the data generation and processing of experimental surface wave links and on the capacity estimates. As the PhD started before the project collaboration, a few elements of the system had been studied and designed to build an experimental setup and early capacity models (including the Sommerfeld and Goubau analytical models and launcher design).

Along with the thesis writing two papers were written to explain the theoretical and the experimental side of the project, the latter describes the OFDM data transmission over the 6.1 m DW11 cable and capacity extrapolations. Furthermore, a comparative study between surface wave and differential mode data transmission was submitted as a conference paper (this work took place as a continuation of the PhD research).

– I. Toledano, S. Bukhari, A. Aziz, E. Dinc, T. Schaich, D. Molnar, A. Al Rawi, E. de Lera Acedo, M. Crisp, R. Penty, "Experimental demonstration of multigigabit data communication using surface wave on twisted pair cables", IEEE Transactions on Communications – Submitted

– T. Schaich, E. Dinc, D. Molnar, S. Bukhari, M. Drolia, A. Aziz, I. Toledano, T. Morsman, F. Burton, A. Al Rawi, M. Crisp, E. de Lera Acedo, R. Penty, M. Payne, "Surface Wave Stop Bands in Twisted Pair Cables", IEEE Transactions on Microwave Theory and Techniques – Submitted

– I. Toledano, A. Aziz, M. Crisp, R. Penty, "Comparison of surface wave with differential mode transmission for potential broadband wired data communications", IEEE International Conference on Communications 2022 – Submitted

The thesis will be outlined as follows.

Chapter 2 will cover surface wave theory, and the background theory for surface wave data transmission. The first part will go through the numerical model of both Sommerfeld wave and Goubau line with simulated response against frequency and wire characteristics. Some extensions of the model were extrapolated to represent parameters of interest.

A deeper overview of the existing data transmission media and standard will be covered as a comparison basis and basis for the presented transmission system. Furthermore, the existing surface wave transmission solution introduced in this chapter will be detailed further as a state of the art of the research topic.

Background theory will then be outlined for data transmission techniques such as modulation, carrier frequency, upsampling or equalisation, with a strong focus on the data generation and processing used in the experiments.

Chapter 3 will present the full system overview approach of the thesis with a general SW transmission system diagram outlining the main components of the setup.

Each of these components are then reviewed with the relevant literature designs and results. These components include the surface wave mode launcher and the wire link; the latter being a requirement in the project scheme. A good understanding of previous results will bring a better understanding of expected results from such a complex structure. A presentation of the DW11 cable will be given as well as its response using surface wave mode propagation.

The last part of the experimental system is the data generation and detection. The solution presentation was linked together with the various setups overview and technical specification of the devices used. Furthermore, some experimental link response characteristics will be presented throughout the chapter with their respective system component.

Chapter 4 will be introducing the capacity calculation using three capacity estimation methods. Each method will give a different precision of data rate calculation for surface wave links. Starting with the absolute maximum Shannon capacity using the modelled surface wave attenuation results and its extension using closer to experiment noise level and attenuation values.

The third model will present and make use of water-filling algorithm to predict close to reality data rates and total power with a high control on input parameters and including measured channel responses.

Chapter 5 will present the results of the surface wave data transmission experiments; it will be divided in two parts. Experiments using a wideband QAM data generation, with various link designs: planar, single wire line and DW11 cable until a certain limit was reached. The second set of experiment focussed on OFDM data transmission. In this part, the link will consist of a 6 m DW11 line aiming to achieve maximum data rates with up to 12.5 Gb/s with transmission using several modulation orders, carrier frequencies and lengths.

Chapter 6 will be building from both chapter 4 and 5's work in order to extrapolate surface wave data transmission results to longer lengths and get closer to the application scenario. From this simulation, further estimations will be drawn on the effect of bit loading, power budget, bandwidth, length and carrier frequencies on the output data rate and transmit power.

Finally, a discussion on the research's future work will be given, driven by the results drawn throughout the thesis and the project aims described earlier in this chapter. The thesis will then be concluded, summarising the outputs of the surface wave transmission system from the thesis, both in comparison with results obtained in surface wave theory and with the existing access solution, G.fast.

2 Surface wave theory and literature review

Foremost, it is necessary to understand what surface waves and their physical properties are. In brief, they are a specific solution to Maxwell's equations, in a cylindrical geometry.

Therefore, a reminder of Maxwell's equations in their differential form is given below:

Gauss' law

$$\nabla.\mathbf{E} = \frac{p}{\varepsilon_0} \tag{1}$$

Gauss' law for magnetism

$$\nabla.\mathbf{B} = 0 \tag{2}$$

Maxwell-Faraday equation

$$\nabla \times \mathbf{E} = -\frac{\partial \mathbf{B}}{\partial t} \tag{3}$$

Ampere's circuital law

$$\nabla \times \mathbf{B} = \mu_0 \mathbf{J} + \mu_0 \varepsilon_0 \frac{\partial \mathbf{E}}{\partial t} \tag{4}$$

Maxwell's equations are a summary of all the theory linking electric and magnetic fields, including voltage, current, geometry and materials involved. With $\mathbf{E}$ the electric field (V/m), p the volume charge density (C/m^3), ε_0 the electric permittivity of free space (F/m), $\mathbf{B}$ the magnetic flux density (T), μ_0 the magnetic permeability of free space (H/m), $\mathbf{J}$ the electric current density (A/m^2) and t the time (s).

2.1 Surface waves definition

In 1899 Arnold Sommerfeld derived a solution for the Maxwell's equations in a circular/cylindrical geometry: the Sommerfeld wave.

Its particularity is its very low attenuation due to the single propagation of the TM_{01} mode and other higher order modes being almost immediately attenuated after the launch of the wave. Another name for it is the surface wave.

However it can sometimes be mistaken for other types of surface waves such as Zenneck waves which need a ground plane. A good comparision of these different waves can be found in [68].

Later on, this solution was extended to slightly different geometries where the wire surface was modified and the frequency range was increased. Firstly, the basic model from the 1899 paper will be explained in detailed equations and plots, using contemporary standard units and computation techniques for more accurate results. From then, the extended system will be covered in a similar manner.

2.1.1 Sommerfeld wave

A specific symmetry is required for Sommerfeld waves: an infinitely long cylindrical conductor of radius a and finite conductivity σ embedded in an infinite homogeneous dielectric, in this case air. The coordinate system is shown in figure 3 with the 3 electromagnetic field components, the direction of propagation z and the radial axes x and y.

For a radially symmetric transverse magnetic wave travelling along a cylinder, the fields are as follows, with ρ the radial distance:

$$\begin{aligned} E_z &= A Z_0(\gamma\rho) e^{j(\omega t - hz)} \\ E_\rho &= jA\frac{h}{\gamma} Z_1(\gamma\rho) e^{j(\omega t - hz)} \\ H_\phi &= jA\frac{k^2}{\omega\mu\gamma} Z_1(\gamma\rho) e^{j(\omega t - hz)} \end{aligned} \tag{5}$$

With h the propagation constant of the guided wave, ω the angular frequency, t the time and k the free wave propagation constant defined as:

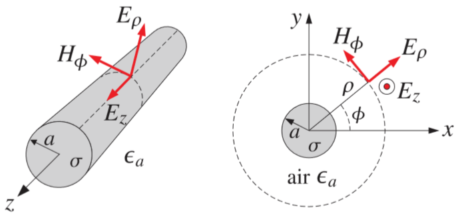

Figure 3: Cylindrical coordinates of the Sommerfeld wire [4]

$$k = \omega(\epsilon\mu)^{1/2} \quad \& \quad k_c = (\omega\sigma_c\mu_c)^{1/2}e^{-j\pi/4} \tag{6}$$

The subscript c refers to the inside of the conductor, and the material parameters are: ϵ the permittivity (or dielectric constant) in F/m, μ the permeability in H/m and σ the conductivity in S/m. The field parameters γ and γ_c seen in equation 2.1.1, are defined as:

$$\gamma^2 = k^2 - h^2 \quad \& \quad \gamma_c = k_c^2 - h^2 \tag{7}$$

$$\varepsilon_c = 1 - j\frac{\sigma}{\omega\epsilon_0} \approx 1 \quad \& \quad \varepsilon_a = 1 \tag{8}$$

The cylinder functions Z_0 and Z_1 are equal to the Bessel functions J_0 and J_1 inside the conductor and to the Hankel functions $H_0^{(1)}$ and $H_1^{(1)}$ outside the wire.

As the tangential fields must be continuous between the two media, a boundary condition at $\rho = a$ is applied, the fields E_z and H_Φ must stay constant (from conductor to air) and so should their ratio.

$$\mu\frac{\gamma}{k^2}\frac{H_0^{(1)}}{H_1^{(1)}} = \mu_c\frac{\gamma_c}{k_c^2}\frac{J_0}{J_1} \tag{9}$$

As computational capabilities have evolved since Goubau and King and Wiltse, Bessel and Hankel functions can now be solved numerically through mathematical software such as MATLAB and the argument γ can then be found through iteration:

Step 1: equate γ to its defined value with initial $h = 0.9k$ this approximation is flexible but should lay around the value of γ:

$$\gamma = \sqrt{k^2 - h^2} \tag{10}$$

Step 2: beginning of the iteration, with n the count of iterations:

$$\gamma_c = \sqrt{k^2(\varepsilon_c - 1) + \gamma_n^2}$$

$$\gamma_{n+1} = \frac{H_0^{(1)}(\gamma_n a)}{H_1^{(1)}(\gamma_n a)}\frac{\gamma_c}{\varepsilon_c}\frac{J_0(\gamma_c a)}{J_1(\gamma_c a)} \tag{11}$$

A limit is set as the difference between γ_n and γ_{n+1} which terminates the iteration process.

With γ calculated for all frequencies, h can now be obtained, it holds the system characterisation data: α the attenuation in dB/m and ν_{ph} the phase velocity in m/s, but is usually expressed as a function of the speed of light c_0.

$$\nu_{ph} = \omega/Re(h) \tag{12}$$

$$\alpha_{(dB/m)} = -8.686 \times Im(h) \tag{13}$$

Figure 4 and 5 represent α and ν_{ph} for different wire radii using the method outlined above. Looking at the plots, Sommerfeld wave attenuation increases with increasing frequency and decreasing wire diameter. However the numbers are still very low for conductor attenuation in the THz range, indeed, about 1 dB/m at 1 THz for the 1 mm radius copper wire.

As for the phase velocity it is very close to the speed of light, with all values within 99 %, and it gets even closer to c_0 as the frequency increases.

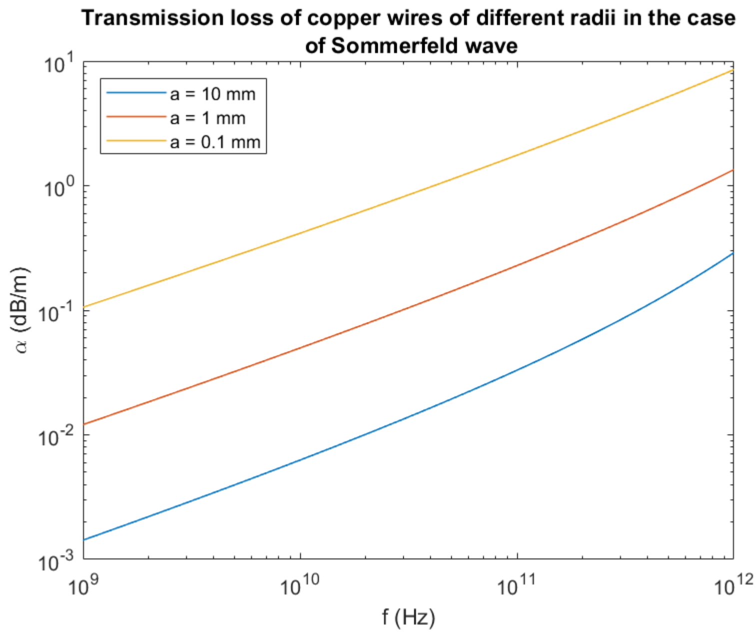

Figure 4: Sommerfeld wave attenuation α in dB/m over copper wires

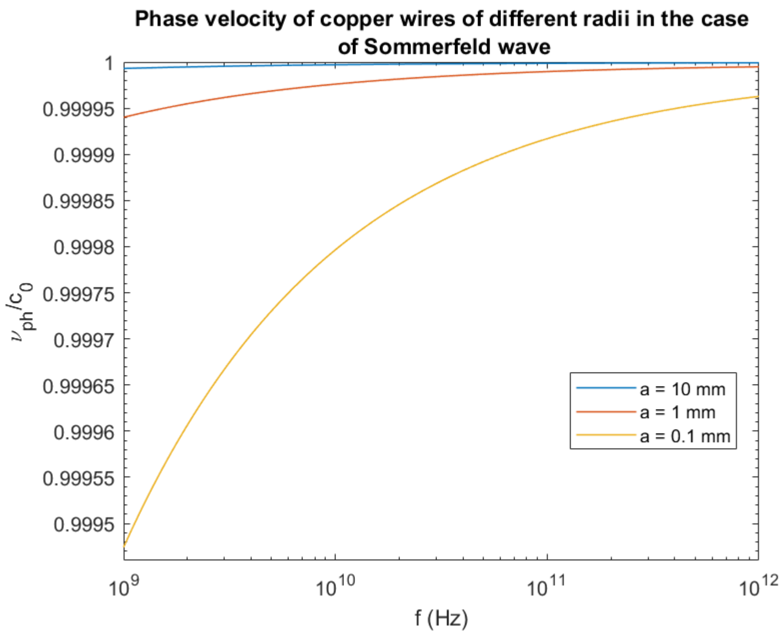

Figure 5: Sommerfeld wave phase velocity ν_{ph} in terms of c_0 over copper wires

The radial field propagation is characterised by the E_z component, and E_z can be defined as:

$$E_z(\rho) = \frac{J_0(\gamma_c \rho)}{J_0(\gamma_c a)} \ , \qquad \rho \leqslant a \tag{14}$$

$$E_z(\rho) = \frac{H_0^{(1)}(\gamma_n \rho)}{H_0^{(1)}(\gamma_n a)} \ , \qquad \rho \geqslant a \tag{15}$$

As before, at $\rho =$ a, equation (14) and (15) must be equal; we then normalise $E_z = 1$ at this point.

With a known γ over the chosen frequency range, the radial power of the Sommerfeld wave can be calculated.

The radius from which a defined amount of power $0 \leq P_{outside} \leq 1$ of the total radial power is propagated can be found by equating $E_z(\rho \geqslant a)$ to the value of interest and calculating ρ for which:

$$\mid E_z(\rho) \mid - P_{outside} = \left| \frac{H_0^{(1)}(\gamma_n \rho)}{H_0^{(1)}(\gamma_n a)} \right| - (1 - P_{inside}) = 0 \tag{16}$$

Here E_z expresses the field outside of the radius ρ, therefore to calculate power is contained within ρ, E_z has to be equated to how much power is left outside the radius $(1 - P_{inside})$.

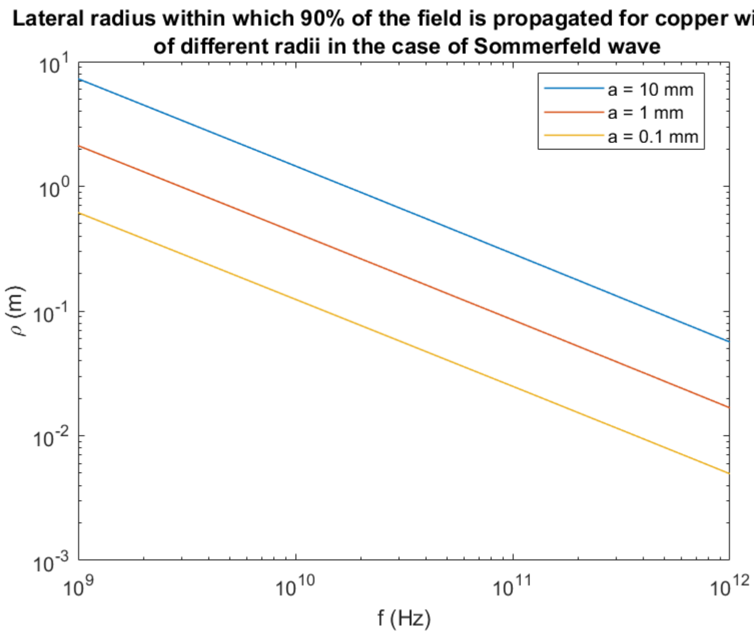

Figure 6: Sommerfeld wave E=90% radial distance ρ over copper wires

From the figure 6, the field extent decreases with decreasing wire radius and increasing frequency.

In fact, the lateral field extent is one of the biggest issues in Sommerfeld wave propagation. For example in data transmission, it can be assumed that minimal cross talk would happen within the outer 10% of the transmitted wave; however, for a 1 mm radius copper wire, this distance is about 2 metres at 1 GHz and 10 cm at 100 GHz, which remains impractically large for some scenarios.

2.1.2 Goubau line

In order to reduce the field extent whilst keeping the advantages of Sommerfeld wave propagation, research was oriented towards modifying the wire structure at its surface. In 1950, Georg Goubau treated the case of modified surface wire with very good outcomes and in particular for the dielectric coated metal wire [69] (earlier investigated by Harms [70]), the latter have therefore taken the name of Goubau lines or G-lines.

The main effect of the dielectric coat is to reduce the phase velocity and the field extension. However it created some new boundary conditions which at the time required approximations. Two major models were published: Goubau's lower frequency approximations [69] and King & Wiltse's high frequency model [71]. The equations covered in this report were based on a more recent model, using numerical methods presented in Orfanidis' book *Electromagnetic Waves and Antennas* [4].

The symmetry is once again cylindrical, it is represented in figure 7. In this model, new assumptions were made: the dielectric layer is thin compared to the wire radius or is equivalent to the wire radius but both are very small compared to wavelength, also the metal has an infinite conductivity and the dielectric is lossless.

The EM fields remain the same in the Goubau line as in the Sommerfeld wave, therefore equation 2.1.1 is still valid, but the constant A is replaced by E_0. In this symmetry, the components Z_0 and Z_1

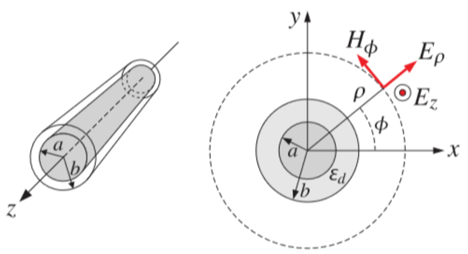

Figure 7: Cylindrical coordinates of the Goubau line [4]

are now dependent on the medium the field propagates in; the subscript a represents the air, and i the dielectric (insulator).

Within the air they are equal to Hankel functions but the field parameter, γ_a is a positive purely imaginary number, so:

$$\begin{aligned} \gamma_a = j\gamma \Rightarrow \gamma_a^2 = h^2 - k^2 \\ Z_0 = H_0^{(1)}(j\gamma\rho) \\ Z_1 = H_1^{(1)}(j\gamma\rho) \end{aligned} \tag{17}$$

Within the dielectric they become the following, with Y the Neumann function:

$$\begin{aligned} Z_0(\gamma_i\rho) = J_0(\gamma_i\rho) + BY_0(\gamma_i\rho) \\ Z_1(\gamma_i\rho) = J_1(\gamma_i\rho) + BY_1(\gamma_i\rho) \end{aligned} \tag{18}$$

And since E_z vanishes at the surface of a perfect conductor, b can be calculated:

$$E_z(a) = 0 \Rightarrow 0 = Z_0(\gamma_i a) = J_0(\gamma_i a) + BY_0(\gamma_i a) \Rightarrow B = -\frac{J_0(\gamma_i)}{Y_0(\gamma_i a)} \tag{19}$$

The E_z over H_ϕ ratio once again has to satisfy the boundary condition, so when $\rho = b$:

$$\frac{\gamma_i}{\varepsilon_i}\frac{Z_0(\gamma_i b)}{Z_1(\gamma_i b)} = \frac{-\gamma}{\varepsilon_a}\frac{H_0^{(1)}(j\gamma b)}{H_1^{(1)}(j\gamma b)} \tag{20}$$

Rearranging the previous equation, then looking back at the expressions for γ and γ_i, and seeing as $\varepsilon_a = 1$, a new function $F(h)$ can be defined:

$$\begin{aligned} F(h) \equiv \frac{\gamma}{\gamma_i} = -\frac{1}{\varepsilon_i}\frac{H_1^{(1)}(j\gamma b)}{H_0^{(1)}(j\gamma b)}\frac{Z_0(\gamma_i b)}{Z_1(\gamma_i b)} \\ \Rightarrow F^2(h) = \frac{\gamma^2}{\gamma_i^2} = \frac{h^2 - k^2}{k^2\varepsilon_i - h^2} \end{aligned} \tag{21}$$

So similar to Sommerfeld's uncoated wires, an iteration can be used to obtain the propagation constant h, and consequently the attenuation and phase velocity.

Step 1: Initialise $h = 0.9k\sqrt{\varepsilon_i}$ and set a relaxation parameter r, with $0 < r \leqslant 1$, which will set how much of the previous iteration h value will influence the next one. (Simulations have been run to verify the impact of the value of r on h which was very low; however the lower the r the further in frequency domain accurate results can be obtained)

Step 2: Rearrange equation (2.1.2) to get h_{n+1}, with n the iteration constant, and weigh the iteration with r. Once again a limit is set so that when $h_{n+1} - h_n$ is lower than the limit, the iteration stops.

$$h_{n+1} = r\,k\sqrt{\frac{1 + \varepsilon_i F^2(h_n)}{1 + F^2(h_n)}} + (1 - r)h_n \tag{22}$$

The phase velocity is derived from h using equation (12) as before and is displayed in figure 8. The phase velocity is much slower than in the previous case, however the values are still close to the velocity

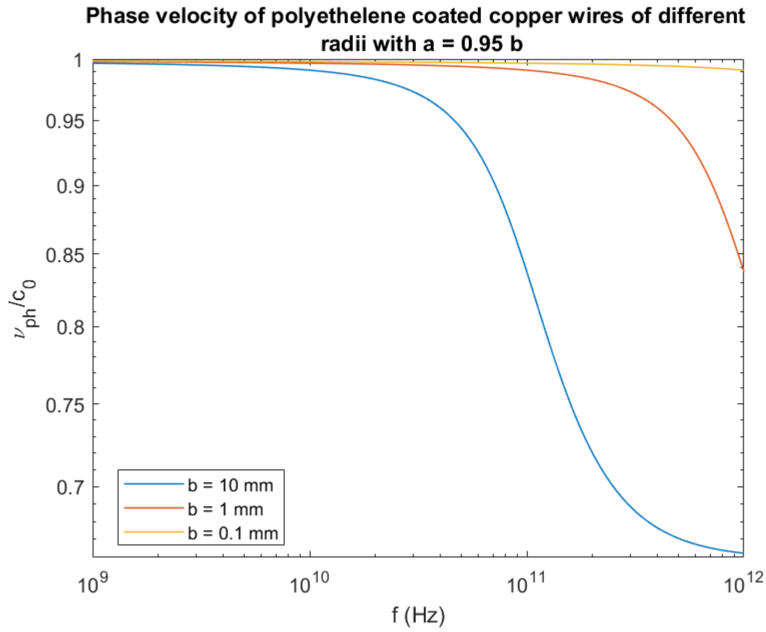

Figure 8: Goubau line phase velocity ν_{ph} in terms of c_0 (with $\varepsilon_r = 2.3$ and $tand\delta = 0.0005$)

of light, all values above are 0.65 c_0. The phase velocity decreases with increasing wire radius and frequency, which is opposite to what was seen in the bare wire case.

Again using equation (13), the attenuation can be calculated. However, this value only considers the characteristics of the dielectric and air media, so in order to get the attenuation for the overall link, Orfanidis [4] has derived a new form of King and Wiltse's [71] approximation for α in dB/m (valid for high frequencies).

$$\alpha_{dB/m} = 8.69 \times \frac{k}{2h\eta_0} . \frac{\frac{R_s}{a} + \frac{\eta_0 tan\delta}{2k\varepsilon_i} ln\left(\frac{b}{a}\right) h^2}{\frac{1}{\varepsilon_i} ln\left(\frac{b}{a}\right) + \frac{1}{2\gamma b}} \tag{23}$$

With R_s the impedance of the conductor surface and $tan\delta$ the loss tangent of the dielectric.

$$R_s = \sqrt{\frac{\omega\mu_0}{2\sigma}} \quad \& \quad \eta_0 = \sqrt{\frac{\mu_0}{\varepsilon_0}} \tag{24}$$

Figure 9 shows the exact formula for the attenuation with no frequency dependent approximations on the Bessel components. The derivation for this formula is available in [4], as well as a comparative plot for the King & Wiltse attenuation. The attenuation once again increases with increasing frequency, and even though the values are quite similar to the Sommerfeld attenuation at GHz frequencies, it worsens towards THz frequencies, with about 10 to 100 times the Sommerfeld attenuation at 1 THz (depending on the wire radius). The attenuation to wire radius relationship changes along the frequency range due to Bessel functions, hence higher diameter changing its trend earlier than the thinner wires. Lower frequencies would follow the Goubau approximations and higher frequencies would follow the King and Wiltse ones.

In the same manner as the previous part, the lateral field extent (the restricting factor for applications of Sommerfeld waves) can be calculated with the sum of field E_z in the dielectric coating and the the air (as it is 0 in the perfect conductor), for the chosen contained power ratio (here 90 %) within the calculated radius.

For lower frequencies, the field extent exponentially decreases with increasing frequency as shown by a straight line on a logarithmic scale. Then above a certain frequency, the field extent stays constant; indeed due to the lower field extent for Goubau lines, it reaches the radius of the cable itself within the displayed frequency range, and therefore the minimum field propagation possible. Consequently, wider wires reach this minima at lower frequencies than thinner ones. Until that point, the wire radius has little effect when the a/b ratio is fixed.

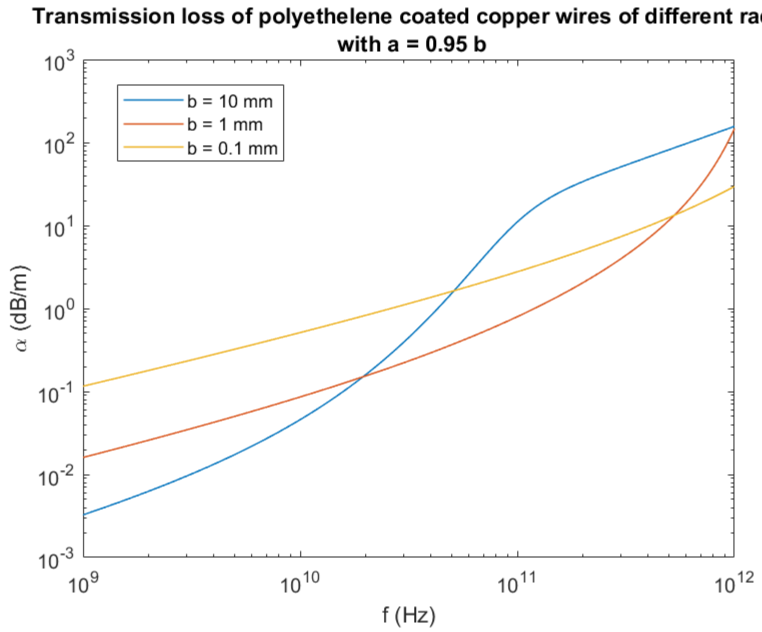

Figure 9: Goubau line wave attenuation α in dB/m

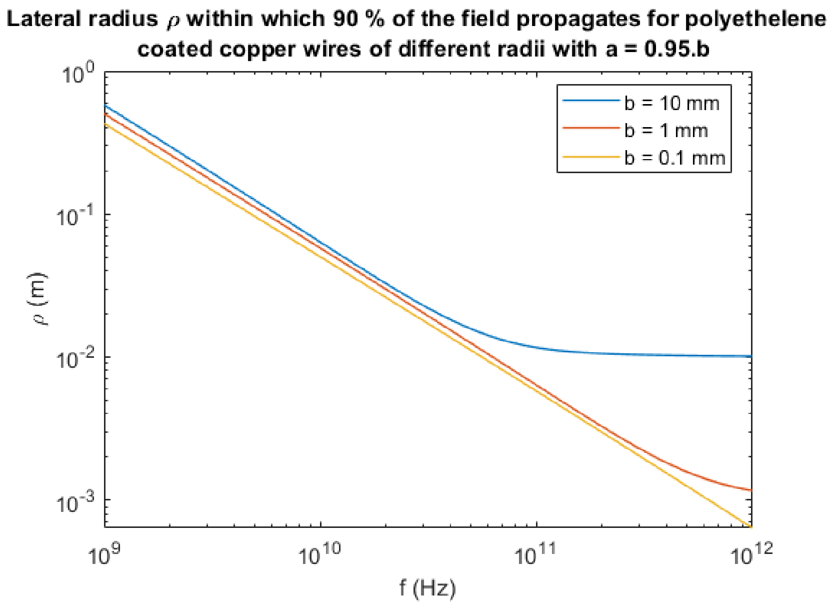

Figure 10: Goubau line lateral wave propagation $E_z = 90\%$ radius ρ in m

From these two mathematical definitions of surface waves, many parameters can be represented and explored in different forms. Much research has been carried on the different aspects of surface waves and their use in many applications. The rest of the thesis will cover this research and try to define the needs of surface waves applied to telecommunication systems.

2.1.3 Signal velocities and effect of the dielectric coating

One of the advantages often mentioned when using Sommerfeld waves in the frame of telecommunications is their low dispersion. This means that it keeps the pulses closer to their original shape and therefore limits the possibility of intersymbol interference (ISI). Dispersion can easily be derived from the earlier calculated phase velocity as follows.

The phase velocity can be defined as the velocity of the carrier wave, so if a point is fixed on the carrier wave its position change within each envelope will show a delay: the phase delay. The group velocity is more important for signal characterisation as it is the velocity of transmitted information; it relates to a group delay which is the time difference of a specific point of the carrier wave from one modulated wave to the next one (the modulation also represents the envelope of the carrier wave). They are both illustrated in figure 11.

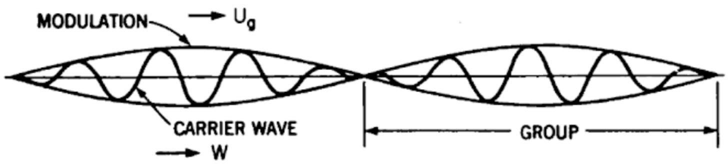

Figure 11: Signal transmission over carrier frequency representation for phase and group velocity definition [5]

Carrier and then modulation signals can be defined by the following two equations, with h the propagation constant or wavenumber as defined in Sommerfeld theory:

$$V = V_0 e^{j(\omega t - hz)} \tag{25}$$

$$V = V_0 cos(\omega t) + V_0 \frac{m}{2} \left[cos((\omega + \Delta\omega)t) + cos((\omega - \Delta\omega)t)\right] \tag{26}$$

The phase shift θ due to a length of cable d is then expressed below, and rearrangement can be made to calculate the phase delay τ_{ph} or the phase velocity ν_{ph} (in m/s) thereafter.

$$\theta = hd = \frac{\omega}{\nu_{ph}} d = \omega \tau_{ph} \tag{27}$$

The group velocity ν_{gr} (in m/s) over a distance d travelled relates to the group delay τ_{gr} by:

$$\tau_{gr} = \frac{d}{\nu_{gr}} = \frac{\partial h}{\partial \omega} d \tag{28}$$

When analysing the signal received, what will really be noticeable is the dispersion. When the phase and group velocities are not equal, it creates a delay between the modulated signal and the carrier wave; this will induce a spread of the pulse signal in time domain resulting in a distorted signal transmission and possibly intersymbol interference (ISI), this effect is illustrated in figure 12. The dispersion, D, is expressed in ps/(nm.km) and derived from the group delay as follows:

$$D = \frac{1}{d} \frac{\partial \tau_{gr}}{\partial \lambda} \tag{29}$$

Another way to express the dispersion is through the group velocity dispersion (GVD) which is the differential of the group delay in terms of angular frequency ω instead of the wavelength λ and is expressed in fs^2.

Alternatively, these parameters can be calculated from the complex S-parameters with the following expressions:

$$\tau_{ph} = -\frac{arg(S_{21})}{\omega}$$

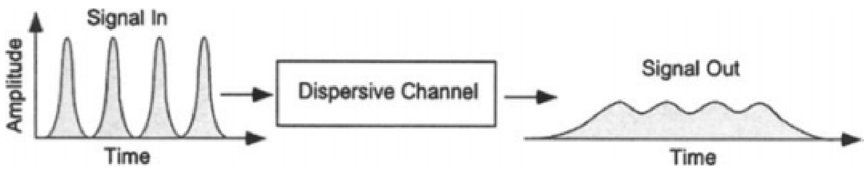

Figure 12: Effect of a dispersive channel on a stream of pulses from [6]

$$\tau_{gr} = -\frac{\partial(arg(S_{21}))}{\partial\omega} \tag{30}$$

These equations were applied to the Sommerfeld and Goubau theory simulations to compare the effect of the coating's properties. In the next plots, 3 different wires are compared, a simple uncoated copper wire (Sommerfeld wave), a copper wire with polyethylene coat (low dielectric constant) and another with a high resistivity silicone coat (high dielectric constant). The third material was based on planar Goubau line experiments led by Grzeskowiak et al. in [47]. In the following simulations, the wire material was copper, the radius used was a = 0.1 mm and the dielectric coating radius was b = a/0.95.

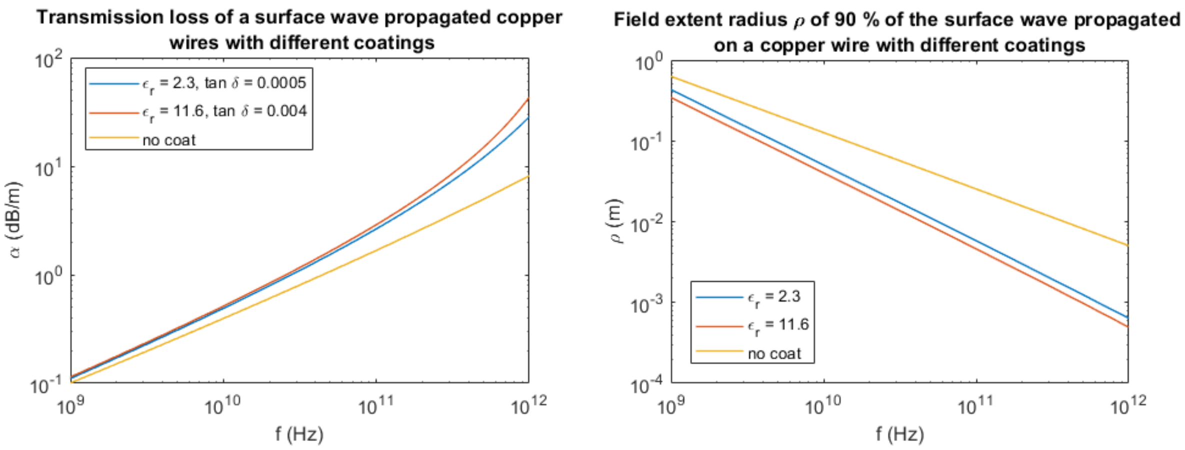

Figure 13: Attenuation (left) and radius of 90% of the lateral field power (right) for copper wires of 0.1 mm with various coatings

In figure 13, the attenuation and lateral field extent are displayed against frequency for the simulated wires. As expected, with a higher dielectric coating, the wave is more attenuated and the field is more confined to the wire surface. However, the difference between the two coatings is very minimal, except for the attenuation in the sub-THz region. Furthermore, as the frequency increases, the different gradient of slope between the coated and uncoated wires becomes more significant, resulting in a compromise between low attenuation or low field extent when designing the link. For example at 100 GHz, the uncoated attenuation is 1.8 dB/m, the coated one is about 3 dB/m and the 90% field extent radius of the uncoated wire is 27 cm and about 5 mm for the coated wires.

Earlier in the the theory chapter, it was seen that Sommerfeld and Goubau waves had opposite trends with regards to velocity against frequency. However, due to Sommerfeld wave phase velocity being so close to the speed of light, the slight decrease at lower frequencies is unnoticeable in figure 14. As ν_{gr} is the derivative of ν_{ph} in terms of frequency, the trend and values of the two plots are close to the same, except that the group velocity decreases further at higher frequencies, inducing a slight dispersion at those frequencies.

With the group velocity derived from the propagation constant h, the dispersion parameter can be calculated following equation (29), and was plotted in figure 15. In this plot, all values are very close to one another and to 0, up until 100 GHz after which higher dielectric coatings have a higher dispersion. In the presented results, the dielectric constant and dissipation factor are taken as constant with respect to frequency, which is inaccurate in practice. However the dispersion values remain very low, the further value from 0 is -6 x 10^{-7} ps/(nm.km), which remains negligible. Taking a standard ITU G652 single

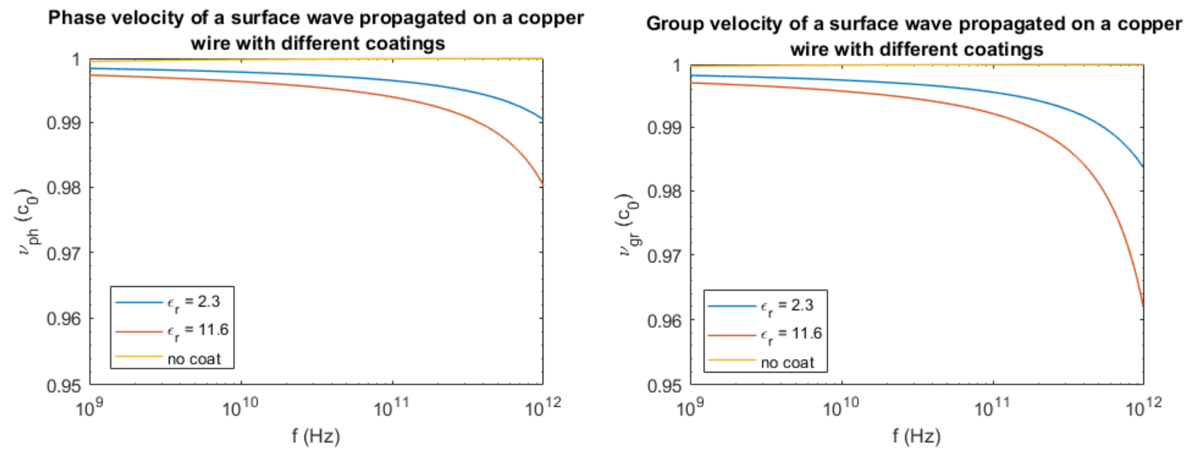

Figure 14: Phase velocity (left) and Group velocity (right) for copper wires of 0.1 mm with various coatings

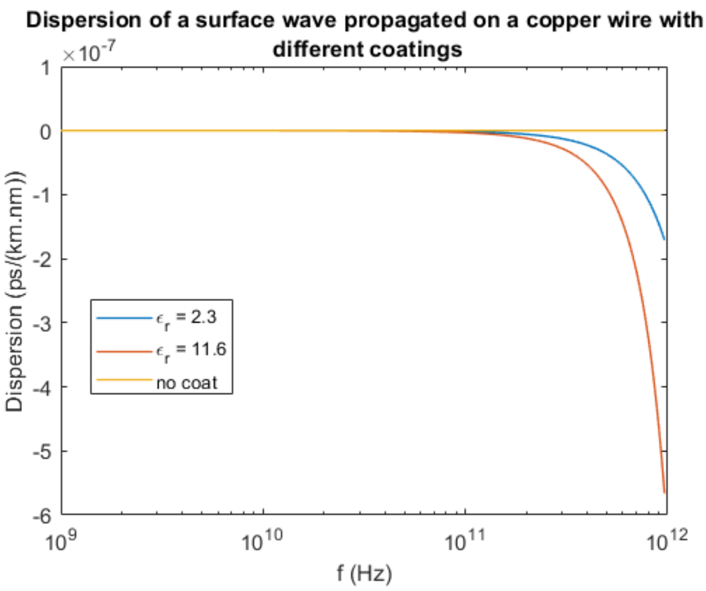

Figure 15: Simulated dispersion for copper wires of 0.1 mm with various coatings

mode optical fibre as a reference, its dispersion at 1550 nm (operating wavelength) is 17 ps/(nm.km) and it can operate over kilometers at gigabits per second rates [72]. As a result, dispersion can be considered as having little effect in the case of Goubau lines.

2.1.4 Planar Goubau line (PGL)

Another type of surface wave link exists beyond cylindrical Sommerfeld wave and Goubau line, the planar Goubau line, also called PGL. As indicated by its name, it is the planar equivalent of the dielectric coated Goubau wire line, and more precisely an ungrounded microstrip transmission line [73]. Currently, the main applications for these alternative transmission lines are THz biosensors and high speed interconnects, such as in data centres [17][74][75][47][29].

The concept and name of PGL was much more recent than the initial surface wave theory; it first appeared in Xu and Bosisio's 2004 paper [76]; where they use a square metal strip over a thin low dielectric material. They decided to base their dimensions on electromagnetic simulations, in order to keep their line as close to Goubau line as possible and suppress higher order modes for higher frequency ranges.

Figure 16: Picture of a planar Goubau line consisting of an FR4 substrate and copper conductor

Since then, many groups have opted for this solution to operate surface waves at mm and submm-waves frequencies due to the advantages of surface waves and the lower cost and easier fabrication of planar Goubau lines. Therefore, many simulated and experimental results have proved their usability and efficiency over a large frequency range and various fields as mentioned earlier.

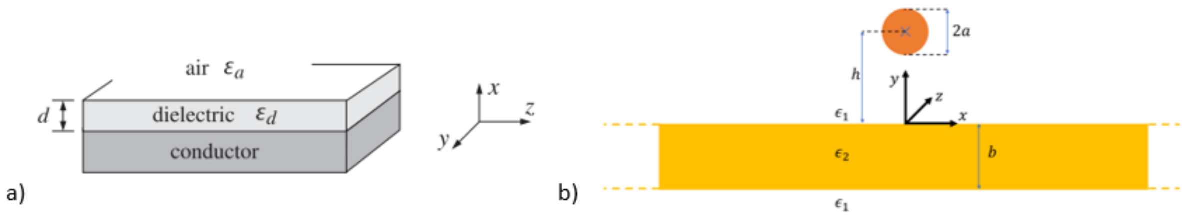

Figure 17: Symmetry of the analytical representations of the solutions for PGL from a) Orfanidis [4] and b) Schaich et al. [7]

Besides electromagnetic simulations and experimental measurements, very few mathematical models have been published for the planar Goubau line case. One derivation is covered in Orfanidis' book [4], where the planar Goubau line is modelled as the limit from where the dimensions a, the conductor radius and b, the dielectric radius tend to infinity, whilst the difference $a - b$ stays finite, assuming a perfect conductor and lossless dielectric as shown in figure 17 a). Through this work the main parameters of interest, such as the attenuation, phase velocity and field extent are calculated at a frequency range of 0.3 to 30 GHz.

More recently, as part of the same research project as this PhD, Schaich et al. derived numerical solutions in the case of a perfectly conducting cylindrical wire over a planar dielectric substrate, both separated by a small variable space [7]. In this paper, the derived model is compared against and verified with EM simulation tools and experimental results. Both of those models have proven to match the low attenuation and single propagation of the initial surface waves definition and can therefore be used to characterise a planar Goubau line system.

In the frame of this work, no mathematical derivations of planar Goubau lines will be used, however because simulations and experiments have been carried on PGL and planar launchers for surface wave generation, it is worth noting the work done on the topic. If future work were to be carried on planar links, further study would be conducted based one of the two models cited.

2.2 DSL theory and current standards

2.2.1 Transmission media overview

Data transmission comprises a large variety of technologies, and rather than being redundant, they actually complement one another, but it also results in a complex communications network.

We can divide these technologies into two categories, guided and non-guided media. The first one is also often called wired and is the transmission type surface waves will fall under, and the second is generally referring to any wireless communications whether being microwave, RF, or satellite technology. Due to the difference in wave transmission, it may seem less relevant to surface waves however being a passband technology and information technology being quite similar from one standard to another it can be a good transmission type to refer to.

One of the main determining factors of the use of each technology is the distance; standards range from very short to very long lengths starting at centimetres up to kilometres distances. However other factors are taken into account such as the cost of acquisition, installation and maintenance of the link and the cost and difficulty of upgrading to newer standards (and higher data rates) [77].

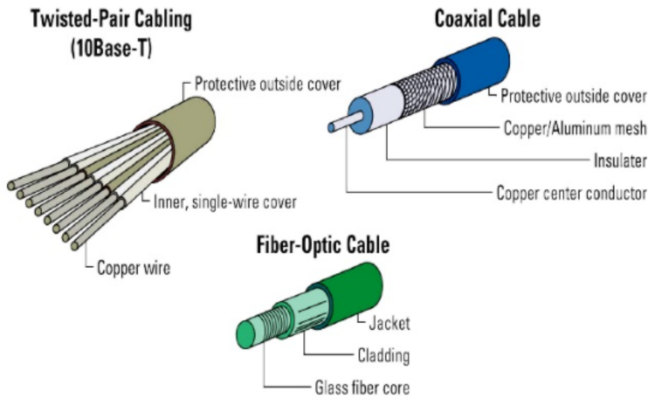

Figure 18: Ethernet wired transmission media representations [8]

Copper wire transmission lines are the oldest and most widespread technology for data transmission. There are two main types, twisted pairs and coaxial cables, both transmitting over conductive cabling but in different modes, the differential mode and the coaxial mode.

Twisted pair was first installed for carrying telephone signals and have since been reused for last-mile internet communications, operating from 4 kHz to allow both telephone and ethernet to transmit over the wires simultaneously. The cable structure is either a single twisted pair or a bundle of 4 pairs. Over the years and with the increasing need for data throughput over the same transmission length, the structure of TP cables has evolved to keep BER and interference low by adding some grounding and shielding over the bundle and/or over each pair. Throughout their evolution, twisted pairs have been widely deployed due to their low cost of initial installation. However, because of their cable structure, they have limited operating bandwidth (which has been extended with data generation and cable structure evolution but remains a limitation). They are sensitive to EM and RF interference and require repeaters for longer lengths of transmission (generally 100m without repeaters).

Coaxial cables were invented around the 1920s. They are a single core cable with a thicker copper wire than twisted pair strands, coated with a thick dielectric and a conducting grounded cylinder which produces the coaxial mode and makes the transmitted signals less affected by EMI (electromagnetic interference). It has a wider bandwidth than the earlier introduced twisted pair and the potential of long-range transmission. The better the cable structure, the more expensive it is due to its build and materials.

Another shorter range that has recently emerged for indoor wired internet is Power Line Communications (PLC), it transmits ethernet signals over the Power network within homes or buildings but requires a lot of repeaters throughout the network as it is rather short range. (Another possible application for surface wave technology.)

For many years now, the industry trend has been to move from the electrical to the optical domain, mostly due to the immense bandwidth availability and the evolution of the light generating and detecting circuits. Fibres are divided into two categories, multi-mode fibre (MMF) and single-mode fibre (SMF). Due to the almost unlimited bandwidth (in the case of SMF), they have close to no capacity limit and being an enclosed light transmission medium they are more secure than their copper counterparts. Although they are costly to fabricate, install and particularly to maintain due to the fragile structure of the actual fibre, they are generally used for medium to long haul networks. In recent years the cost of fabrication and maintenance has greatly decreased getting it closer to its copper counterpart.

The last category is wireless communications; it usually operates at microwave frequencies but mostly under 20 GHz, and is generally allocated in bands of 10-50 MHz. Being an unguided wave, it is susceptible to its environment and surroundings. Early technologies were quite lacking in data capacity but with the evolution of Long-Term Evolution (LTE) and small cells, its capacity has greatly increased. The main limitation is the sharing of the channel between multiple users limiting each individual's throughput.

As mentioned earlier, each technology has its particularities and therefore fits a specific application within the network. For the past few years, the Ethernet Alliance has been publishing a yearly roadmap with an overview of the current and future technologies and a survey of the developing industries to give an up to date illustration of the "Ethernet ecosystem" [9]. In the 2020 roadmap, applications have been split into 5 categories, from lower data rates required to highest: automation, automotive, enterprise, service providers and cloud providers. In the presented work frame, surface wave technology would be used for the third category: enterprise and campus applications ranging from 100 Mb/s to 400 Gb/s. And especially for LAN (local area network) delivery, as within the past 15 years, over 70 billion metres of copper cabling have been deployed in addition to all the already existing infrastructures.

EMERGING INTERFACES AND NOMENCLATURE

	Electrical Interface	Backplane	Twinax Cable	Twisted Pair (1 Pair)	Twisted Pair (4 Pair)	MMF	500m PSM4	2km SMF	10km SMF	20km SMF	40km SMF	80km SMF
10BASE-		T1S		T1S/T1L								
100BASE-				T1								
1000BASE-				T1	T							
2.5GBASE-		KX		T1	T							
5GBASE-		KR		T1	T							
10GBASE-				T1	T				BIDI Access	BIDI Access	BIDI Access	
25GBASE-	25GAUI	KR	CR/CR-S		T	SR			LR/ EPON/ BIDI Access	EPON/ BIDI Access	ER/ BIDI Access	
40GBASE-	XLAUI	KR4	CR4		T	SR4/eSR4	PSM4	FR	LR4			
50GBASE-	LAUI-2/50GAUI-2 50GAUI-1	KR	CR			SR		FR	EPON/ BIDI Access LR	EPON/ BIDI Access	BIDI Access ER	
100GBASE-	CAUI-10 CAUI-4/100GAUI-4 100GAUI-2 100GAUI-1	KR4 KR2 KR1	CR10 CR4 CR2 CR1			SR10 SR4 SR2	PSM4 DR	10X10 CWDM4/ CLR4 100G-FR	LR4/ 4WDM-10 100G-LR	4WDM-20	ER4/ 4WDM-40	ZR
200GBASE-	200GAUI-4 200GAUI-2	KR4 KR2	CR4 CR2			SR4	DR4	FR4	LR4		ER4	
400GBASE-	400GAUI-16 400GAUI- 8 400GAUI-4	KR4	CR4			SR16 SR8/SR4.2	DR4	FR8 400G-FR4	LR8 400G-LR4		ER8	ZR

Gray Text = IEEE Standard   Red Text = In Standardization   Green Text = In Study Group
Blue Text = Non-IEEE standard but complies to IEEE electrical interfaces

Figure 19: Ethernet standards nomenalture for various transmission medium technologies [9]

Figure 19 is displaying the current Ethernet technology standards, with the data rate on the table's lines, the transmission media used on the columns and the specific standard's name at the intersection.

Looking at the different technologies, they are arranged by operating transmission length, with on the left side standards for high-speed short reach (PCB interconnects levels), then Twinax cables which are defined for maximum lengths of 3-7m, single twisted pair used in automotive and IoT fields for reaches up to 40m, 4 pairs twisted pairs in ranges of 30 to 100 metres, multimode fibres defined between 100 m and 2 km depending on the standard and finally, the single-mode fibre or SMF with reaches shown in figure 19, and up to 80 km in standardisation.

2.2.2 Twisted pair technologies

This work aims to explore the feasibility of using surface wave transmission over existing wired networks to fill gaps within Ethernet deployments and provide higher data rates to premises with existing infrastructure.

The path explored here is the upgrade of twisted pair communications, and even though installations have evolved throughout the years and within the network, several types of cable structures exist. The standards currently used to support twisted pair communications are shown and characterised in table 1, higher end ones being more specific to data centres with higher complexity cable structures (non-compatible with surface wave transmission).

Application	Standard	IEEE	Cable cat	lanes (TP)	Bit rate	Max. reach	Bandwidth	Modulation	Coding
Automotive/IOT	1000BASE-T1	802.3bp	cat 6a	1	1 Gb/s	40m	375 MHz	PAM3	80b/81b RS-FEC
LAN	1000BASE-T	802.3ab	cat 5	4	1 Gb/s	100m	62.5 MHz	4D-PAM5	TCM
LAN	2.5GBASE-T	802.3bz	cat 5e	4	2.5 Gb/s	100m	100 MHz	PAM16 and 128 DSQ	64b/65b LDPC (2048/1723)
LAN	5GBASE-T	802.3bz	cat 6	4	5 Gb/s	100m	200 MHz	PAM16 and 128 DSQ	64b/65b LDPC (2048/1723)
LAN	10GBASE-T	802.3an	cat 6 or 7	4	10 Gb/s	55/100m	400 MHz	PAM16 and 128 DSQ	64b/65b LDPC + TH precoding
Data centres	25GBASE-T	802.3bq	cat 8	4	25 Gb/s	30m	1000 MHz	PAM16 and 128 DSQ	RS-FEC (192, 186) + LDPC(2048/1723)
Data centres	40GBASE-T	802.3bq	cat 8	4	40 Gb/s	30m	1600 MHz	PAM16 and 128 DSQ	RS-FEC (192, 186) + LDPC(2048/1723)

Table 1: Twisted pair Ethernet communication standards performance and characteristics summary [50][51][52][53][54]

Table 1 shows a good overview of achievable data rates with copper cabling together with the available bandwidth, modulation and coding formats. Looking at the standards, modulations vary from PAM5 to PAM16 (from 2 bits to 4 bits per symbol). The latter is implemented together with 128 DSQ, meaning 128 double square constellation, it is "obtained by concatenating two time-adjacent 1D PAM16 symbols and retaining among the 256 possible Cartesian product combinations, 128 maximally spaced 2D symbols" [78]. 16PAM together with 128DSQ results in 7 bits of data 4 of which are coded and 3 are uncoded. Further capacity and error immunity improvements can be implemented through channel encoding. The data encoding methods employed in the presented standards are TCM, standing for Treillis coded modulation, which is one of the most common convolutional type codes. LDPC, the low-density parity-check code, belongs to the turbo type code and has a high coding gain getting it close to the Shannon capacity potential. And RS-FEC meaning Reed-Solomon Forward error code, is a type of block coding, very efficient at correcting errors (up to a parametrised number of errors).

In terms of the data rates presented, it would be more relevant to review the data rate per TP lane as the thesis is only demonstrating single lane data transmission. The data rate per lane can be calculated with the ratio of total bit rate to the number of lanes from table 1. The lane data rate ranges from 0.25 to 10 Gb/s for cable lengths of 30-100 m and bandwidths of 62.3 MHz to 1.6 GHz.

Decades of work has been invested in increasing the data rate and reliability from one standard generation to another which is why a quick review of the principles used to increase the data rate as well as decrease the cross talk of each TP and bundle was carried out.

2.2.3 Surface wave for telecommunications literature

Since their discovery, surface wave modes have been a strong contender for data transmission [63] largely due to their low attenuation over various wires and a very wide range of frequencies.
In the early days, the main issues were the field extent (mostly Sommerfeld), the loose bounding to the surface of the wire inducing attenuations at bends and other structural irregularities, exacerbated by the lack of options for higher frequency signal generation. Operating at lower frequencies leads to the inconvenience of larger antennas and field extent. When more recent papers were published from 2004 [79], new interest was brought to surface waves, for communications and other applications, especially around terahertz frequencies.

From there, two main projects started for surface wave data communications: the Airgig project and TDSL. Airgig started in 2012 in the form of an AT&T project. The main idea consists of transmitting data with surface waves on the power cable network to deliver broadband internet to nearby homes and mobile devices. It would then be compatible with 4G and 5G data transmission, from one power pole to another, similar to DAS (distributed antenna systems).

This application is particularly good in terms of surface wave theory as attenuation decreases with thicker cables, even though it increases field extent, the design takes into account licence free frequency bands. Another advantage to this technology is using the power cable infrastructure which consists of tall mostly straight and non-obstructed cable single lines with poles (used as repeaters) at medium distances. Due to surface waves (especially Sommerfeld) being loosely bound and sensitive to bends and obstacles, this is a rather ideal setup. In terms of weather effects, it was measured to have minimal effect on the transmission [80].

In this project, hundreds of patents have been filed, most of which cover the transmission structure, the launcher designs and other details [81, 82].

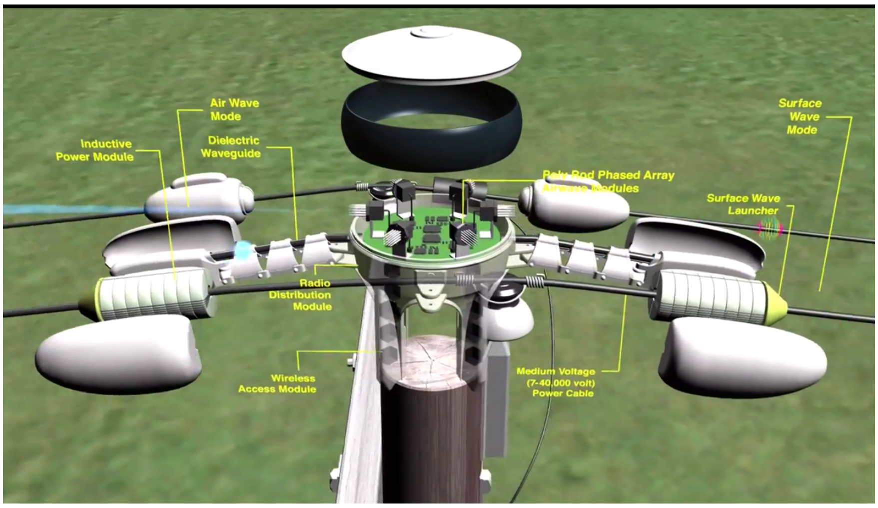

Figure 20: Airgig project exploded view of the surface wave transmission over a power pole [10]

The design team has announced a few technical details about the system as follows. Firstly, the launchers design, as shown in figure 20; they are plastic non-invasive launchers that are installed over the power cables (minimal installation time and cost) and transmitting at mmWave frequencies and then converting the signal back to the standard wired/wireless format at each pole. Secondly, Airgig gives a new control over power lines, which could offer real-time management for the power line companies such as meter reading or pinpointing disruption and breakage locations in the network. Lastly, AT&T claims it would be an efficient solution to deliver broadband internet globally, even to more deprived areas, estimating hundreds of Mbps (and potentially up to Gbps if commercially developed) to residential locations [80].

In 2017 John Cioffi, know as"the father of DSL", has presented the new concept of TDSL, meaning terabit digital subscriber line, using surface waves over twisted pairs of over 100 metres [64]. Two possible ways of generating such data rates were given, firstly the waveguide mode on a single pair, similar to AT&T, but using an enormous bandwidth. And secondly, using the transmission-line mode over a whole bundle of twisted pairs (estimated to 50-100 pairs in the presentation) through vectoring.

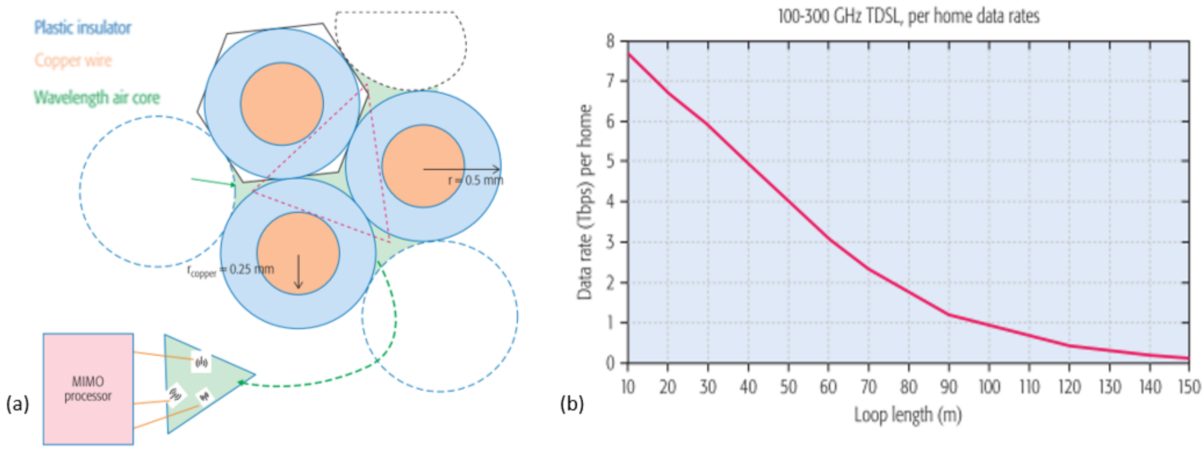

Figure 21: a) MIMO vectoring over twisted pair bundles for TDSL illustration and b) Simulated data rates for TDSL link against line length [11]

In a later paper, the process to obtain TDSL is further explained as well as initially simulated data rates over various link designs [11]. In a nutshell, multiple electric and magnetic fields are propagated along each wire at mm-wavelength (TM, plasmon-polariton TEM and potentially TIR modes) which will create large crosstalk between the modes and will be used for signal recovery through vectoring (or MIMO) rather than cancelled to remove crosstalk. Some simulations have been carried with the main parameters being:

- up to 20 dBm transmit power
- 4096 subcarriers between 100 and 300 GHz
- bit loading up to 12 bit/Hz
- 100 waveguide modes in the cable (2 per wire)
- attenuation value taken from [79] equal to 0.05 dB/m (using a single value is however unrealistic for a bandwidth of over 100 GHz)

The results are displayed in figure 21 b) showing data rates of 0.1 to 7.5 Tb/s for length between 150 and 10 meters. Further simulations showed that with vectoring and multiple EM mode propagations, this system would allow data rates of Tb/s up to 100 m, 100 Gb/s at 300 m, and 10 Gb/s at 500 m.

Initial experimental mode measurements around 200 GHz has been published [83], from which data rate simulations have been extrapolated. With the presented setup, Tb/s rates have been calculated for lengths of a few metres or below and a 30 Gb/s rate was obtained at 15 m. A few questions remain about this project, firstly the viability of launching those EM modes at the same time especially since TM (Sommerfeld) waves should not be grounded, and hence if it would be actual surface wave transmission. But also the very large bandwidth that has been planned 100 - 200 GHz and the devices required to generate such data rates. They are planning to use optical signal generation and such systems have proven to be lossy and may be very costly [33].

In this work, a mix of both concepts is used with a stronger focus on single line transmission at lower frequency (and therefore data rates). It is a initial proof of concept experiment with the hope of evolving to MIMO transmission in future work (planing on using only the TM_{01} mode transmission, but may excite others due to cabling structures).

2.3 Data transmission and processing techniques - information theory

The physical properties of surface waves have been introduced earlier in this chapter and since surface waves were first discovered data transmission technologies have drastically evolved. With high achievable carrier frequencies, and high-end modulation techniques available, surface wave transmission is now a strong contender for high data rate communications on imperfect channels.

The following section will introduce data generation and processing theory for the processes used experimentally. Figure 22 a) and b) is a block diagram of the signal generation and processing used in the OFDM transmission of chapter 5.2 of the thesis.

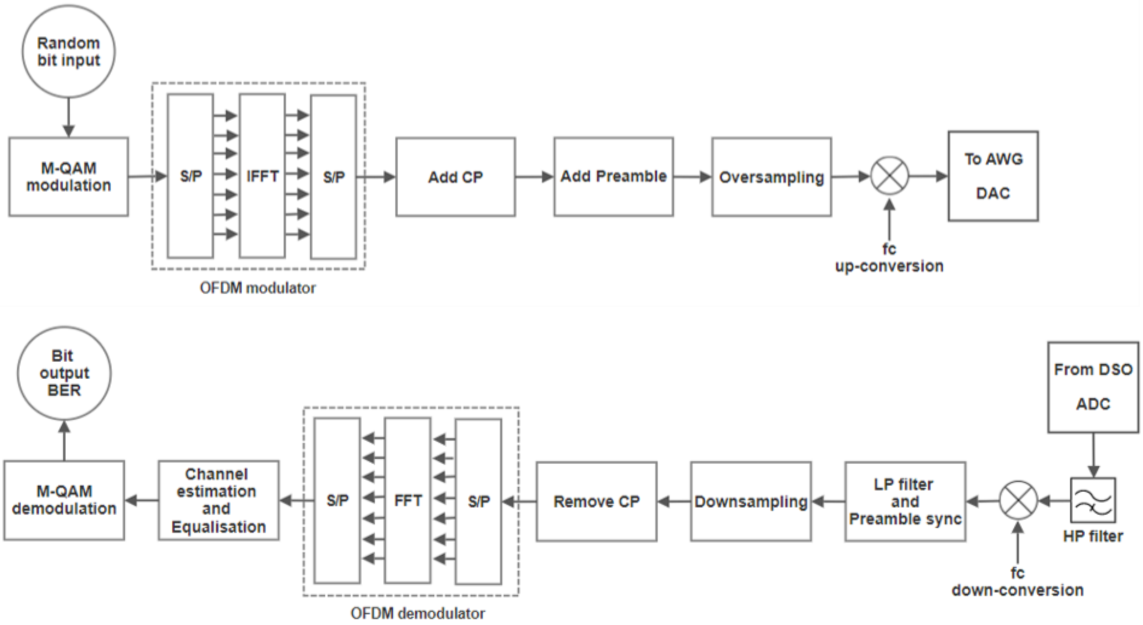

a)

b)

Figure 22: Block diagram of a) the data generation and b) the data processing experimental approach

In order to understand it a bit further, some of the digital signal processing theory will be covered here.

2.3.1 Digital modulation

One of the major aspects of data transmission is signal modulation. It changes some parameters of the wave such as amplitude, phase and frequency and allows it to transmit more information. There is a trade off between the modulation levels (bits/symbol), the required SNR and the required bandwidth (symbols/sec). Rather than transmitting only 1 bit per second, 2 bit (decimal values up to 4) or more can be transmitted at once, it then becomes a symbol and the data rate can also be expressed in symbol rate instead of bit rate. The most commonly used modulation formats are illustrated in figure 23.

Digital modulation consists of mapping k number of bits into a symbol s, with $0 \leqslant s \leqslant 2^k - 1$, and the modulation order being $M = 2^k$. Therefore if one modulated symbol is transmitted every T_s, the symbol rate R_s becomes:

$$R_s = \frac{1}{T_s} \tag{31}$$

And its bit rate, R_b, is:

$$R_b = \frac{k}{T_s} = kR_s = log_2(M)R_s \tag{32}$$

From there another important factor can be derived, the bandwidth efficiency, *eff*, in bit/s/Hz (also called spectral efficiency) which can be defined as the ratio of bit rate to transmission bandwidth, therefore the higher the *eff* the higher the bit rate in each hertz of bandwidth. Its value varies depending on a few parameters, but in the case of a baseband Nyquist filtering, the bandwidth at baseband would be $0.5R_s$ and at the carrier frequency it would be $B = R_s$. So for an M-ary modulation, the bandwidth efficiency is:

$$eff = \frac{R_b}{B} = log_2(M) \tag{33}$$

Such M-ary modulations have been represented in figure 23 with the constellations of amplitude, phase and quadrature amplitude modulations and the time domain plot of a binary frequency modulation. Some

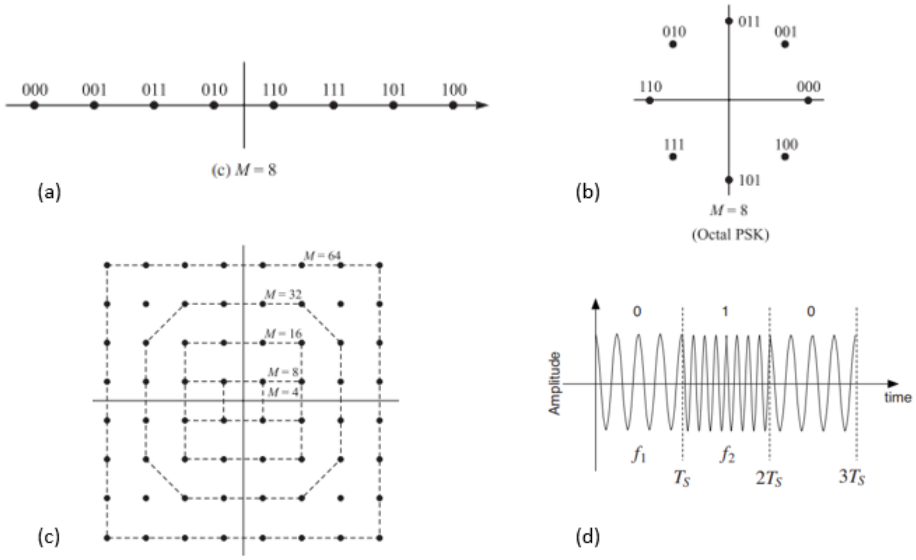

Figure 23: Graphical representation of common modulation formats, with the constellation of a) an 8 PAM, b) an 8 PSK, c) various M QAM and d) a time domain binary FSK [12][13]

of those modulation formats' bandwidth efficiency has been summarised in figure 24 for a given BER = 10^{-5}. It can be seen that the ones closest to Shannon capacity are QAM and single sideband PAM.

2.3.2 Orthogonal frequency division multiplexing (OFDM)

A type of digital transmission method that can be added on top of the earlier basic digital modulation formats is frequency division multiplexing (FDM). It consists in dividing the transmission bandwidth in subchannels each one of them can transmit independently modulated or coded symbols. This type of transmission is used when one or more of the subchannels would be unreliable from time to time, for example high attenuation or interference. One of the most common form of FDM is orthogonal frequency division multiplexing (OFDM), meaning the subcarriers of the channel are orthogonal one to another.

If there are N OFDM subcarriers (and therefore subchannels), the subchannel bandwidth is B_{sub}, with B the total transmission bandwidth:

$$B_{sub} = \frac{B}{N} \tag{34}$$

The OFDM modulator and demodulator are represented in figure 22. In the generator, the modulated symbols are converted from serial to parallel, N symbols at a time, and then go through an inverse Fourier transform (IFFT), now transmitting in the time domain, finally the signal is converted back to serial from parallel.

After this, a cyclic prefix (CP) is added at the front of the OFDM symbol and acts as a time guard band against interference. The cyclic prefix is made out of the last x subcarriers in the time domain of each OFDM symbol and it is added to the front of the symbol, as shown in figure 25.

Lastly, to front of the OFDM symbol and frame, is added a preamble, it is used for synchronisation purposes on the receiver side. The synchronisation process presented is the one proposed by Schmidl and Cox in [49][48]. In the paper, the preamble is made of two identical halves (in the time domain); each with a pseudo-noise sequence transmitted on the even frequencies and zeros on the odd frequencies, to which a cyclic prefix is then added.

Using this structure, a coarse estimate of the preamble's start point can be calculated as well as a carrier frequency mismatch between the transmitted and received signal.

On the demodulator side, once the preamble start has been calculated, the OFDM symbol's CP is removed and the time domain signal is converted from serial to parallel, the parallel subcarriers are passed through a fast Fourier transform and are converted back to serial data (in the frequency domain).

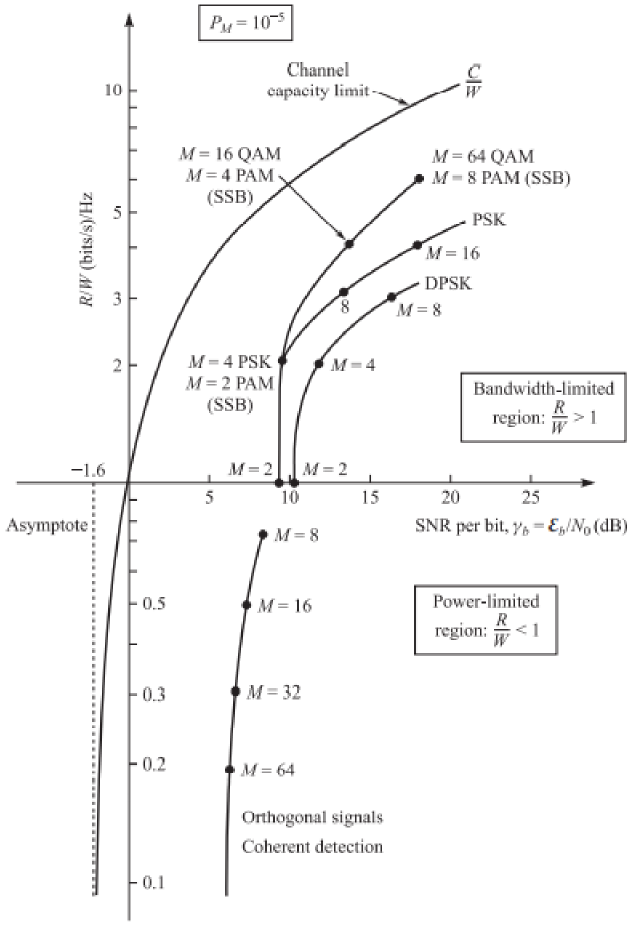

Figure 24: Bandwidth efficiency against SNR per bit for a few modulation formats with BER = 10^{-5} [12]

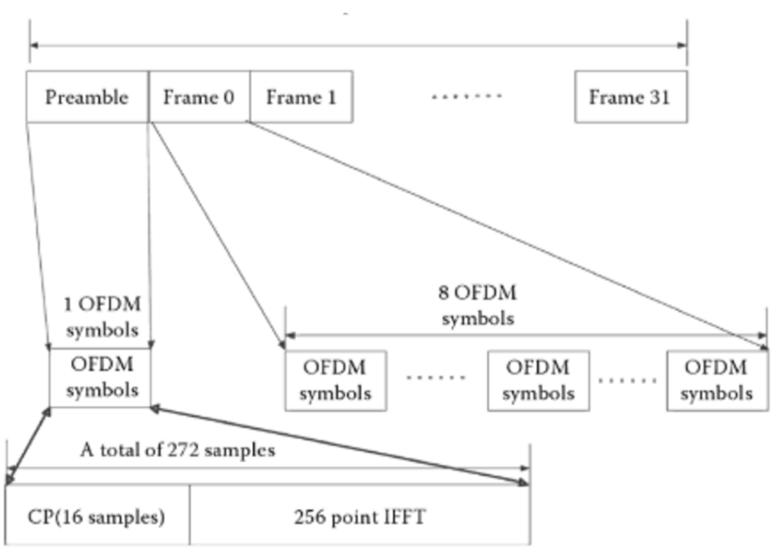

Figure 25: Example of OFDM transmission structure [14]

Another name given to OFDM, generally when talking about wired communications is discrete multitone or DMT. In such systems, DMT is associated with bit loading, meaning that a maximum bit per subcarrier is defined and depending on the channel response, a bit/symbol value is allocated to each subchannel to optimise the data transmission and minimise errors. This process is explained in more detail in the capacity simulations chapter.

2.3.3 Frequency mixing and up-sampling

In digital communication, the signal can be transmitted either baseband or passband, meaning the signal bandwidth will be the same in both cases but it will be transmitted at a specified frequency, either to suit the antenna and circuit characteristics or to suit the wireless spectrum. In terms of surface waves, they can be transmitted over most of the frequency spectrum, however, too low frequencies will induce bulky antenna design and much narrower transmission bands.

Frequency mixing is generally done by analogue mixing of a sine wave of the carrier frequency, f_c, and of the baseband I and Q signals separately. However when mixing digitally, a large enough frequency spectrum needs to be defined (f_{clock}). The signal, $S_{frequp}(t)$, transmitted over the channel is obtained with the following equation.

$$S_{frequp}(t) = I \times cos(2\pi t f_c) - Q \times sin(2\pi t f_c); \tag{35}$$

Before upmixing, the signal is upsampled to obtain a wider frequency band of operation, and a pulse-shaping filter is applied to the data. In this case, a root raised cosine (RRC) filter is used with a defined filter span, roll-off factor and output samples per symbol, *sps*. The pulse shaping will make the signal more resistant to channel infringements and the filter's sps is chosen such that:

$$sps = \frac{f_{clock}}{B} \qquad \text{with,} \qquad f_{clock} > 2 \times \left(f_c + \frac{B}{2}\right) \tag{36}$$

With f_{clock} the sample rate of the upsampled and upmixed signal (also serves as an input to the waveform generator), and B the transmission bandwidth.

2.3.4 Equalisation

Equalising is mostly used to reduce inter-symbol interference (ISI) effects, these are caused by the transmission channel response. The equaliser's purpose is to correct the received signal such that phase, amplitude, timing and frequency effects of the channel are removed and result in a close to flat channel response.

Many possible structures exist but two are used here, the adaptive one, which has low to medium computational complexity, and the MLSE (maximum-likelihood sequence estimation) one, with high computational complexity but with high performance in time-varying propagation channels. Within the adaptive structures, there are two types of equalisers: linear and decision feedback equalisers. Both of which use the same algorithms: least mean squares (LMS), recursive least squares (RLS) and constant modulus algorithm (CMA). Depending on the situation the type of equalisation can be chosen to fit the system's requirements. If the frequency response of a channel possesses frequency nulls, linear equalisers tend to enhance the noise. In this case, decision feedback equalisers would be used to avoid signal degradation.

Decision Feedback Equaliser (DFE)

The decision feedback equaliser structure is represented in figure 26. Its input can either be 1 sample per symbol or K samples per symbol (K being an integer of 1 or more) therefore this input data rate is K/T and the output data rate is $1/T$ with T the symbol period.

The central top part is a simple feedforward filter with L taps and the central bottom part is the feedback filter with $N - L$ taps, each of the taps have an associated weight, w_i with $1 \leqslant i \leqslant N$ that is updated every T. To both filters, the input signal is the vector $\mathbf{u}$, and the output of the equaliser is y. The decision device feeds hard decision to the feedback filter, its output is y_d, however when the equaliser is in training mode, the decision device is unconnected and the training (known) sequence is

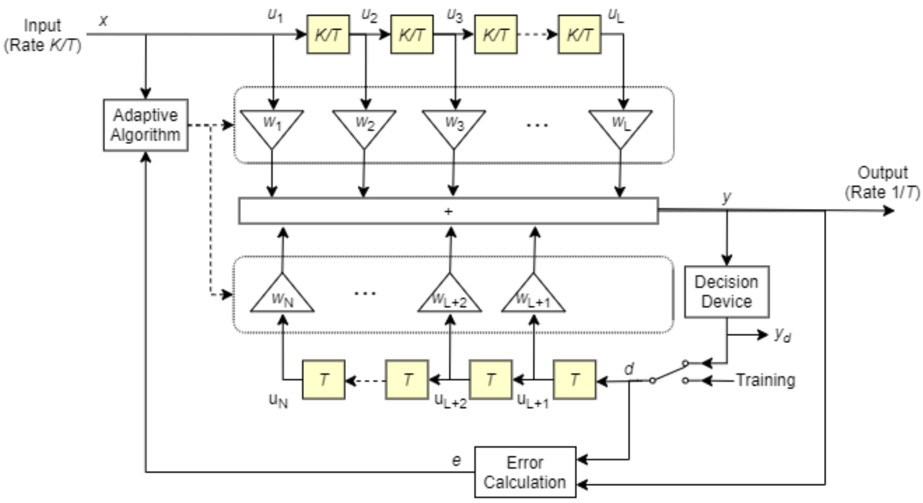

Figure 26: Decision feedback equaliser block diagram [15]

fed to the feedback filter, the output of either one of the mode is defined as d. A few parameters can be added to the equaliser such as the modulation format which will make its predictions easier.

In order to update the equaliser taps, an error, e, is calculated and fed to the adaptive algorithm such that:

$$e = d - y \qquad \text{(LMS or RLS)} \tag{37}$$

Depending on the algorithm, the weights are calculated differently. For LMS the new equaliser weights $\mathbf{w}_{new}$ are:

$$\mathbf{w}_{new} = \mathbf{w}_{current} + (\text{step size})\mathbf{u}e^* \tag{38}$$

With step size, an LMS parameter that is user-defined, and e^* the complex conjugate of the error.

As for RLS, the weight calculation is dependent on some new parameters, $\mathbf{P}$, the inverse correlation matrix (its initial value can is user-defined) and $\mathbf{K}$, the Kalman gain vector. Another parameter that is once again user-defined, the forgetting factor $0 \leqslant forg \leqslant 1$, setting how much of the previous taps' weight is forgotten or kept in the next iteration.

$$\mathbf{K} = \frac{\mathbf{Pu}}{forg + \mathbf{u}^H\mathbf{Pu}} \tag{39}$$

$$\mathbf{P}_{new} = \frac{(1 - \mathbf{Ku}^H)\mathbf{P}_{current}}{forg} \tag{40}$$

Therefore the new RLS weights can be calculated:

$$\mathbf{w}_{new} = \mathbf{w}_{current} + \mathbf{K}^* e \tag{41}$$

Single Tap Equaliser - OFDM case

When using OFDM, due to each symbol being transmitted over a much narrower bandwidth, the equalisation is greatly simplified. Depending on the needs of the system, the pilots (training symbols) can either be spread on a few points of each OFDM symbol throughout the transmission as is used for time varying channel response, for example in wireless systems. Or it can be set as a full symbol once every few frames, to have a more precise estimate of the full channel; this would be suitable for links with a more stable channel response over time such as wired links.

In the presented system, the first symbol immediately after the preamble is used for equalisation and is consequently known by the receiver. From this symbol the link's channel response can be estimated as:

$$H_{est}(f_{subcarrier}) = \frac{QAM_{Rx}(f_{subcarrier})}{QAM_{Tx}(f_{subcarrier})} \quad (42)$$

The above estimation takes place after the OFDM demodulator and before the QAM modulator, the known symbols are therefore frequency domain QAM symbols. A single tap equaliser means that each subcarrier has only one equaliser tap, therefore the equalisation at all $f_{subcarrier}$ can be done as such:

$$QAM_{equalised} = \frac{QAM_{Rx}}{H_{est}} \quad (43)$$

In the case of the project's OFDM transmission further processing has been done over the channel estimate, H_{est}, firstly outliers points are removed using software's built-in functions and secondly a moving average of the channel response was taken, to get a smoother frequency response. Such parameters were compared to an average of several captures of the channel response over time and gave much closer results to the measured response.

2.3.5 Analysis tools

Once the received data has been processed, a few measurements will help determine the channel effect and data processing and correction effectiveness on the quality of the signal.

One of the first analysis tools is called the error vector magnitude (EVM) and is used to determine the quality of the received symbols on the constellation diagram. Due to the channel response, the expected data point might be slightly shifted in terms of amplitude or phase from the modulated data. The measurement of this shift is then the EVM.

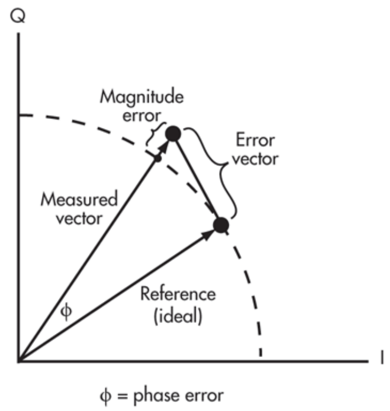

Figure 27: EVM representation with ideal and measured data on a constellation [16]

A graphical representation of the EVM is shown in figure 27 and it can be calculated using the following equation:

$$EVM(\%) = \sqrt{\frac{P_{error}}{P_{reference}}} \times 100 \quad (44)$$

For example for the QAM modulation defined earlier, the maximum acceptable EVM is: for QPSK, EVM $\leqslant$ 17.5%, for 16 QAM EVM $\leqslant$ 12.5 % and for 64 QAM EVM $\leqslant$ 8 %; in order to stay within the area of the transmitted symbol as QAM demodulation is a hard decision demodulation [84].

The next and most common data transmission result is the bit error rate or BER. As indicated by the name, it is the ratio of the error bits received to the transmitted data bits post demodulation and decoding. Any known bit used for synchronisation or equalisation training is not taken into account in the calculation, as it is not carrying any data.

$$BER = \frac{\text{error bits}}{\text{total data bits sent}} \quad (45)$$

This then leads to another output parameter, the overhead. The overhead, OH, is the ratio of data bits to the total amount of bits sent through the link, including known bits used for signal quality purposes (data and non-data). Its main sources are synchronisation (for example the preamble in OFDM), equalisation (for example DFE's training sequence or OFDM's pilots), the modulation structure (for example OFDM's nulls or cyclic prefix) and mostly coding. Depending on the type of coding used, the overhead can vary greatly from 1/2 to almost nothing.

$$OH = (OH_{\text{coding}}) \left(\frac{\text{data bits}}{\text{total sent bits}} \right) = (OH_{\text{coding}}) \left(1 - \frac{\text{non-data bits}}{\text{total sent bits}} \right) \tag{46}$$

In the case of the data transmission represented in figure 22:

$$OH = \left(1 - \frac{\text{preamble} + OFDM_{\text{symb 1}}}{OFDM_{\text{symb all}} + \text{preamble}} \right) \left(1 - \frac{CP}{OFDM_{subcarriers} + CP - OFDM_{Nulls}} \right) \tag{47}$$

The main use of overhead is to calculate the actual data rate, the initial data rate is calculated using the bandwidth and the modulation's bandwidth efficiency but does not yet take into account the non-data bits. Therefore the actual or post-overhead data rate $R_{\text{post-OH}}$ can be obtained using:

$$R_{\text{post-OH}} = R_{\text{pre-OH}} \times OH \tag{48}$$

3 Surface wave transmission experimental overview

3.1 Full system overview (holistic approach)

An overall setup design is required when using surface wave technology. As surface wave properties can vary with most structure parameters, the system design will depend on the application and hence the frequency range, distance and bit rate required. A standard communication system transmitting data through surface waves is summarised in the diagram figure 28.

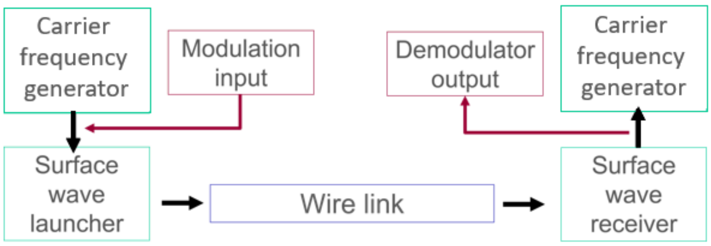

Figure 28: Basic surface wave telecommunication system diagram

The surface wave wire to dielectric interface can be considered as a waveguide, which is quite similar to optical fibre signal propagation. They remain EM waves and are a part of the electrical transmission domain.

The overall system design can be flexible and will mainly depend on cost, frequency ranges, available technologies and components' performance.

In the previous chapter, most advantages of surface waves have been described; however, they still include a few inconveniences and limitations for potential applications.

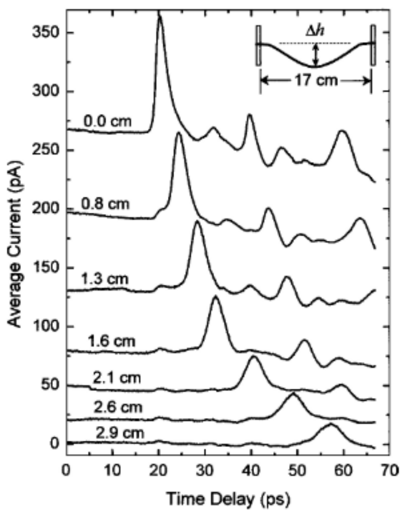

Figure 29: Effect of bending on surface wave transmission at about 100 GHz with Δh the curve depth [17]

The first one is the energy loss at wire corners, bends or discontinuities, this phenomenon was described in an experiment represented figure 29 from [17].

The loss comes from the fact that the wave is loosely bound to the conductor (in particular ones with high conductance [85]), causing higher energy loss at discontinuities such as bends.

Suggested solutions involve applying a dielectric coating or a thicker/higher permittivity dielectric material at the bend, which would provide closer binding of the wave and smaller field extent but higher attenuation. This would be a better solution for shorter lines [62]. Another alternative is to create another horn receiver and launcher at the bend, meaning converting the wave to TEM and back to TM modes [18], as shown in figure 30. Otherwise, using a less conductive wire material such as stainless steel instead of copper at the bend would have similar effects as the first solution [85], but loss may arise from some misalignment of the two wires.

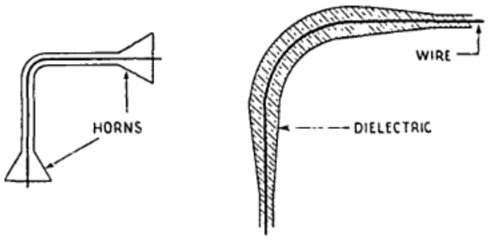

Figure 30: Solution representation for reducing bend attenuation from [18]

A well studied solution for reducing bending losses is the use of parallel wires. This concept is further descrbed in section 3.3.1 of the thesis. An example of a coated two-wire bend with low effect on propagation can be found in [86].

Furthermore, some results of 45^o and 90^o bending on a twisted pair around 1 GHz were presented at a collaborative workshop (unpublished results); at this frequency range, the measured loss was only a few dB.

Seeing as the field propagation must change when the same signal is sent over two close wires (within the lateral propagation distance), a more condensed wave would then exist between the two wires. This phenomenon could potentially apply to twisted pairs as well.

The second main disadvantage of surface wave transmission is the cross-sectional radius of the wave propagation. It was thoroughly characterised in the surface wave mathematical model in chapter 2. This is a significant issue for communications systems, firstly because of crosstalk between the lines and also for data security reasons. Additionally, and more importantly, the transmission may be affected by any interfering object or surface, which would be problematic for underground applications, such phenomenon was studied in [7] and shown later in figure 52.

As seen earlier, the field extent can be diminished with higher frequencies and dielectric coatings, both of which, as a counterpart, increase the propagation attenuation. This is not an issue for shorter or high-frequency links (for example, backplanes).

3.2 Launcher design

When Sommerfeld first published his work, Sommerfeld waves were only based on theoretical calculation and not yet verified experimentally. It was in Goubau's papers that a more practical setup was mentioned; in [69], part VI was entirely dedicated to the surface wave launching device. The aforesaid launcher consisted simply in a "tapered coaxial line", as shown in figure 31, and the receiving side would reverse the mode conversion of the wave using the exact same antenna device.

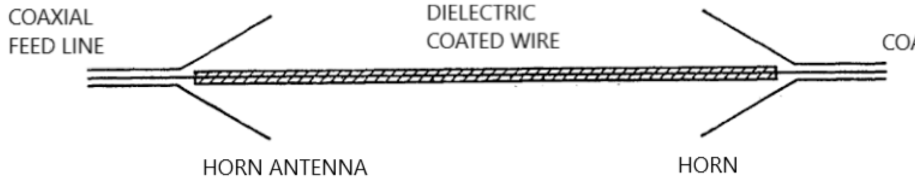

Figure 31: G-line with coax input/ouput drawing from [19]

As mentioned earlier, the electromagnetic transmission mode corresponding to the (low attenuation) surface waves is the TM_{01} mode, which presents a radial electric field and a circular magnetic field.

Furthermore, the most common electrical feed is the coaxial line, which presents TEM mode propagation, meaning both electric and magnetic fields are perpendicular to the direction of propagation. The issue was then to convert the more common feed TEM mode to the wanted TM mode.

In terms of Maxwell's corrections of Ampère's circuital law, all currents can be expressed in the form of equation (2).

In a coaxial cable, the displacement current is very small; hence most of the current is free current. In a copper wire, free current is the normal conduction. As the diameter of the outer conductor of a coax cable is increased, the free current drops towards zero, and so does the transverse electric field. Therefore the magnetic field is built entirely from the displacement current. This magnetic field is transverse to the direction of propagation but generates a longitudinal electric field, representing the desired TM wave at the impedance of free space.

These relationships and fields are represented in figure 32, which is a side cut of the launcher with, on the output side, the E-field being longitudinal and the H-field circular. This explains the choice of the imaged "tapered coaxial cable", but more commonly called the conical horn antenna.

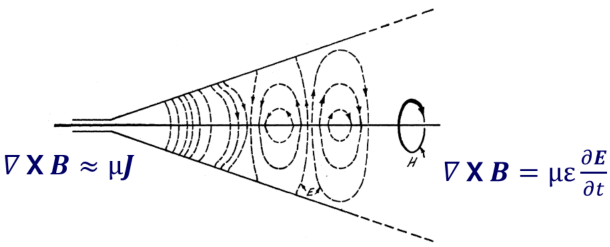

Figure 32: TEM to TM mode transition with field representations from [20]

Now that the required launcher was found, a deep understanding of the structure, mode conversion and design parameters of the horn antenna is required to build a functioning system.

The modelling theory for that specific horn was properly established in 1950 by Andrew Peter King as well as Schorr and Beck the same year [21] [87]. A more recent paper was published comparing different conical horn theories and developed a more accurate model for the optimum conical horn design depending on the system requirements. The following equations have been derived from these papers and the *Antenna Theory Analysis and Design* book [22].

The horn antenna symmetry and dimensions used to characterise it are shown in figure 33.

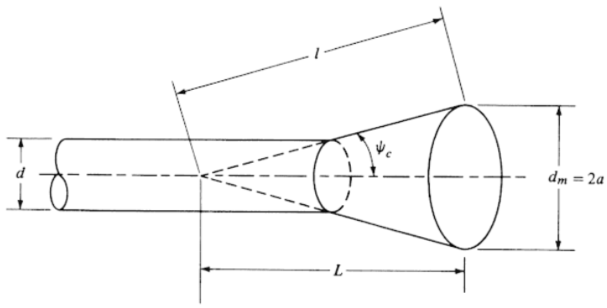

Figure 33: Symmetry of a conical horn from [21]

The main three components to describe conical horn antenna's performance would be its directivity or absolute gain D, the wavelength of operation λ, the aperture diameter d_m and the apex to aperture flare length l. The directivity, in linear units, is defined as:

$$D = \epsilon_a \left(\frac{\pi d_m}{\lambda}\right)^2 \tag{49}$$

With ϵ_a the aperture efficiency, which "represents the reduction in gain due to the amplitude and phase tapers across the horn aperture" [25], when expressed in dB it is then called the loss factor, L, which can be approximated as a function of the maximum phase deviation, s (in wavelengths).

$$L(s) = -10log_{10}(\epsilon_a) \tag{50}$$

$$s = \frac{(d_m)^2}{8\lambda l} \tag{51}$$

For optimum directivity, the aperture diameter should be as equation (52). Therefore, the design is best when $s = 3/8$ wavelengths, meaning $L(s) = 2.9$ dB and $\epsilon_a = 52$ %.

$$d_m \simeq \sqrt{3\lambda l} \tag{52}$$

The main design parameters have been brought together in a graph plotted by Gray and Schelkunoff in [21] based on experimental data, figure 34; the optimum design corresponds to the dashed line, with varying d_m/λ and L/λ, illustrated in the inset. As the flare angle diminishes and the antenna is becoming a cylinder, the maximum gain increases.

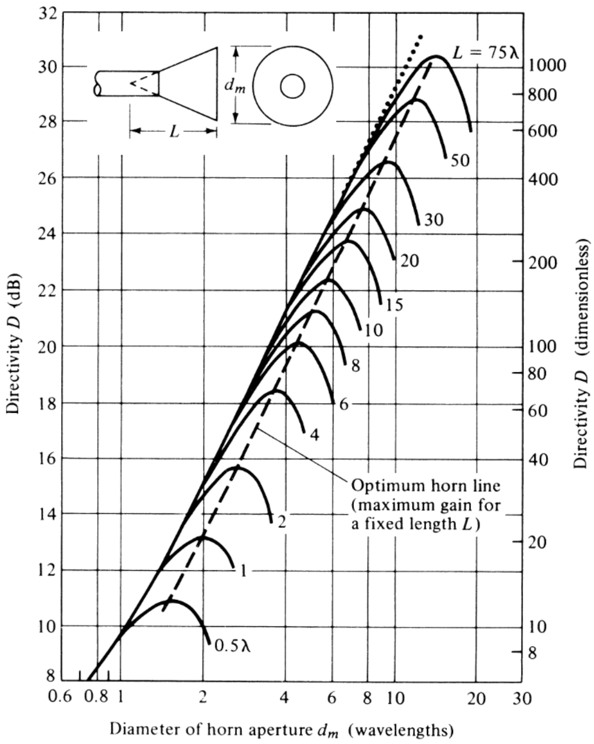

Figure 34: Directivity of a conical horn as a function of apex to aperture centre length and aperture diameter as a function of the wavelength from [22]

A deeper study on design and modelling approximations was conducted in [88], deducing a spherical phase distribution system representation would fit conical horn antennas better according to simulations (HFSS) and comparison to Gray and Schelkunoff's experimental graph. These approximations may be used for further antenna design work.

So that the horn can launch surface waves efficiently, it must also fulfil one of the requirements defined in [69] and represented in figure 35, which shows that as the ratio of the aperture to input diameter increases, the power (N) becomes constant and therefore the horn has no influence on the propagated field. In a practical case (finite conductivity), the outer diameter would have to be too large for this to take effect; even so, the aperture must be made large enough to have minimal effect on the field from the horn.

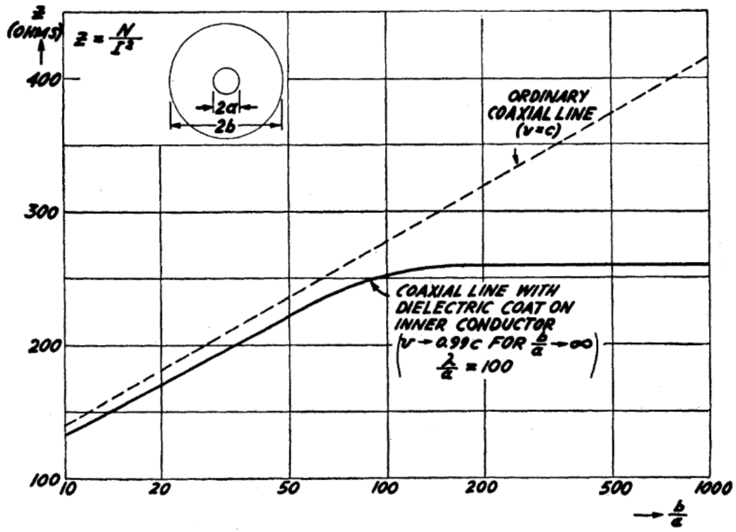

Figure 35: Effect of Goubau line horn outer diameter size on the impedance and the power transmission [20]

3.2.1 Goubau-line conical horn antenna practical designs

As it was the first option created for surface wave transmissions, many basic, as well as modified conical horn designs, have been created for surface wave transmission. One of the main modifications is the horn taper and the wire within the horn, sometimes coated with a dielectric, or corrugated, as shown in the examples figure 36.

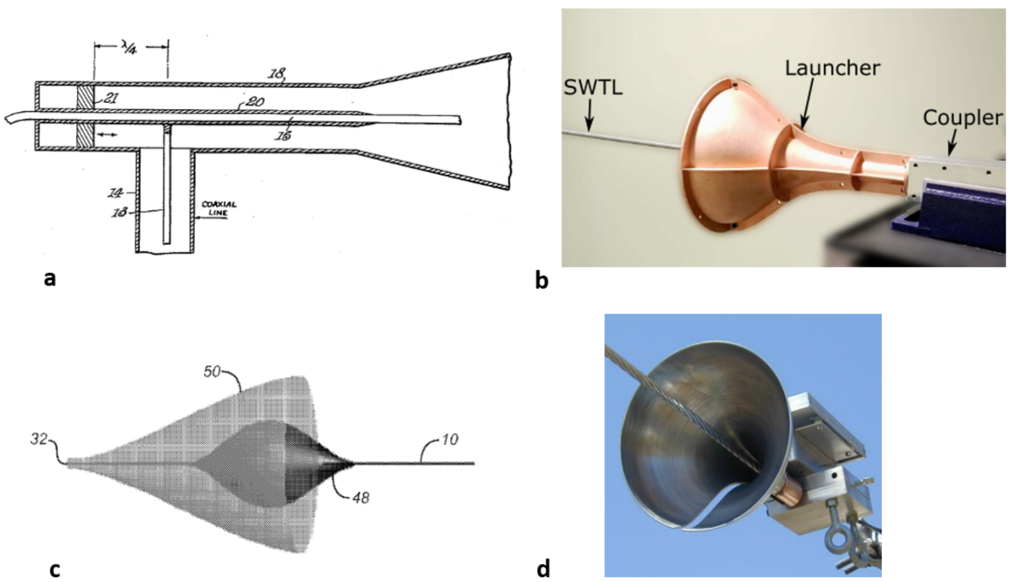

Figure 36: Example of multiple conical horn designs for surface wave transmission line, a) [23], b) [24], c) [25] and d) [26]

Horn antennas have proven to be a very good design for surface wave launching; however, they also come with a lot of restrictions. When operating at low frequencies, their dimensions are very large, making them bulky and difficult to integrate within a system. Whilst at higher frequencies, their design is difficult to manufacture and becomes costly. And in all cases, the wire to antenna alignment is also a challenge, and their fabrication is expensive.

Fortunately, a lot of other designs have been suggested over the years and can overcome some of the difficulties listed.

3.2.2 Planar launchers and coplanar waveguides

One of the most common alternatives to conical horns is planar launchers or, more precisely, antennas based on tapered coplanar waveguides. They are an obvious choice as they correspond to a planar projection of conical horn antennas, as shown in figure 37, making their design rather straightforward with a horn antenna background.

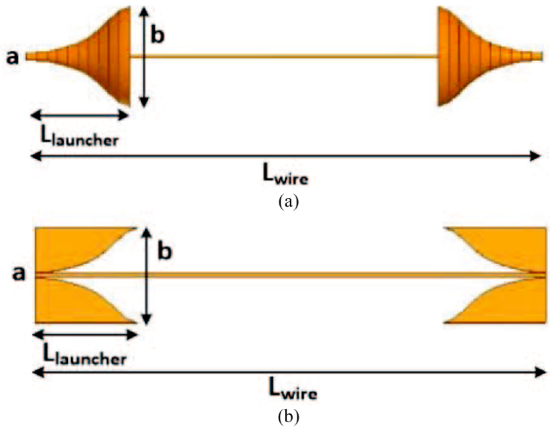

Figure 37: a) Conventional and b) Planar Goubau line transmission [27]

They first appeared along with what has been called planar Goubau lines, PGL, which is the planar equivalent of the dielectric coated Goubau wire line [76], and more precisely an ungrounded microstrip transmission line [73]. The main applications for these alternative transmission lines are THz biosensors, and high speed interconnects, such as in data centres.

An ideal coplanar waveguide, or CPW, consists of a centre conducting strip separated from, on each side, a semi-infinite ground plane, all of it on an infinitely wide dielectric substrate. They can be either grounded (conductor backed) with another infinite ground plane below the substrate or ungrounded. They support the quasi-TEM mode of propagation, similar to the coaxial feed. In terms of design, CPW characteristic impedance is proportional to the ratio a/b (see figure 38) hence easily adaptable to different sizes or frequencies. Furthermore, they can be aligned, and due to the side ground planes, the crosstalk between lines would be greatly reduced.

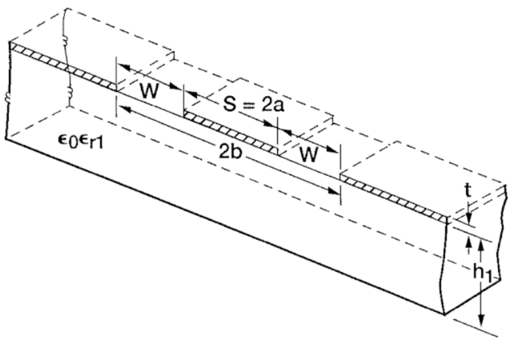

Figure 38: Coplanar waveguide structure (ungrounded) [28]

The expressions to determine CPW dimensions and main parameters such as its impedance Z_0 and its effective dielectric constant ϵ_{eff} will be defined following *Coplanar Waveguide Circuits, Components, and Systems* [28] and therefore the conformal mapping technique. A few assumptions are made in this model: the conducting strips have perfect electrical conductivity, their thickness is assumed to be 0, and the dielectric material is lossless.

The model used for the equations is represented in figure 39 and will be used to calculate the total capacitance C_{CPW}. The capacitance is divided into three parts of the CPW, however in the case considered, only part 1 remains as in the original model, part 2 is ignored, and part 3 greatly simplified. The function K is defined as the complete elliptic integral of the first kind.

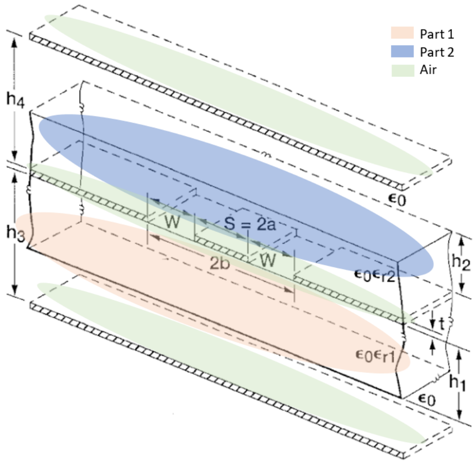

Figure 39: Full CPW representation for impedance calculation with 3 parts from [28]

$$C_{CPW} = C_1 + C_2 + C_{air} \tag{53}$$

$$C_1 = 2\epsilon_0(\epsilon_{r1} - 1)\frac{K(k_1)}{K(k_1')} \tag{54}$$

with

$$k_1 = \frac{sinh\left(\frac{\pi S}{4h_1}\right)}{sinh\left(\frac{\pi(S+2W)}{4h_1}\right)} \tag{55}$$

and

$$k_i' = \sqrt{1 - k_i^2} \tag{56}$$

Since there is no second dielectric substrate $C_2 = 0$ and since there are no outer ground planes:

$$k_3 = k_4 = k_0 = \frac{S}{S+2W} = \frac{a}{b} \tag{57}$$

so

$$C_{air} = 4\epsilon_0\frac{K(k_0)}{K(k_0')} \tag{58}$$

and

$$C_{CPW} = 2\epsilon_0(\epsilon_{r1} - 1)\frac{K(k_1)}{K(k_1')} + 4\epsilon_0\frac{K(k_0)}{K(k_0')} \tag{59}$$

From this expression, the effective dielectric constant can be calculated as the ratio of the total to the air capacitance:

$$\epsilon_{eff} = \frac{C_{CPW}}{C_{air}} = 1 + \frac{\epsilon_{r1} - 1}{2}\frac{K(k_1)}{K(k_1')}\frac{K(k_0')}{K(k_0)} \tag{60}$$

Finally, the coplanar waveguide impedance can be calculated, with c the speed of light in vacuum.

$$Z_0 = \frac{1}{c\, C_{air}\sqrt{\epsilon_{eff}}} = \frac{30\pi}{\sqrt{\epsilon_{eff}}}\frac{K(k_0')}{K(k_0)} \tag{61}$$

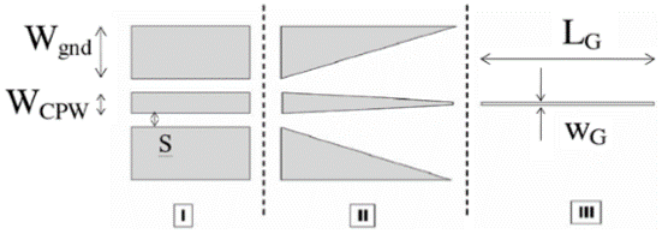

Figure 40: Structure of the coplanar waveguide to planar Goubau line transition with I the CPW, II the tapered transition and III the Goubau line [29]

In a similar manner to the coax cable to the horn antenna transition, CPWs are used to transmit the signal onto the Goubau line. And to convert the quasi-TEM mode into a TM mode, once again, the outer conductors (ground planes) will be tapered to a much larger "radius" and obtain a high "radius" ratio. Additionally, one can even taper down the Goubau line to increase that ratio, as shown in figure 40.

Because of their ease of fabrication, many taper shapes can be found in the literature and become especially complex in higher frequency ranges. Another part of the design that has been studied with great interest is the dielectric substrate. From the equations, both its thickness and (even more) its dielectric constant will impact the transmission parameters. A good analysis of the layers' dimension impact on the wave transmission can be found in [47].

Some field propagation simulations are shown in figure 41 and confirm the launching of the TM_{01} mode through the planar antenna model. In figure 42, several literature designs are shown; for example, the symmetry of c) will recreate the 3D effect of a conical horn launcher better and potentially have better coupling with the line. All these designs can also be adapted to the frequency range of interest by changing their dimensions with the presented theory.

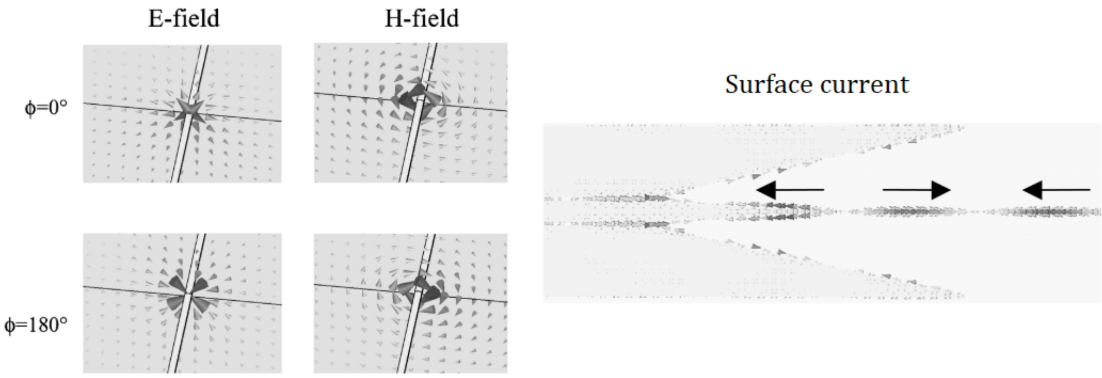

Figure 41: Simulations of Electric and Magnetic fields (left) and Surface current of a planar Goubau line [17]

3.2.3 Other possible designs: literature review

Apart from these more conventional designs, other antennas have been designed and have been surveyed for the project. These designs include corrugations which are more of a feature that can be added to either the conical horn or the planar horn antennas. They are known to improve the transmission but also sharpen the frequency of operation (less bandwidth). Ring antennas can also take many forms and launch the surface wave uniformly, they have been shown in the following papers [89] [32] [90] [91] and [92].

Another surface wave launcher consists of the SW to wire coupling with photoconductive antennas for optically generated signal (usually requires the same laser for transmission and detection). A few possible designs are shown in figure 44. They have been used for high frequency generation in the THz

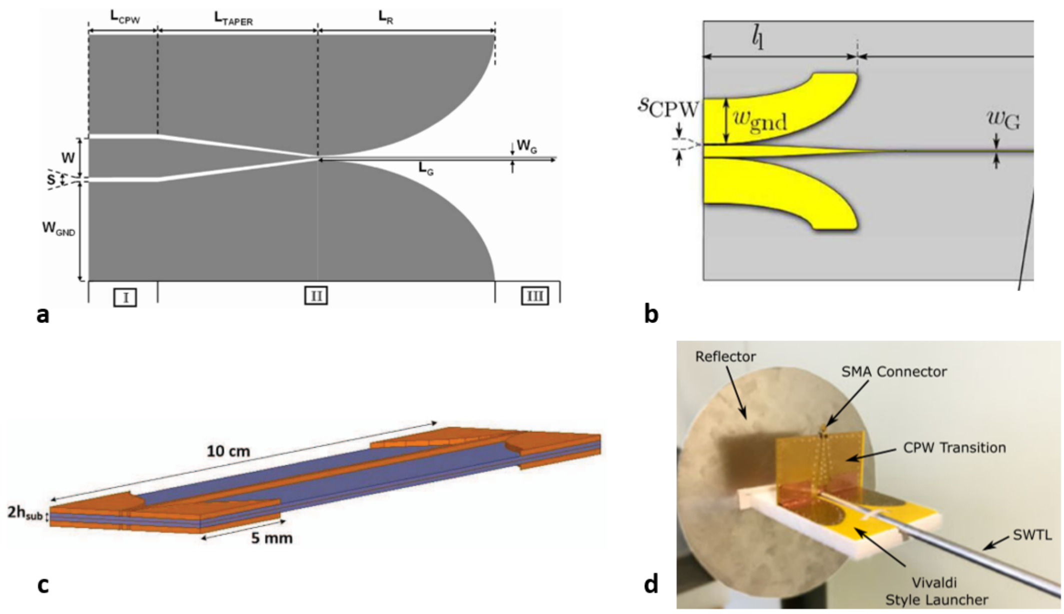

Figure 42: Examples of planar horn antennas and Goubau lines, a) modified taper [17], b) modified ground plane width along the taper [30], c) symmetrical launcher positioning wrt substrate [27] and d) planar horn launcher with non planar G-line [24]

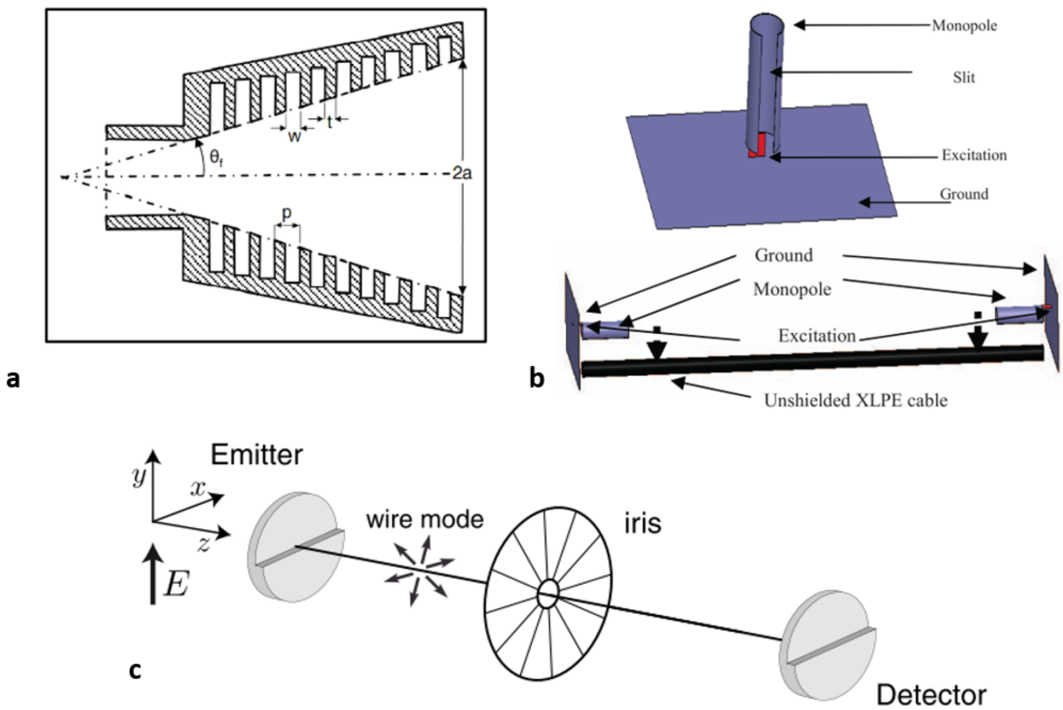

Figure 43: Other possible surface wave launcher designs a) corrugated antenna [31] b) conformal surface wave launcher [32] c) differential phase element [33]

ranges. Their coupling efficiencies are usually not as good as some of the planar horns from what was reported in literature.

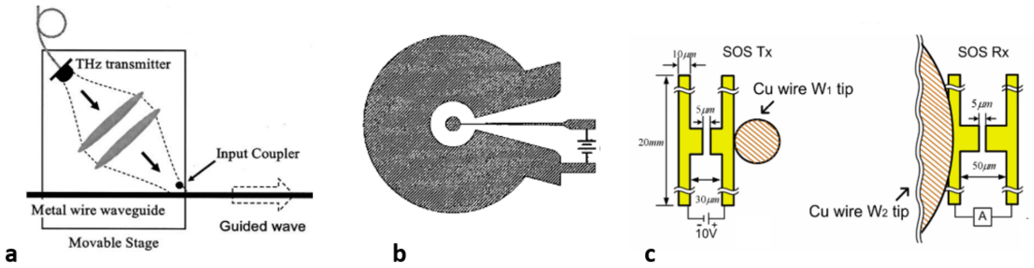

Figure 44: Photoconductive antenna designs for surface wave TDS, a) original perpendicular wire radial coupling [34] b)second antenna design [35] and c)third design with less coupling loss [36]

3.3 Wire structure

One of the main aims of the research is to reuse existing cabling networks and upgrade their data throughput. However, a good understanding of various wire structures' effects is still necessary. And further research is always possible on other applications if such structures are suited to data communications. A review of the literature on surface wave wire structures will be given in the first place, and secondly, a description of the "Drop Wire 11" (DW11) cable used in the experiments and its properties will be presented.

3.3.1 Structural properties

Binding of the wave

The overall theory for wire materials and their effect on propagating wave in terms of frequency was thoroughly defined in section 2 of the thesis.

One interesting theoretical result that has not yet been plotted is the field propagation against the radial distance from the wire core in the case of the Sommerfeld wave. This property has been plotted in figure 45 for a wire of 1 mm radius at 10 GHz and two different conductors, copper and steel.

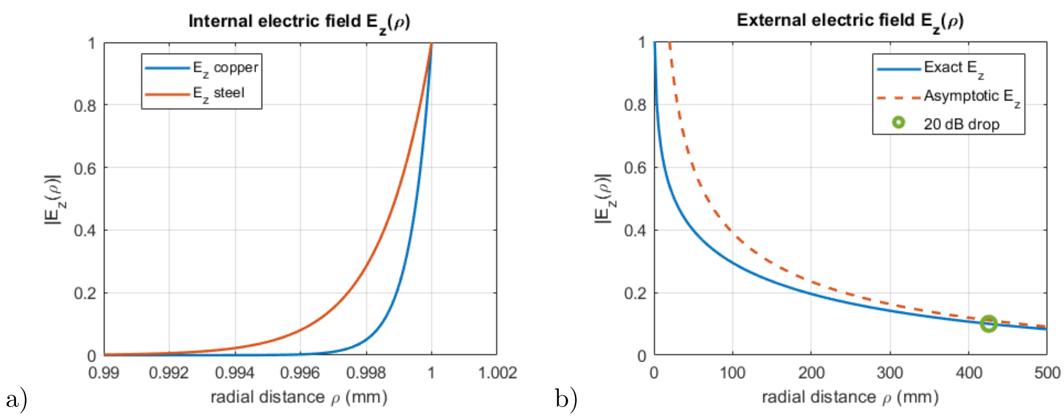

Figure 45: Electric field propagation against wire cross sectional radius at f = 10 GHz with a) the field inside the conductor and b) the field outside the conductor (in the air)

The fields are normalised so that they are equal to 1 at the metal/air boundary. In the case of the internal propagation, the amount of field within the wire is very small, only 0.005 mm radius, explaining the weak wave binding and even more so for higher conductivity materials. As for the external field extent, both conductivities have the same results, to which an asymptotic approximation of the Hankel function was compared (following calculations from [4]); they only started matching from further radial distances (about 200 mm). The 20-dB point represents the distance at which 90 % of the wave has faded, in this case around 420 mm; this value will decrease with increasing frequencies as defined in theory.

In the case of Goubau lines, a large amount of the tangential electric field would be concentrated in the dielectric layer, explaining the closer binding of surface waves in coated wires.

Wire materials

From published work on surface waves and simple theory background, common wire structures include high conductivity metals such as copper or stainless steel (silver and gold would be too expensive). And in the case of Goubau lines, low permittivity dielectric coating such as polystyrene, polyethylene or Teflon.

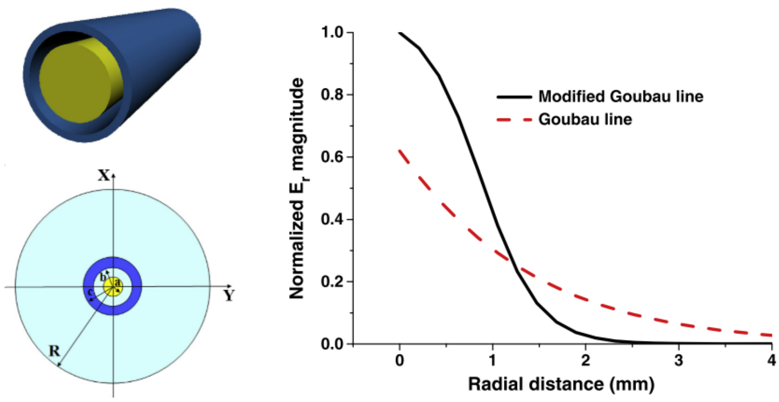

Figure 46: Structure representation (left) and normalised E_z against radial distance simulation (right) [37]

Beyond those more classic combinations, an interesting wire structure was characterised in [37]; it combines two dielectric coatings on top of the conductor, with the closest one to the core being air see figure 46. The main appeal of this idea is the change of behaviour of the field extent when it is first propagating within a low dielectric material and then a high one; it concentrates the field around the wire and has less residue (less than 10 %) power extent at larger radial distances.

Wire shaping

A more common area of experimentation is the physical shape of the wire. Some research was carried on reducing the wire diameter at its end, thus forming a conical shape [36] [93] [35].

Its advantage is the higher field concentration (less surface to share it with), and it is used at the end of the link for a more efficient wave launching and coupling. The conical wire field plots and simulations in the figure below show the electric field for a surface wave coupled with a photoconductive antenna from a 150 GHz laser pulse.

Even though the design is very efficient, the dimensions and alignment required for such results would be very complicated in a practical setup. However, this idea may be of use in planar transmission which involves much fewer alignment issues.

Multiple wires

In his initial work, Goubau already mentioned two-wire waveguides [94], and twisted pair (TP) cables [23]; the latter was thought to act similarly to a roughened wire surface which would reduce the phase velocity and concentrate the field adjacent to the transmitting media. Parallel cables have also been covered thoroughly both theoretically [95] [96] [97] and experimentally in surface wave research [38] [98] [86] [99] [100].

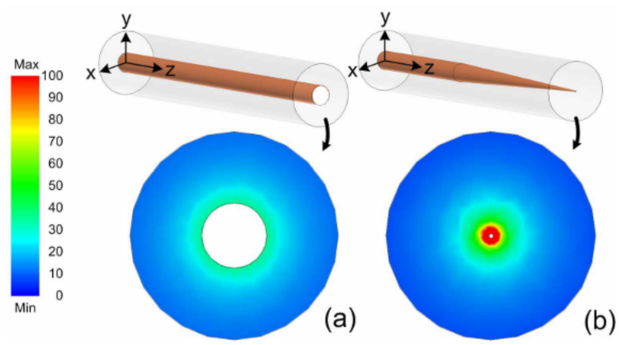

Figure 47: Simulation of the electric field distribution for a) cylindrical wire tip and b) conical wire tip [36]

They have proven to reduce bending loss, as mentioned earlier. For example, the work in [100] shows the difference between single and two-wire amplitude attenuation from wire bending, where there is a significant difference, especially as the bending increases. At a 3 cm curve depth, the two-wire output pulse amplitude is three times larger than the single wire.

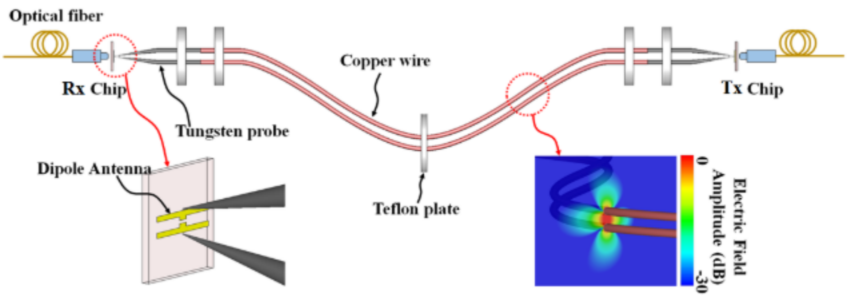

Figure 48: Setup of two-wire waveguide for different curve depths (17 cm between the two Teflon holders) [38]

In the experiments shown in figure 49, the attenuation from bending is minimal, and it brings no dispersion to the wave.

Another multiple wire cable structure was suggested in [39], consisting of a hybrid between an optical fibre and a conductor.

In this example, it seems to be used as plasmonic wave transmission. However, it could be interesting to test it for surface waves; in particular, with the higher dielectric constant of optical fibre materials, less lateral propagation would be occurring.

3.3.2 Twisted pairs and DW11 cable

With the aim of reusing the existing cabling network, this thesis's main focus is based on twisted pair cable links (amongst other structures used for initial tests). Due to either older theory or relatively recent interest in the topic, very little work has been published on surface wave transmission over twisted pairs.

This is besides some work based on millimetre-wave modes characterisation over copper twisted pairs [101]; as well as the TDSL research mentioned previously, which has been looking at twisted pair cable bundles as their transmission media. In their publications, they describe transmission over twisted-pair bundle structure mode characterisation through calculations and COMSOL simulations at mm-Wave to THz frequencies. They then use the obtained results for data rate and capacity estimates at various lengths. [11] [83]

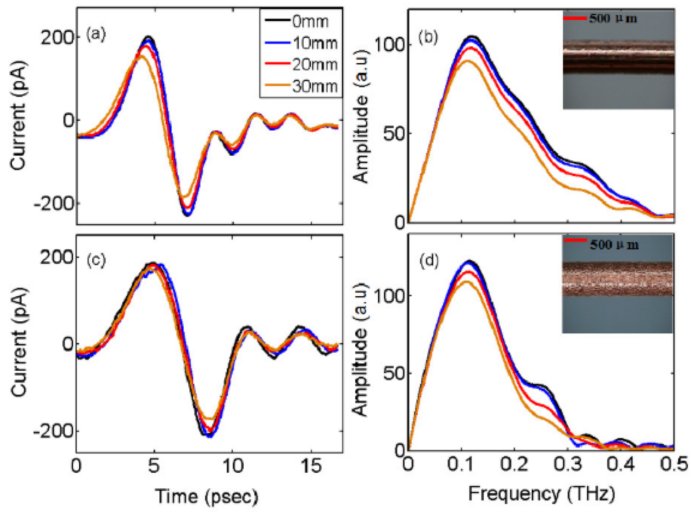

Figure 49: THz pulse propagation on bent (legend scale) coated (25 μm) two-wire waveguide with smooth (top) and rough (bottom) conductor [38]

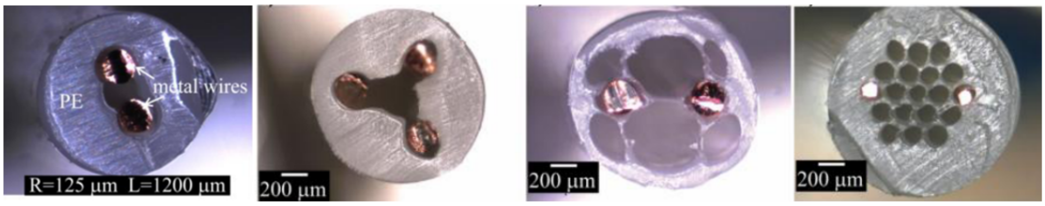

Figure 50: Different hybrid fibre cables presented in [39]

In the presented project scope, a specific cable was used for the higher end experiments; it belongs to the telephone cable network and has the potential for surface wave data communications; this wire is BT's Drop Wire 11 or DW11 [40].

a) 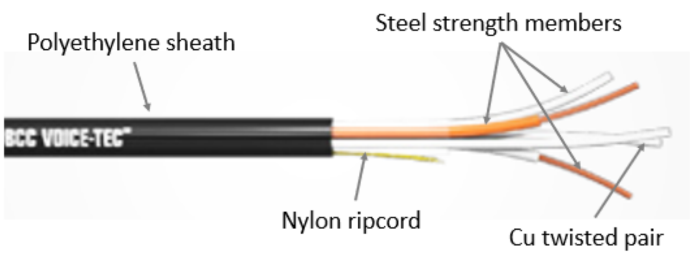

b) 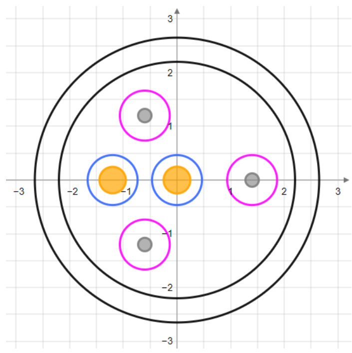

Figure 51: BT DW11 a) general cable structure [40] and b) cross-section schematic following specification's dimensions (in mm)

Figure 51, shows the structure of the cable: a single copper wire twisted pair coated with Solid High-Density Polyethylene, three straight steel strength members coated with PVC insulation, all five coated with polyester tape, a nylon ripcord, and all of which covered by a Medium Density Polyethylene jacket. Further detail about the specific dimensions and material properties can be found in [40].

This research work being a part of a collaborative project, with several research groups involved, some of their work published is also relevant to the work undertaken and presented in the thesis. Experiments were carried on the frequency response of this DW11 cable but with the steel strength members removed (basically only a twisted pair cable). The paper is exploring the effects of dielectrics on surface waves transmission similar to through wall or underground transmission [7].

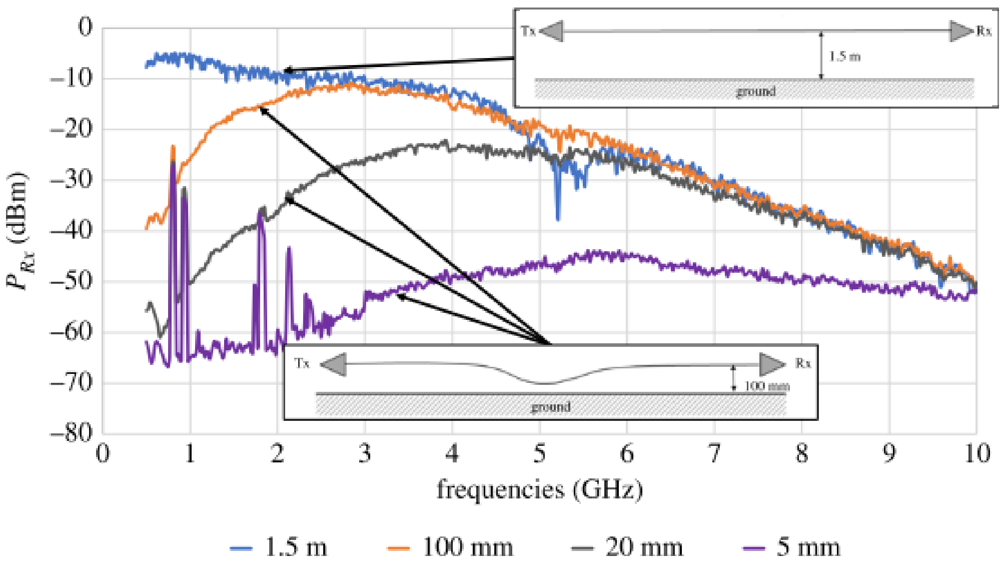

Figure 52: Received power of a 20 m TP-only (DW11) surface wave transmission launched using conical horn antennas ($P_{TX} = 0$ dBm), two different setup are shown in the insets, one with a straight cable 1.5 m above ground and one with a variable height of the middle of the cable above ground [7]

Figure 52 shows an experimental frequency response of surface wave transmission over a twisted pair cable structure in various scenarios. As the launcher properties are unknown, it may be assumed that it has a few dB insertion loss and some (again unknown) frequency dependence. The launcher loss should be taken out to obtain the cable's loss alone and calculate attenuation per unit length. In this case (with no launcher loss nor gain being removed), a maximum attenuation of 0.3 dB/m can be calculated at 1 GHz and 0.6 dB/m at 4 GHz (from the blue line).

A few conclusions can be drawn from this figure; firstly, surface wave mode was effectively transmitted over a twisted pair cable. Then, the unperturbed (blue line) frequency response is relatively uniform, and the loss increases with higher frequencies, in agreement with Goubau theory. Lastly, the results closer to the ground are mostly affected at lower frequencies and join the blue curve's trend from higher frequencies. This can be explained by the field extent of surface waves decreasing with increasing frequencies, therefore having an electric field radius inferior to the distance between the wire and the ground, once again in agreement with the theory.

Prior to testing data transmission, a frequency characterisation of the SW launchers and DW11 cable was measured using a calibrated vector network analyser (VNA) over a 5.5 metres long cable and using the launchers described in figure 60.

Looking at figure 53, there is a significant difference between the response of the general DW11 and the modified one shown in figure 52. The most obvious one is the large transmission notch between 3.5 and 4 GHz. This has been studied and proven to be an effect of the cable geometry (research results will be published in an upcoming paper). The research group ran some COMSOL simulations which showed that a twisted pair together with a straight wire produces a strong absorption peak whose frequency depends on the twist rate of the twisted pair. The notch's frequency was calculated to decrease with an increasing twist rate.

Another notable point is the difference between both setups' S21; at lower frequencies they are approximately the same, but after a specific frequency of about 2.5 GHz, the TP-only response rapidly decreases and remains about 5 dB below the all-wires launching results. Therefore, the potential higher frequency transmission range that can be seen from 5.1 to 6.1 GHz (purple and yellow curves) becomes unusable when launching only on the twisted pair (red and blue curves, as S11>S21).

It may be worth mentioning that the method used for launching the surface waves (wire soldering) was only chosen for testing purposes, and non-invasive launchers are being investigated. Furthermore,

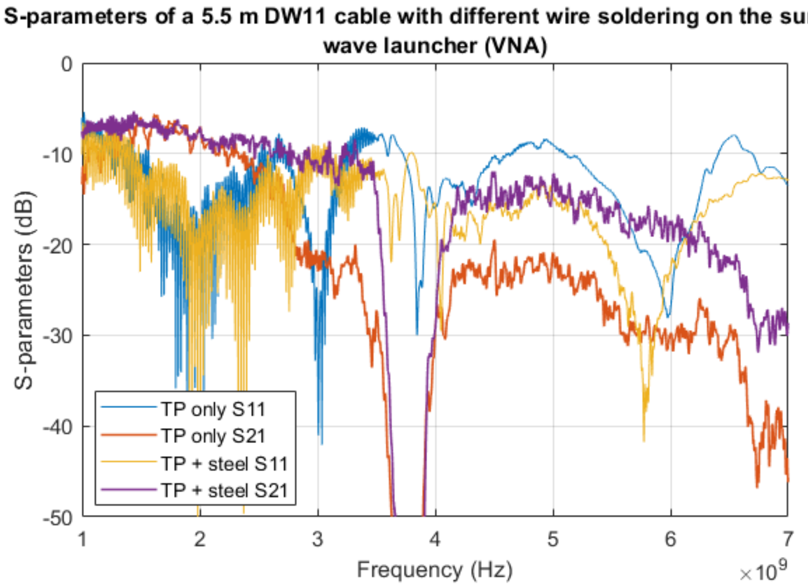

Figure 53: S-parameters of two surface wave links, a DW11 cable with only twisted-pairs soldered on the launcher (blue and red lines) and a DW11 with all cables, twisted pairs and steel strength members, soldered on the launcher (yellow and purple)

two different launchers were used for wave propagation in both figure 52 and 53, and a more optimised launcher will be presented in the following plots.

In order to further characterise the DW11 cable, the spectrum of two links of two different lengths was captured and is shown in figure 54 a). All the wires, copper twisted pair and steel strength members, were once again soldered onto the planar launcher (FR4 optimised design), and the two lengths were 6.1 m (long) and 3.15 m (short) measured from the soldering point.

The two different attenuation extrapolations in figure 54 b) have been calculated in two different manners. The first one (blue line) was obtained using S-parameters to ABCD parameters conversion, and the difference between the short and long link calculated whilst in ABCD parameters, then converted back to S-parameters, further detail can be found in the appendix.

$$ABCD_{long-short} = \left(\sqrt{ABCD_{short}}\right)^{-1} \cdot ABCD_{long} \cdot \left(\sqrt{ABCD_{short}}\right)^{-1} \tag{62}$$

For the output $ABCD_{long-short}$ ABCD-parameter, the attenuation is then calculated as:

$$att = \frac{S21_{long-short}}{L_{long} - L_{short}} \tag{63}$$

The second one was calculated assuming that S-parameters can be cascaded with the linear attenuation being:

$$att = \frac{S21_{long} - S21_{short}}{L_{long} - L_{short}} \tag{64}$$

And with L_x being the cable length. Such comparison was used to verify that surface wave link S-parameters may be cascaded as some measurements only had the transmission and not the reflection. Therefore, from the plot, DW11 has about 0.5 dB/m of attenuation around 1,5 GHz and about 1.8 dB/m around 5 GHz.

3.4 Experimental procedures and setup design

3.4.1 Experimental setups

Throughout the experimental work of the thesis, several setups were explored for various measurement types as well to keep increasing the data rate test on the characterised links and the frequency of

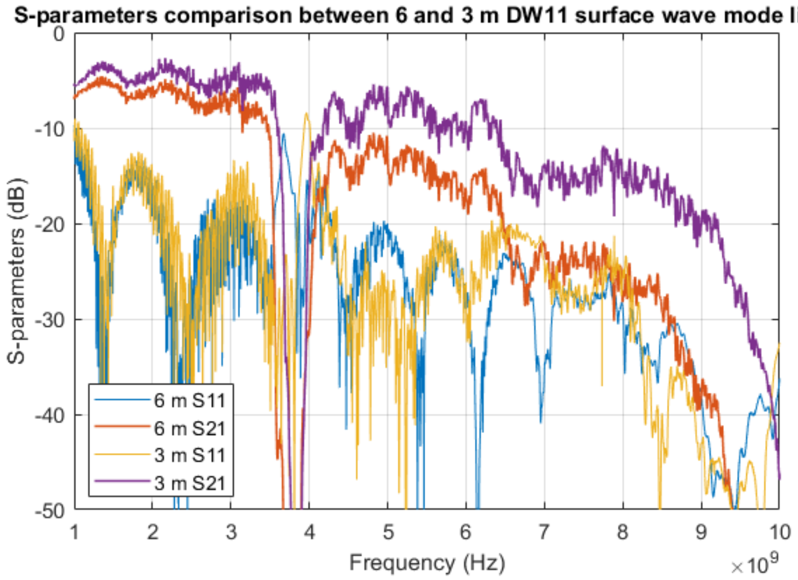

a)

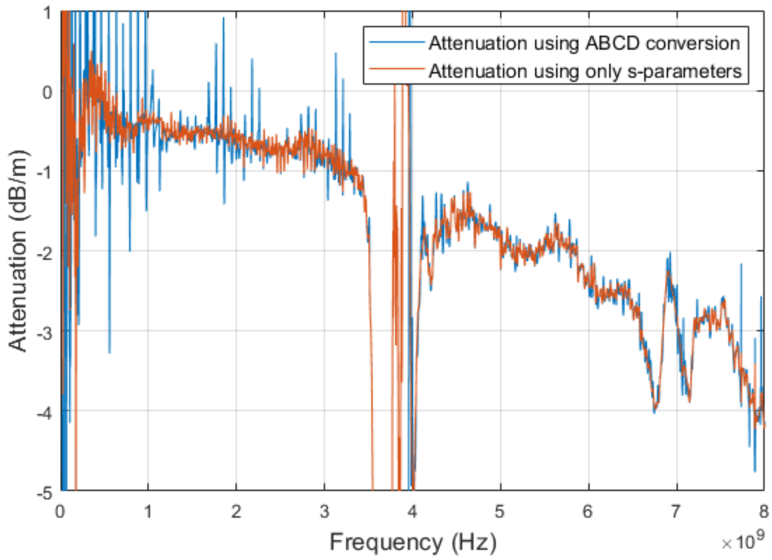

b)

Figure 54: DW11 cable measurements of 6.1 and 3.15 m cables against frequency with a) both links' S-parameters and b) the attenuation in dB/m extrapolated using two calculation methods

operation.

Amongst the presented setups, the vector network analyser, the vector signal generator and analyser combinations and the arbitrary waveform generator together with digital storage oscilloscopes.

Vector Network Analyser (VNA)

The vector network analyser setup is using the Rohde & Schwarz vector network analyser (VNA) and is shown in figure 55. A VNA can be used to characterise frequency dependent RF components or systems, with measurements such as S-parameters, noise figure, phase and group delay, Smith charts, etc.

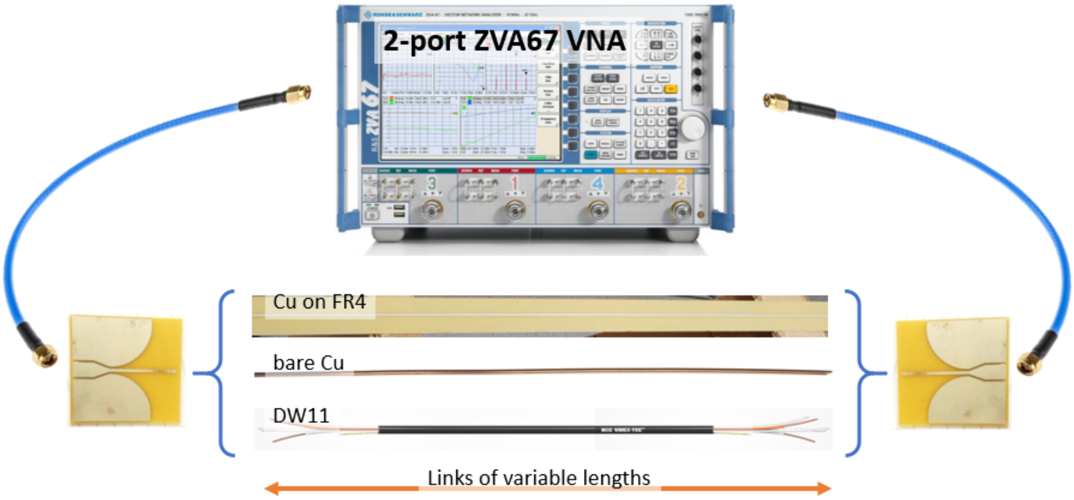

Figure 55: Vector Network Analyser experiment setup representation [41]

The VNA used was the 2-port Rohde & Schwarz ZVA67 [41], with a frequency range of 10 MHz to 67 GHz and up to 60000 points; a new calibration was done for each different link characterised or when changing the frequency range. The calibration consisted in excluding the SMA connectors from the channel response, but not the launchers as they act as impedance converters from the 50 Ω SMA cables to the various wires used as a transmission channel. The VNA setup was used to characterise various links and especially taking various cable lengths in order to obtain the specific cable attenuation per unit length, as well as characterising the different antenna designs, both magnitude and phase over a wide frequency range.

Vector signal generator and analyser (VSG and VSA)

The second setup used is an initial test setup; it is rather straightforward and well automated and gives a basic overview of a system potential for data communications. The experimental diagram is shown in figure 56.

A vector signal generator consists of a continuous wave generator with an extra baseband IQ input. As shown in the block diagram, a carrier frequency generator is mixed individually with the I and the Q inputs, which are then added to form a fully modulated and up-mixed signal. The I and Q modulators can have either internal bit input or external ones depending on the device and function as described in the previous chapter.

In a similar manner, the vector signal analyser reverses the process with first downmixing, filtering, analogue to digital conversion, and then a large number of measurements can be outputted. For example, the passband or baseband spectrum, the constellation, the detected EVM, etc.

In the experiments, various devices were used, each with different features and different complexity of data generation and processing.

The first VSG/VSA combination consisted of Rohde & Schwarz devices, with internal IQ generation and high-end data processing; two different signal generators were used for different frequency ranges

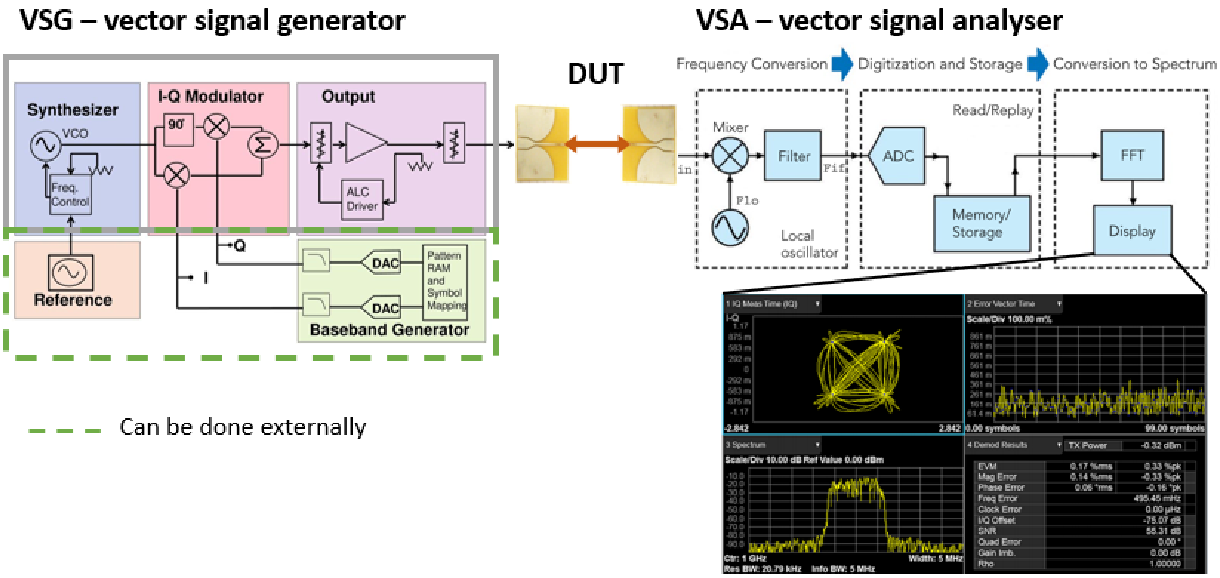

Figure 56: Vector signal generator and analyser setup digram, with a VSG block diagram [42], a generic SW link, a VSA block structure [43] and an example VSA display [44]

and maximum symbol rate characteristics. The technical specifications are as follows [102] [103] [104]:

Device	Name	Frequency range	Maximum bandwidth	Additional features
VSG 1	R&S SMW200A	100 kHz - 3 GHz	120 MHz	Supporting most digital standards (ex: 5G, LTE)
VSG 2	R&S SMIQ06B	300 kHz - 6.4 GHz	18 MHz	High output power, up to 16 dBm
VSA	R&S FSQ 26	20 Hz - 26.5 GHz	28 MHz	Eye diagram, constellation diagram, spectral evaluation ...

Table 2: Rohde & Schwarz VSG and VSA parameters

Due to the transmission bandwidth limitations (and therefore symbol rate limitations) and little control over the data sets sent, another setup was used for data transmission tests. The higher bandwidth setup is once again composed of a vector signal generator and analyser set, the Anritsu MG3710A [105] and the Anritsu MS2690A [106]. Their technical characteristics are summarised in the two following tables:

a)

Name	Anritsu MG3710A
Device	VSG
Frequency	100 kHz - 6 GHz
Bandwidth max.	125 MHz
Output power max.	23 dBm
Memory	64 MSamples

b)

Name	Anritsu MG2690A
Device	VSA (+ VSG)
Frequency	50 Hz - 6 GHz
Bandwidth max.	125 MHz
Dynamic range	177 dB
Memory	256 MSamples
Functions	Spectrum analysis
	FFT signal analysis
	Digitiser (up to 200 MHz, min. 2 samples/symbol)

Table 3: Technical specifications of the Anritsu a) MG3710A VSG and b) MG2690A VSA

In this case, to exploit the maximum bandwidth, the IQ data was generated through MathWorks Simulink software, defining the modulation format, the baseband bandwidth, the number of samples per symbol and the filter shape, and is then up-mixed by the VSG. At the other end, the received data was down-mixed by the VSA and then digitised to separate baseband I and Q data. Such digitising process required a minimum of two samples per symbol, therefore, reducing the maximum output data rate. The digitised data was once again post-processed on Simulink and Matlab software as described in the experimental chapter.

Arbitrary waveform generator (AWG) and Digital storage oscilloscope (DSO)

Further data rates requirements led to another experimental setup change, an arbitrary waveform generator (AWG), also sometimes called an Arb, together with a digital storage oscilloscope (DSO).

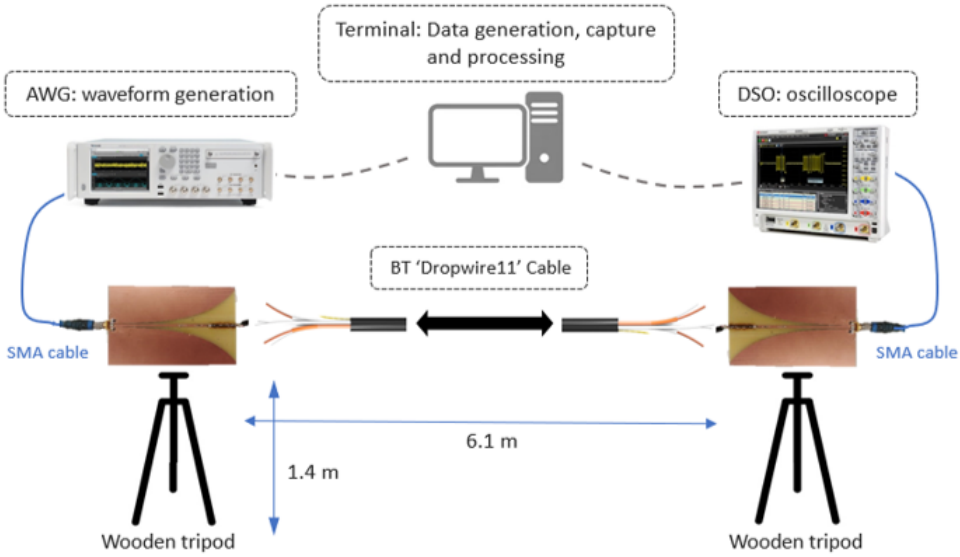

Figure 57: Representation of the lab setup for the AWG and DSO data transmsission over the DW11 link using holds and wooden tripods (for OFDM experiments) [45] [46]

An AWG is a specialised type of function generator that is able to generate waveforms from a set of entered values. Some can operate as standard function generators, including conventional waveforms, for example, sine, square, triangle, noise and pulse, and some include more complex functions. In the presented system, a formerly generated (and up-mixed) signal is loaded onto the waveform generator, the code written for data generation is summarised in figure 22 a). Then a few settings are selected, such as the sample rate clock in S/s (also referred to as f_{clock} in eq. (36)), the output amplitude, single or continuous run of the dataset, presence of markers. The AWG used was the Tektronix AWG70001A, and its relevant characteristics are as shown in the table below [45].

Name	Tektronix AWG70001A
Device	AWG
Sample rate	1.5 kS/s – 50 GS/s
DAC Resolution	8 – 10 bits
Analogue bandwidth	15 GHz
Output range	250 – 500 $mV_{p\text{-}p}$
Number of channels	1
Max. dataset length	2 GSamples

Table 4: Tektronix AWG parameters

On the receiving end, Another high-frequency band and high sample rate device was used, a digital storage oscilloscope, two of which were used depending on the experiment and device availability. The first one was a Keysight DSO404A [46] and the second one a Teledyne LeCroy WavePro 804HD [107] which was mostly used for higher carrier frequency experiments. The technical specifications of interest are summarised in the following table.

The digitised data from the oscilloscope was transferred to Matlab for data recovery and post-processing, as is shown in figure 22 b) which is a block diagram of the written code.

Name	Keysight DSO404A	WavePro 804HD
Device	DSO 1	DSO 2
Max. sample rate	20 GS/s	20 GS/s
Resolution	10 – 16 bits	12 bits
Bandwidth	4 GHz	8 GHz
RF noise density	-160 dBm/Hz	
Number of channels	4	4
Memory	100 Mpoints/channel	5 Gpoints

Table 5: Keysight and Teledyne LeCroy DSO parameters

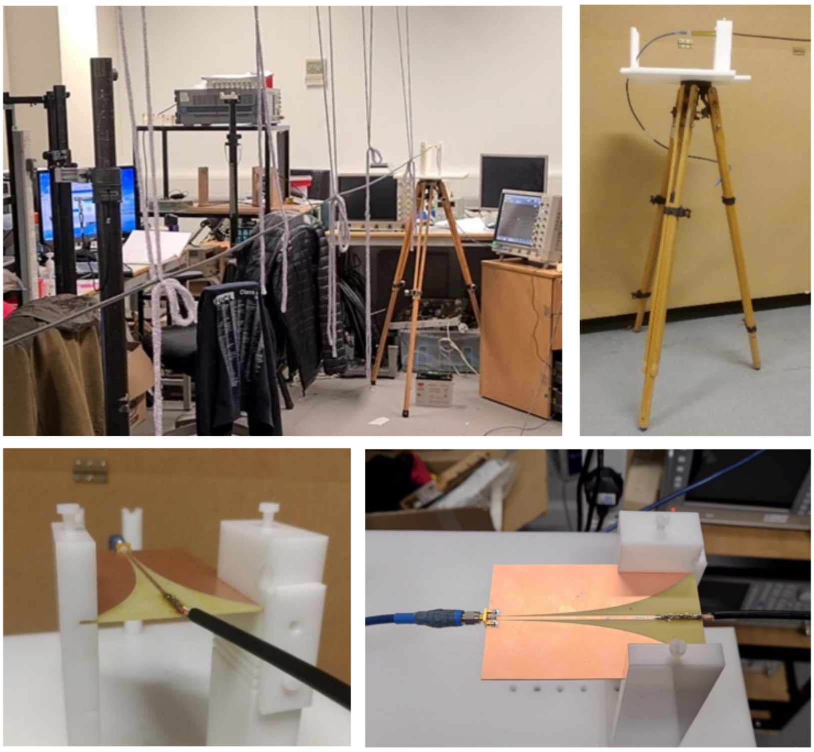

Figure 58: Pictures of the experimental data transmission setup over a 6.1 m DW11 cable using AWG and DSO setup, displaying tripods, launcher holds and cable supports

Some pictures of the actual final data transmission setup are shown in figure 58. A few extra features are shown in the pictures, such as wooden tripods that bring elevation from the ground and avoid issues with the field extent or ground plane (from the building structure). As well as a launcher hold built in a low dielectric plastic with fitting antenna slots, they have minimal effect on the launched surface wave and allow a straighter link without damaging the launchers. Finally, some cable support strings were added, once again for supporting the cable structure to further straighten the link; the link transmission spectrum has been measured with and without the string support, and it showed minimal to no effect on the channel response.

3.4.2 Surface-wave launcher designs

From the explanations in the earlier section, a more straightforward and less costly design that stood out was the planar launcher design. A few antennas have been used throughout the PhD, one self designed following the theory and adjusted through EM simulations using CST microwave. Other launchers (although only one presented in the thesis) were designed by some of the collaborating groups and optimised for the proof-of-concept transmission range of 1 to 10 GHz. The design for both the self-made and optimised launchers was based on the antenna presented by Akalin et al. in [17].

The antenna designed through CST is presented in figure 59 as well as the dimensions chosen through

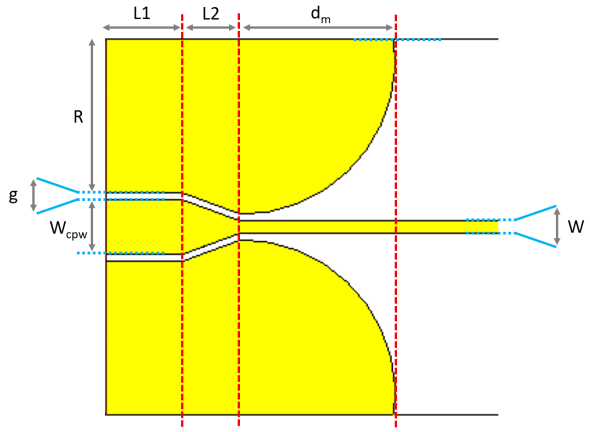

a)

Name	(mm)	Description
L1	10	
L2	7.5	
dm	20	
R	20	
g	0.95	
Wcpw	7	
W	1.5	
length	100	"wire" length from one taper end to another
h1	1.57	FR4 laminate thickness
t	0.035	copper cladding thickness

b)

Figure 59: Planar surface wave launcher design a) schematic with dimension names and b) table with dimension values chosen for the printed design

calculation and simulation adjustments in the table part b). The parameters $h1$ and t represent the PCB's properties. The antenna was printed on a copper clad FR4 laminate. The copper conductivity used was 5.87×10^7 S/m, and the FR4 properties were chosen following [108] with $\epsilon_r = 4.5$ and $tan\delta = 0.021$, however it should be noted that FR4 substrates are known to have variable properties (both production and frequency dependent).

From the simulations of a short planar link with two launchers, a few properties were calculated, firstly the simulated link S-parameters, shown in figure 60. Secondly, the reference impedance was calculated at each port, in this case being 53 ohms (expecting a slight mismatch with 50 ohms devices). And finally, electric field, magnetic field and surface current representations.

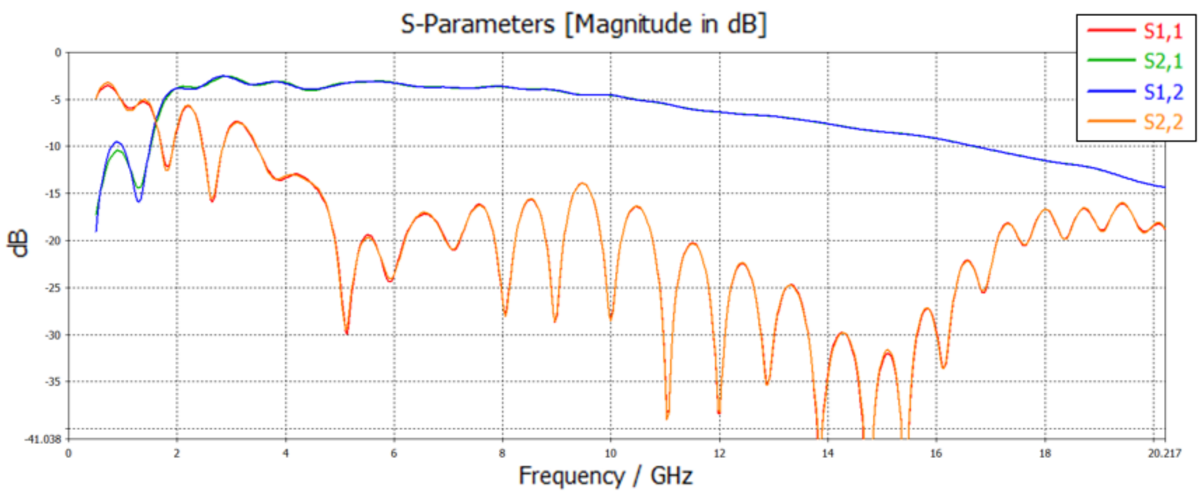

Figure 60: S-parameters of the simulated planar surface wave link in CST Microwave with "wire" length = 100 mm

A wide operating band is expected from the S-parameters simulations between 2 and 19 GHz with two areas with a higher transmission to reflection ratio, around 5 and 14 GHz. Due to both launchers being identical, S21 and S12, as well as S11 and S22, are essentially identical. The S21 remains stable from 2 to 9 GHz, after which it starts to decrease; this could be due to both Goubau line properties, with the attenuation increase with frequency, and the launcher design (material or dimensions). The substrate properties such as higher loss tangent will degrade the response with increasing frequency, as is the case for FR4's loss tangent [109]. Furthermore they are defined as a constant for all frequencies whereas they generally have a slight frequency dependent variability.

Once the design was finalised, a few antennas were printed, some individual ones for wired links as

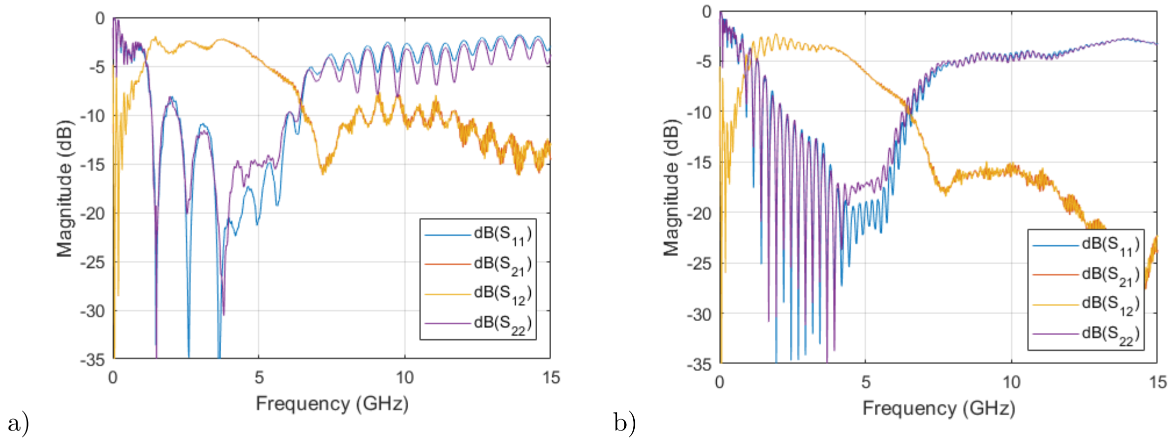

Figure 61: Measured S-parameters for surface wave planar links with a) the short 6.1 cm link and b) the long 41.2 cm link

shown in figure 55 and two fully planar links. One of the planar links is shorter and follows the simulation's dimensions given in figure 59 (pictured in figure 16), and a longer one where the only change is the parameter length. From this point onwards, the cable length will be defined from the end of the antenna, therefore from the end of d_m, rather than the end of the taper as was the case in the simulation. The shorter link has a cable length of 6.1 cm, and the longer one has a cable of 41.2 cm.

Comparing the simulated and experimental links, a lot of differences are noticeable. The main one is the frequencies of operation, and unlike the simulations, the received power significantly decreases after about 4.5 GHz. In addition, the reflection pattern is quite different even in the lower frequency range, where some sharper reflection peaks can be observed. Such poor performance in the higher frequency range has been attributed to the PCB material, which is manufactured to operate only for lower frequency ranges. Despite those differences, at lower frequencies, the transmission pattern and power levels seem in good agreement with a magnitude around -3 to -4 dB and a few ripples (assumed to be related to impedance mismatch).

Then comparing the shorter and longer planar links, the general trend remains the same between both S-parameters, with a higher number of ripples (both on the transmission and the reflection curves) for the longer planar link. This shows an operating frequency band of about 4.5 GHz between 1.5 and 6 GHz for the designed surface wave launcher.

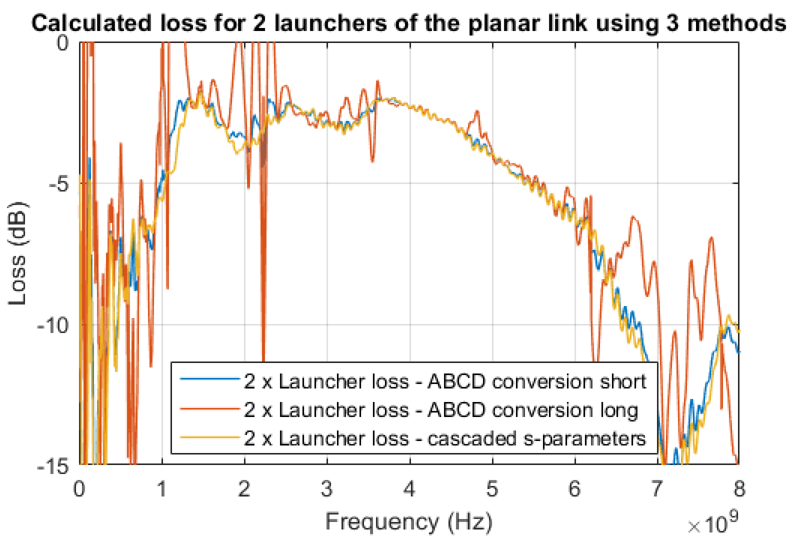

Figure 62: Calculated loss of two identical launchers from two lengths planar links using three calculation methods

Similar to the earlier process, using the two link lengths with identical antennas, the wire's attenuation and the launcher's frequency response (without the wire's loss) can both be obtained.

The two combined launcher losses are displayed in figure 62 with three different calculation methods. The first two (blue and red) were obtained with the attenuation calculated through S-parameter to ABCD-parameter conversion, and the last one (yellow line) was calculated assuming s-parameters can be cascaded (neglecting reflections). Looking at this antenna design, all three calculation methods seem to be outputting very similar results, and the cascading s-parameters resemble a smoother version of the other two calculations.

As explained for the attenuation, such extrapolation may be helpful when looking at longer links without reflection measurements and, therefore, not being able to convert to ABCD-parameters.

From this plot, a single launcher has a loss of about 1 dB at 1.5 GHz and about 2 dB at 5 GHz. Beyond the transmission range (when $S21 < S11$), the calculated attenuation and launcher loss started being unreliable (similar to the response at 0-1 GHz), hence it was not displayed.

Those launchers were built and employed as a test design for initial experiments, and therefore various setup and cable designs have been tested using them, as explained in Chapter 5.1. However, for higher-end data transmissions, some optimised launchers were provided by collaborating research groups to better demonstrate surface wave transmission capabilities in data communications.

a) 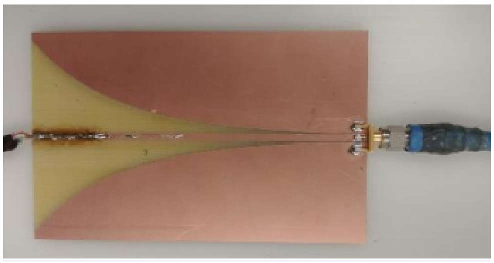

b) 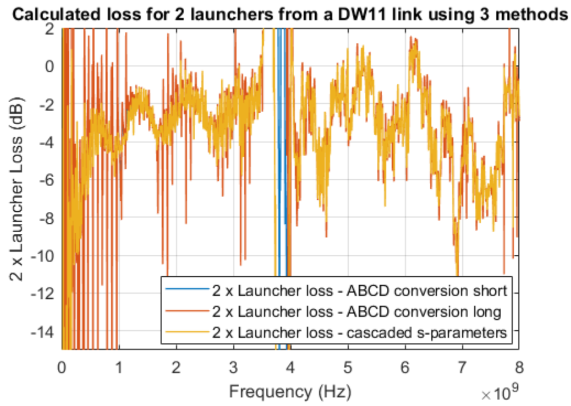

Figure 63: Optimised launcher design for GHz surface wave transmission with a) a picture of the launcher and b) the calculated loss of two launchers (the channel response can be found in figure 54)

The second design is shown in figure 63 where a) shows a picture taken from the experimental setup and b) shows the calculated loss for two launchers using the same processing methods as before and the S-parameter measurements for the DW11 link is shown in figure 54 a). Once again, the three calculations resulted in well matching curves; however, the loss obtained through ABCD conversion retained more of the irregular features of the transmission over the DW11 cable. Indeed, the initial measurements and extrapolated results have a lot more ripples (possibly noise) over them due to the length of the links. The VNA had to be calibrated with coaxial cables that would allow such a reach and frequency of operation, which may cause the irregularities. Additionally, the notch feature of the DW11 cable structure added an area of fluctuating loss in the response, which may be ignored as it was proven to be induced by the cable only.

4 Link characterisation and capacity calculation

Prior to experimental transmission further understanding of surface wave data transmission was required. As explained in chapters 2 and 3, surface waves operate over a wide frequency range, hence capacity estimates would help orientate towards a well fitted setup and experiment design. Such calculations would therefore benefit from the initial Sommerfeld wave and Goubau line models with variable parameters such as frequency, wire and dielectric radius and materials. Further simulations would also give insights on the performance of specific launcher designs and cable structures.

4.1 Shannon capacity and initial power budget

Channel capacity is defined by the Shannon-Hartley theorem; it sets a theoretical upper bound on the information rate of data that can be transmitted through an analogue communication channel in the presence of noise.

$$C = B \times log_2 \left(1 + \frac{S}{N}\right) \tag{65}$$

Where C is the channel capacity in bits per second, B is the bandwidth of the channel in Hertz, S and N are the average power of the signal and the noise, respectively, in Watts.

It assumes that the data transmitted through the channel is random and the noise is additive and Gaussian with a known power spectral density. As an upper bound, such a capacity can only be achieved with unlimited coding complexity to achieve error-free transmission. However, it provides a useful comparison of systems provided the bandwidth, average power and noise can be found or assumed. Since these variables are rarely constant, the channel is often sub-divided into smaller spectral slices, ultimately leading to the so-called water filling capacity, where the integral is performed in the limit when the slices become infinitely narrow.

Practical limitations which reduce the capacity beyond the Shannon limit are coding schemes. They typically add an overhead due to a restricted size code book to limit complexity, and an upper limit on the number of bits per hertz bandwidth, which can be achieved in high signal-to-noise ratio (SNR) channels, determined by the modulation format, though it is not included in the following calculation (data to coded and non-data bit ratio is not defined).

The attenuation of the channel (and its variation with frequency) is a key input to the Shannon capacity limit due to its effect on $\frac{S}{N}$ as the noise level at the receiver is generally fixed along with the transmit power (either by practical considerations or regulations limiting interference).

Shannon applied to SW link

For initial Shannon capacity calculations, a very simple signal transmission system was simulated; comprising: a signal source with an input power Pin, a transmitting launcher with a fixed loss $L_{launcher}$, a cable with an attenuation depending on the carrier frequency and wire length (single value over the bandwidth) and a receiving launcher with the same loss. Any RF signal processing loss and noise due to filtering, amplification and other processes have been ignored for this model. The last element required for the link characterisation is the noise, in this case, absolute theoretical limits are considered, and therefore, thermal noise is assumed for the transmitter, with its noise power spectral density being $N_0 = kT = -174$ dBm/Hz, with $N = N_0 B$.

The other system dependent parameters are the wire attenuation which was calculated with the Sommerfeld wave mathematical model presented in the earlier chapter, and the chosen frequency being the carrier frequency, f_c.

Furthermore, the launcher's loss was set as $L_{launcher} = 1.6dB$; in this case, a value based on literature and experimental designs whilst remaining realistic over a large range of frequencies.

The Shannon capacity of a 100 metre long, 0.5 mm radius, bare copper single line is considered. In figure 64 the effect of the carrier frequency is compared in the left and right side plots, assuming the same fractional bandwidth ($f_c/10$, $f_c/2$ and f_c). With f_c being 1 and 100 GHz and the corresponding wire attenuations being 0.023 and 0.42 dB/m.

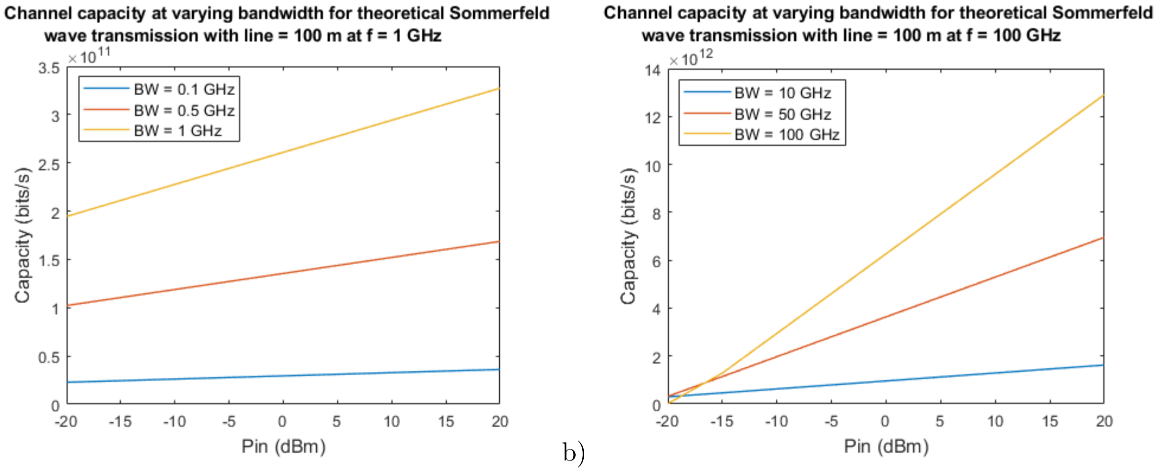

a) b)

Figure 64: Comparison of capacity limits for a) 1GHz and b) 100GHz carrier frequencies

As expected, higher bandwidth provides higher data rates, as does increasing input power. In this case, the carrier frequency to bandwidth ratio is physically realisable, and on the low end, over 0.1 Tb/s is shown, whereas, on the higher end, over 5 Tb/s is calculated. Since these simulations use theoretical surface wave attenuations and thermal noise, the data rates are absolute maxima; these can be used as limits to achievable numbers but not yet as predictions of data rates that can be transmitted through surface wave links.

Constrained Shannon model

A more realistic estimate of the available capacity can be obtained by modifying the Shannon equation to take into account the need for a particular bit error rate (BER), assuming a specific modulation format and making realistic estimates of the noise floor. The modified Shannon equation is:

$$C = \int_{f_{min}}^{f_{max}} log_2 \left(1 + \frac{S(f)}{N(f)\Gamma}\right) df \tag{66}$$

Where the loss factor is, Γ = transmission efficiency + noise margin − coding gain.

The transmission efficiency is assumed to be 9.8 dB corresponding to a BER of 10^{-7}, a 6 dB noise margin is allowed, and the coding gain is dependent on the modulation and coding employed [110]. In this case, Trellis coding is assumed, while the modulation is 16QAM, 64QAM and 265QAM. Furthermore, a maximum spectral efficiency is added; it is dependent on each modulation's power spectral density.

Unless otherwise stated, theoretical values for attenuation are used for a bare copper wire with a 0.5 mm radius. The launcher losses are assumed to be 1.6 dB each at the transmitter and receiver. In this model, the theoretical attenuation varies with the frequency, even though the changes should not be significant. Noise contributions beyond the intrinsic link (launchers and surface wave) are not explicitly included, although the noise floor was modified to DSL noise levels of -150 dBm/Hz [111], and it could be viewed as including these.

A comparison with the previous model, as well as useful insights into the general trends can be gained by considering the comparison of carriers at 1 GHz, 10 GHz and 100 GHz. As greater bandwidth is available with increased carrier frequency, 20 GHz bandwidth is considered for 100 GHz, 2 GHz is considered at 10 GHz and 0.2 GHz at 1 GHz (keeping the fractional bandwidth constant).

As can be seen in Figure 65, all modulations reach a maximum data rate due to the spectral efficiency cap at high SNR, so with a lower carrier frequency (and less bandwidth), 256 QAM can go up to 1.7 Gb/s whereas on the higher frequency band it can go up to 170 Gb/s. To accommodate the higher rate with the same transmit power and increased attenuation, the length is reduced from 1500 m for 1 GHz to 500 m for the 10 GHz link and 100 m at 100 GHz.

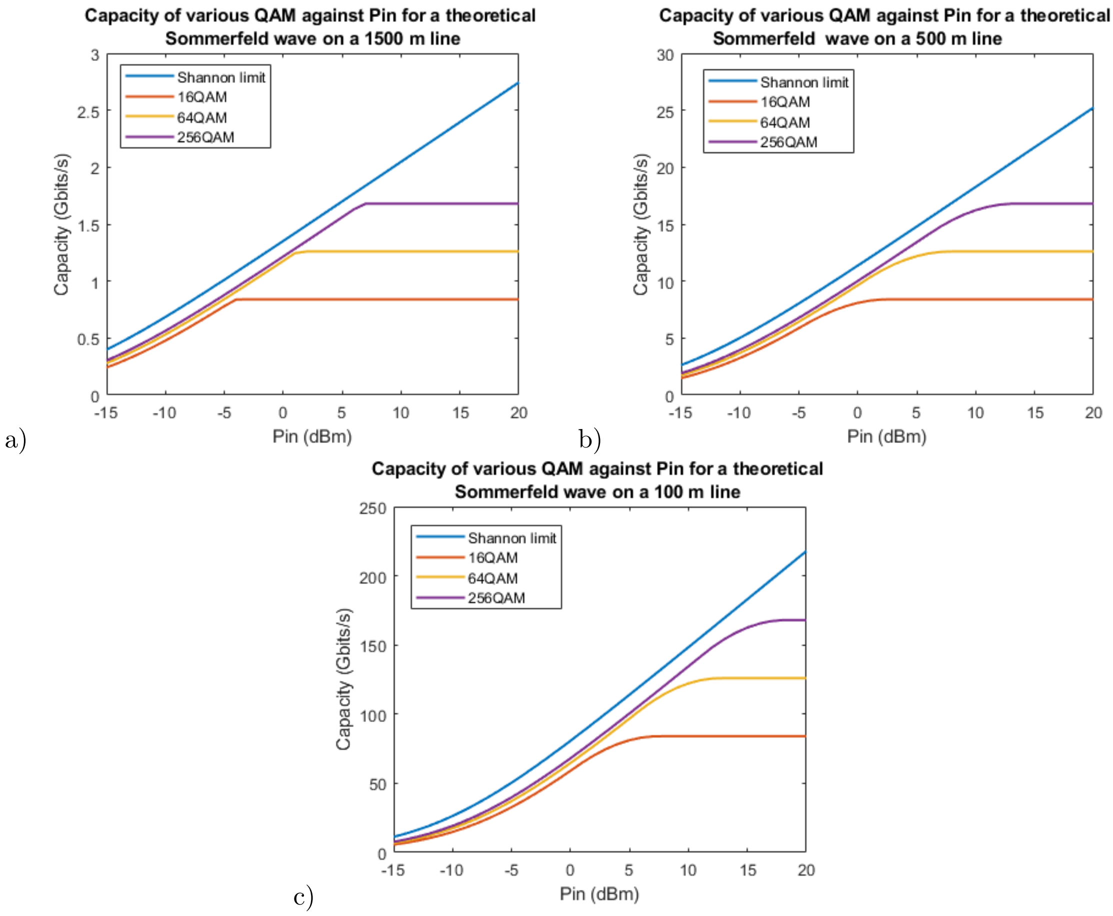

Figure 65: Comparison of 1 GHz, 10GHz and 100GHz carrier frequency with various modulation formats, and same carrier fractional bandwidth. a) f_c = 1 GHz and bandwidth = 0.2 GHz, b) f_c = 10 GHz and bandwidth = 2 GHz and c) f_c = 100 GHz and bandwidth = 20 GHz

When tested and following the formula, even with the same carrier frequency, an increasing bandwidth results in an increasing capacity. Furthermore, it can be seen that until the link saturates at high SNR, the modulation has relatively little impact on capacity.

Estimation at License-free bands

Due to the large field extent of the surface waves defined in Sommerfeld theory and the antenna mode conversion, there is a considerable risk that surface wave communications may fall within the RF wireless band regulations.

To determine whether radiative loss occurs on surface wave links, a short, straight, single wire link was connected to a spectrum analyser while the input was terminated, in a standard lab environment. The recorded spectrum is shown in Figure 66. The presence of peaks at common communications bands (around 900 MHz cellular, 2.4 GHz ISM/Wifi and 5.2 GHz ISM/Wifi) shows that both TEM and TM modes are detected and by reciprocity will be radiated. Therefore, the system must be robust to interference from external sources and must keep the interference it causes to other systems within acceptable limits. It is believed that the interference may come from the mode converting antenna rather than the actual surface wave transmission line itself, but it needs further exploration.

In order to comply with the wireless communications regulations, a few UK licence-free bands with relatively wide bandwidth were chosen to calculate data rate capacities [112]. Furthermore, simulated and experimental wire attenuations have been compared, the latter being either attenuations measured from experiments within the research group or values found in relevant literature.

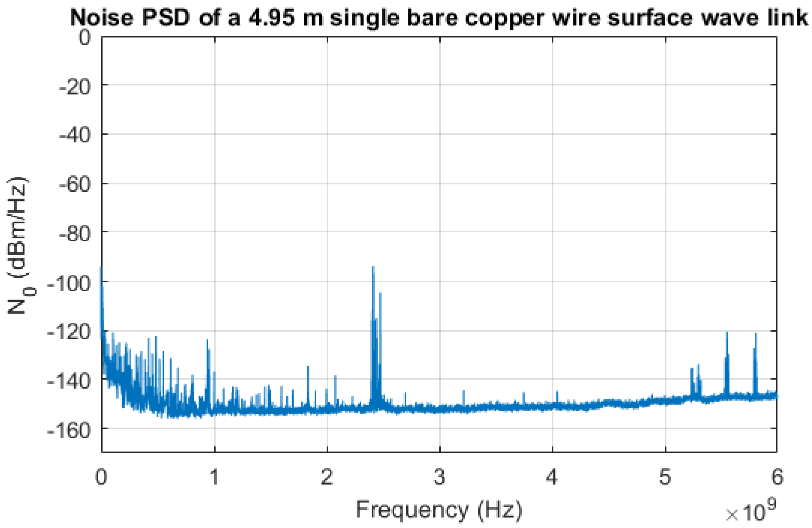

Figure 66: Recorded RF interference seen at the output of a terminated surface wave line in the laboratory environment

The 2.4 GHz ISM band represents the lowest frequency ISM band where a significant bandwidth is available (100 MHz). Taking the average noise PSD (above 500 MHz) from figure 66, the noise floor for both theoretical and experimental simulations was taken as $N_0 = -151$ dBm/Hz. The capacity as a function of input power for various modulation types is shown in Figure 67 for a 400 m line using theoretically calculated attenuation values and for a 130 m line using experimentally deduced attenuation values.

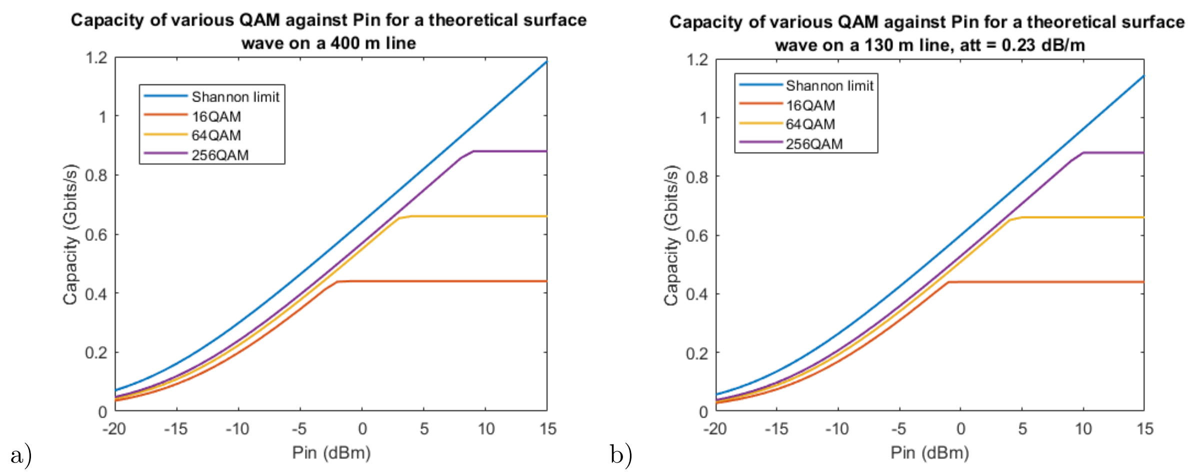

Figure 67: Capacity comparison of a) theoretical attenuation over a 24 AWG bare copper wire att = 0.063-0.067 dB/m and b) experimental data taken from unpublished collaborative data measured over a coated copper wire (d=0.5mm) (measurement resolution bandwidth (RBW) = 10 kHz)

The maximum length has been reduced to 130 m from 400 m for the experimental data for a data rate of 880 Mb/s over only 100 MHz at 256 QAM. It is worth noting, however, that the maximum equivalent isotropically radiated power (EIRP) in this band is 20 dBm, so it is possible that higher input powers would be allowable (not plotted as the curves have saturated), which coupled with 2048 QAM may lead to about 1.5 Gb/s over 100 m.

The 60 GHz band is also of interest due to the substantial bandwidth available (here using 57-66 GHz) [113] [114], the possibility of very compact launchers and the likely insensitivity to bends and objects close to the transmission line. The noise level was taken as thermal noise due to a lack of information on the noise floor at these frequencies (so realistic capacities would be lower).

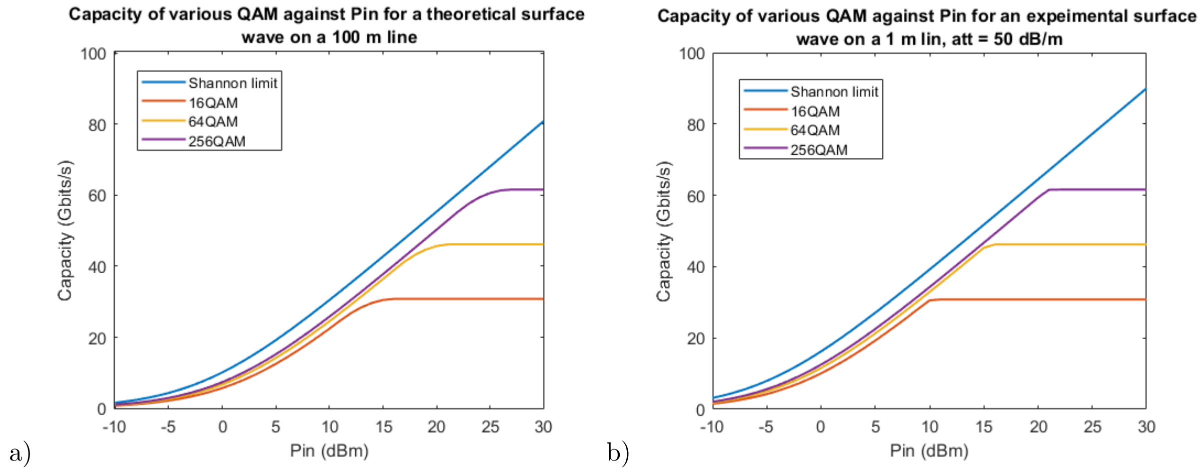

Figure 68: Capacity comparison of a) theoretical attenuation over a 24 AWG bare Ccopper wire att = 0.155-0.557 dB/m and b) experimental data from Grezkowiak and Emond's 2014 journal paper [47]

Figure 68 represents a more extreme case than the previous ISM band. Theoretical and experimental attenuations are compared for the same frequency range. However, the experimental value is extracted from a planar link designed for short distance operations with a high resistivity substrate, resulting in an attenuation of 50 dB/m compared to 0.2-0.6 dB/m theoretically. This gives an opportunity to simulate what data rates a highly attenuating or complex planar link would output. Nevertheless, it shows the potential for shorter or planar links with wide transmission bandwidths data rates up to 60 Gb/s for 256QAM.

Using different wire structures which show greater similarity between the simulated and experimental results will give a fairer comparison. It is believed that a single wire line would have a much lower attenuation in this frequency range and would result in longer transmission length for similar performance. However, the interest here was in the achievable transmission lengths for experimentally recorded attenuations rather than seeing what their true theoretical equivalent would achieve. Future work could, if needed, include such simulations, although more complex wire structures may be of greater interest.

Other licence-free bands would be of interest, such as approximately 700 MHz of split spectrum around 5 GHz with a 30 dBm max power allowed. In this case, data rates of 8.4 Gb/s were calculated for a 12 bit/s/Hz cap (4096 QAM) applied and a noise floor of -151 dBm/Hz for a single wire line. In this band, as well as the ones presented beforehand, MIMO communication could be implemented (similar to DSL) and significantly increase the data rates.

The ultimate theoretical capacity of a higher than 100 m surface wave single wire transmission line is in the region of hundreds of Gb/s, provided a sufficiently high carrier frequency can be used. The ability to reach such high carrier frequencies depends on the dielectric losses of the transmission lines.

The 60 GHz band offers the greatest data capacity for a realistic narrow band channel, with over 60 Gb/s achievable over 100 m for a Sommerfeld line using a theoretically calculated attenuation and 256 QAM modulation. Assuming the link attenuation would be much less than for a high dielectric planar link, such data rates should be achievable for longer single wire lines in a practical setup. Even assuming an attenuation 5 times the theoretical one (instead of 100), the length would be reduced to 20 m for similar behaviour (instead of 1 m).

The lower frequency bands offer, however, greater promise, with a better agreement between theoretical values of the loss and those published in the literature. Over such links, 256QAM (or higher level) modulation will be required to reach high data rates if the transmission is restricted to ISM bandwidths, with achievable data rates on the order of 5-10 Gb/s being possible over 100 m.

The frequency bands considered above comply with wireless transmission licence free bands. Even though surface waves have a high field extent it is still uncertain if this would imply them falling under wireless transmission regulations or if it can be considered as a wired technology, therefore further study would be required to distinguish which regulations to follow in the case of industrial deployment.

The modelling carried out only considers the channel attenuation and noise as the impairments produced by the surface wave channel. The effects of interference have not been considered beyond treating interferers as a source of broadband noise. Investigation of the representative noise shape and level as a function of frequency merits attention.

The structure of the twisted pair cables is more complex than single-wire lines presented here (shown in the previous chapter). When used conventionally as a differential pair, the channel shape limits the capacity for a given receiver complexity due to the highly dispersive nature of the channels, which must be compensated with multi-carrier modulation such that each carrier can be separately modulated. A basic surface wave transmission channel is not dispersive, so broadband single carrier modulation is considered here. It is likely that as the channel becomes less homogeneous due to variations in the surroundings (e.g. passing through walls), it will become more dispersive as well as more attenuating.

Comparing with the existing G.fast standard, figure 65 a) displays a 200 MHz bandwidth transmission resulting in 1.7 Gb/s with 256 QAM over 1500 m length; with a lower modulation order, similar bandwidth and much longer length, a slightly better performance is achieved. (G.fast reaches 1-2 Gb/s at 50-100 m).

4.2 Water-filling capacity

The surface wave link capacity was estimated from an extension of Shannon capacity theorem. These calculations therefore allowed us to set an upper limit on what would be achievable for a given launcher and wire link.

When evaluating surface waves as a communications channel, one of the first steps is to look at the uniformity of its frequency response. For transmission bandwidths beyond a few hundred megahertz, the channel response becomes quite irregular with some low pass response and would require complex data generation and equalisation to reach low BER. It is anticipated that the effects of interference and coupling of wires will exacerbate this effect.

As in most high data rate standards, a solution is to use multicarrier modulation, such as discrete multitone or OFDM, such that the channel effect experienced by each carrier is flat. To predict the capacity over such channels and perform the most efficient power and bit allocation a water-filling algorithm is used. It is assumed that the frequency response of the channel is known to the transmitter.

4.2.1 The Water-filling algorithm

The water-filling algorithm states that the "input power should be allocated to different frequencies in such a way that more power is transmitted at those frequencies of which the channel exhibits a higher signal-to-noise ratio and less power is sent at the frequencies with poor signal-to-noise ratio" [12]. In this thesis, the algorithm used was based on [115][48].

There are two types of water-filling algorithms the rate maximisation (RM), given a fixed power budget, and the margin maximisation (MM), given a goal data rate. Both are based on the following two reciprocal equations:

$$b_i = log_2\left(1 + \frac{P_i . g_i}{\Gamma}\right) \qquad P_i = \frac{2^{b_i} - 1}{g_i} \tag{67}$$

Where b_i is the capacity of each sub-carrier, i. P_i is the power allocated to the subcarrier and Γ is the SNR gap which is given by (transmission efficiency + noise margin − coding gain) and is dependent on the modulation format and coding of the subcarrier. The subchannel signal to noise ratio g_i is given by:

$$g_i \equiv \frac{\mid H_i^2 \mid}{N_i \Gamma} \tag{68}$$

Where H_i is the channel response, and N_i is the subchannel noise.

The total bit rate is the sum of all b_i, and similarly, the total power is the sum of all P_i. The steps of the algorithm are:

1. Compute subchannel signal to noise ratios g_i and sort them in descending order.
2. Compute the water-filling level or NSR (noise to signal ratio) K_W, allocate the power budget among the subchannels and determine the number (M_{ON}) of subchannels to be used (point of intersection with ${g_i}^{-1}$).
3. Allocate power to subchannels and apply PSD mask.

$$P_i = \begin{cases} Pmax & \text{if } g_i^{-1} + P_{max} \leq K_W \\ 0 & \text{if } g_i^{-1} \geq K_W \\ K_W - g_i^{-1} & \text{otherwise} \end{cases} \tag{69}$$

4. Allocate bit loading to subchannels (using initial equation), apply maximum bit loading cap and round it down to give it integer values and reorder the subchannels. (After the bit loading cap has been applied, the power allocation can be recalculated as reduced bit allocations will require less power.)
5. Calculate total power used and total bit rate produced.

The algorithm process is illustrated in figure 69, where ${g_i}^{-1}$ the subchannels' NSR is plotted against the ordered subchannels. The circled area, firstly orange, is the intersection between the calculated K_w (blue circle) and the ${g_i}^{-1}$ curve to determine the M_{ON} subchannels turned on ($M_{ON} + 1$ onwards are turned off). Similarly, after the unused power budget reallocation, a few extra subchannels can be turned on until the green circle point(subchannels $M_{ON}^{new} + 1$ onwards are turned off). The dashed curve represents the power cap $\overline{P}$ which is applied for subchannels 1 to $\overline{M}_{ON}$ or $\overline{M}_{ON}^{new}$.

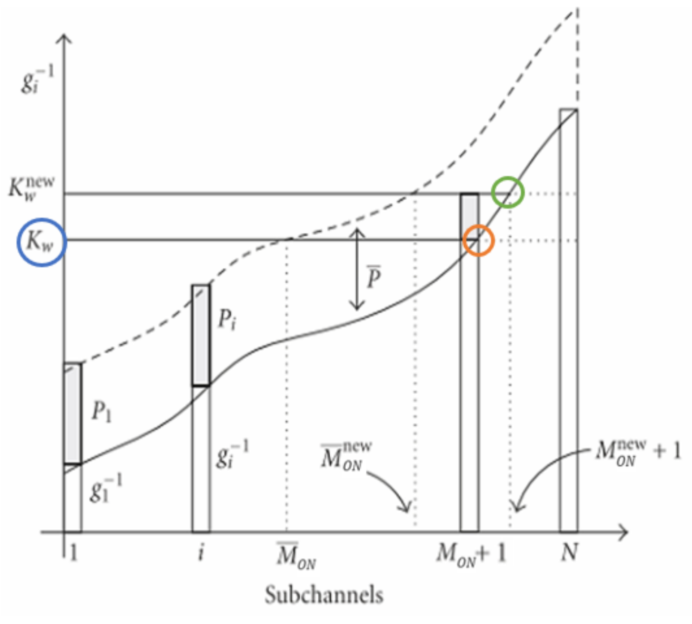

Figure 69: Graphical representation of the iterative Water-filling algorithm from [48]

4.2.2 Model parameters

From the brief introduction to water-filling algorithms given above, it can be seen that several parameters must be defined. Using data from other data transmission standards, initial SW measurements, and measurements given by collaborators, the following parameters have been reviewed and given some realistic settings.

Noise level

Looking at DSL transmission, it typically uses a noise level around -150 ± 5 dBm/Hz [111], significantly above the thermal noise limit, representing noise-like interference and the noise figure of the receiver.

The measurement of the noise power spectral density over a single bare copper wire of 4.95 m is shown in figure 66. Outside of the interference bands, there is a noise level of about -150 dBm/Hz, which is limited by the spectrum analyser used. Due to the nature of the bare copper wire, it is expected to be more sensitive to interference than other coated wires. The experiment has been repeated with other wire lengths and structures and outputted similar levels. It is also worth pointing out that in outdoor environments, the level of interference is likely to be lower and in different bands. However, the system will still need to be robust to interference.

PSD mask

Power spectral density (PSD) masks are constructed from a combination of limit PSD mask (LPM), subcarrier mask (SM), PSD shaping mask (PSM), low-frequency edge stop-band mask (LESM) and notching mask (NM) (to avoid interference with other RF transmissions).

Due to the presence of interference on the link, and the reciprocal nature of antennas, it is reasonable to expect that radiation from the launchers (and/or wire) will also exist. As a result, regulatory restrictions are likely to limit emissions in sensitive bands. Exact limits vary by region due to different uses of the spectrum. According to the ITU-T G.fast standards, a valid range of PSD ceiling values is from -50 dBm/Hz to -100 dBm/Hz [60].

Based on the guidelines for the mask of RF transmission over coax cables, a mask model could be built for surface wave communications when the transmission design is more set. In the simulations, the highest limit was applied with a max transmit power of -50 dBm per Hertz. Due to the novelty of surface wave communications it is expected that a different spectral mask would be required for this transmission.

Launcher response

Loss measurements and simulations have been provided by collaborating research groups. Examples of a calculated launcher loss (both transmitter and receiver) are shown in figures 62 and 63.

Ripples have been observed in launcher responses both in simulations and in experiments. These are due to some impedance mismatch between the coax and launcher and launcher and surface wave transmission line. As the transmission line length increases, this effect becomes less significant due to the attenuation of the reflections by the line.

Wire loss and attenuation

Two or more lengths channel responses of the same cable link have been measured such that the cable response can be de-embedded from the launchers. Their attenuation was calculated and therefore allowing the capacity to be scaled to longer wire lengths for several wire structures. As described in the experimental setup and introduction, the DW11 cable being the cable structure studied over the project, this simulation focuses on this structure.

Maximum bit loading and Power budget

The power budget, defined as the maximum power allowed over the whole frequency band, is governed by both regulations and the driver amplifier design. The amplifier is likely to be limited by thermal power considerations owing to the need for highly linear amplifiers for OFDM signals and the poor efficiency of linear amplifiers. The maximum bit loading is determined by the complexity (and therefore cost) of the transmitter and receiver hardware. As a starting point, it is proposed to use values based on current wired communication standards such as G.fast and G.mgfast.

4.2.3 Calculations for experimental data transmission links

Output power and capacity have been predicted for one of the links presented in the experimental setups using the water-filling algorithm. In order to fit the experiments section 5.2.2 closely, its parametric restrictions have been applied to the capacity simulations. Some of which have been varied to understand the systems behaviour better.

Amongst those, the channel response of the DW11 cables and the noise power spectral density response represented in figure 70 b) and c).

Further system parameters, taken as close to the experiments as possible, are presented in the table figure 70 a).

With the parameters of the simulation defined, the channel and noise responses are truncated and fitted with the defined number of subcarriers. From these, each subchannel's signal to noise ratio, g_i, is calculated, and so is the water-filling level K_W, both of which are represented in the descending order in figure 70 d). In this case, there is no crossing between the signal to noise ratio and the water filling level; therefore, all subchannels will be used (expected for such lengths).

Property	Value
Carrier frequency (fc)	2.1 GHz
Bandwidth	2083 MHz
Subcarriers (Nc)	2048
Coding gain	6 dB
Noise margin	6 dB
BER	10^{-7} (=> 9.8 dB)
PSD mask	-50 dBm/Hz
Input power budget	10 dBm
Bit cap	15 or 6 bit/s/Hz

a)

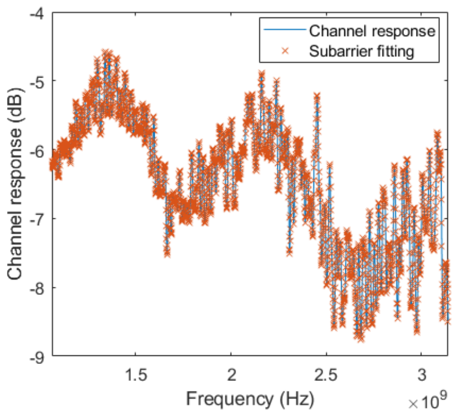

b)

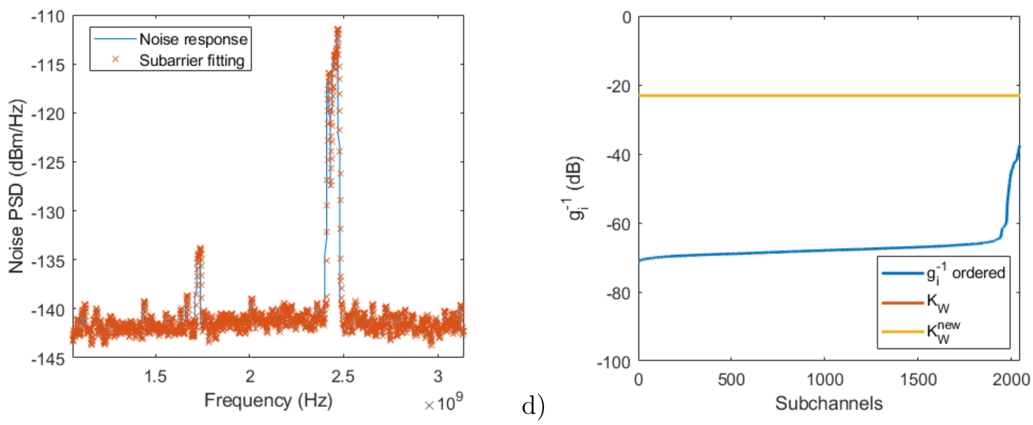

c) d)

Figure 70: Channel parameters used for the water-filling algorithm a) simulation parameters table, b) 6m DW11 link transmission response, c) measured noise level (on a 1.5m single wire line) and their subcarrier fitting and d) the computed NSR g_i^{-1} in ascending order

After calculating each subchannel's power and bit loading as described in the algorithm equation (67), their respective bit, total power cap and PSD mask limits are applied. The bit level calculated was rounded down to have only integer values, and the power was recalculated.

In the first case considered, the limit defined in the simulation parameters is clearly displayed on the resulting power and bit allocation figure 71 a) and b). The power levels remain much lower than the PSD; therefore, the max transmit power (set at 10 dBm) is the main limiting factor. A large correlation between the bit allocation and the noise level is noticeable, reducing the transmitted bits at the frequencies suffering higher interference.

The simulations have been repeated for a case closer to the experiments section 5.2.2, setting a bit

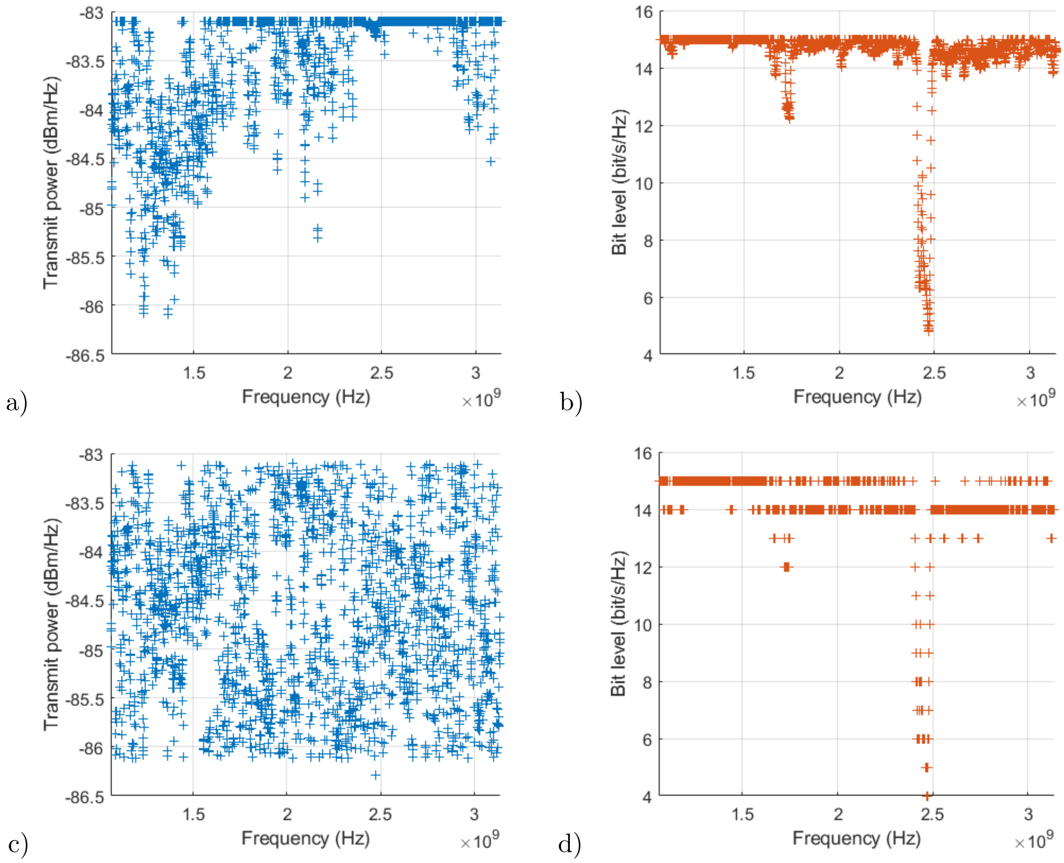

Figure 71: Simulated results for the 6.1 metre link a) transmit power per subchannel, total sum **Ptot = 9.65 dBm** b) transmitted bit per subchannel, total bit rate **R = 29.6 Gb/s** c) transmit power per subchannel floored, total sum **floored Ptot = 8.57 dBm** d) floored bit per subchannel, total bit rate **floored R = 28.8 Gb/s**

cap of 6 bit/s/Hz; the results are shown in figure 72. With a total power of -7.1 dBm, a bit rate of 12.2 Gb/s is predicted when rounding the bit levels allocated down. In this case, the power distribution can be seen to vary with the SNR of each carrier as the bit level limit is reached. With 6 bit/s/Hz due to the short transmission length, the bit allocation is constant accross the carriers, which resembles experimental transmission using a fixed bit loading.

Further simulations were performed with various power budgets and bit loading restrictions which are shown in figure 73. A 6.1 m link was used and other parameters are defined in the table in figure 70 a); the experimental noise level used is displayed in figure 70 b). The power budget P_{budget}, corresponds to the maximum allowed launch power in the simulation and may be higher than the actual launch power used depending on the parameters chosen.

The simulations with a varying power budget show that for such a short link, the maximum data rate is reached from about 5 dBm of power budget (a slight increase in both power and bit rate is seen after P_{budget} = 15 dBm but is not significant compared to the additional required power). The data rate corresponds to all subcarriers transmitting 15 bits/s/Hz resulting in a maximum rate of 30.67 Gb/s. On the varying bit cap graph, there is no capped area as the power never reaches the 10 dBm limit, and as expected, the data rate increases with increasing bit/s/Hz. On both plots, the slight irregularities are mostly due to the measured noise response included in the simulation. When running the same simulations with a single fixed noise level (- 150 dBm), the maximum data rate is reached from a lower power budget (5 dBm) and using less floored transmit power (1 dBm). However, the response against varying bit cap has a very similar trend to the one with an experimentally measured noise level.

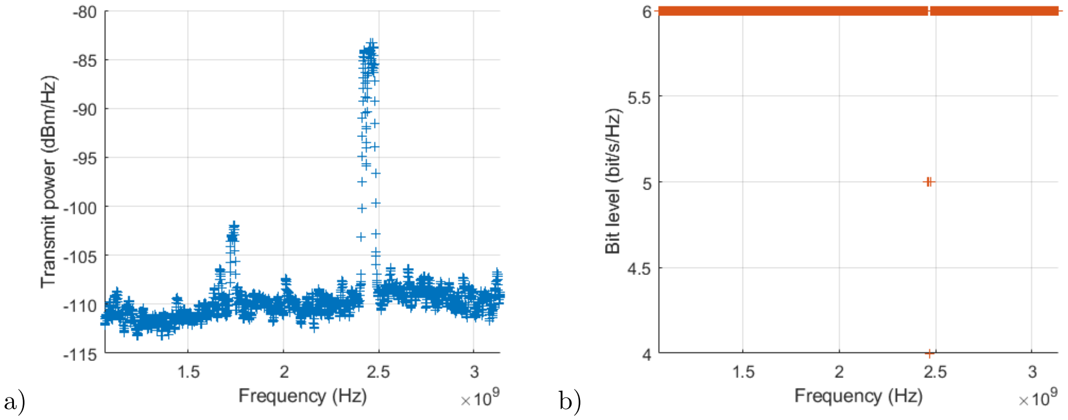

Figure 72: Simulated results for the 6.1 metre link with 6 bit/s/Hz cap with a) the transmit power per subchannel floored, total sum **floored Ptot = -7.1 dBm** and b) the floored bit per subchannel, total bit rate **floored R = 12.2 Gb/s**

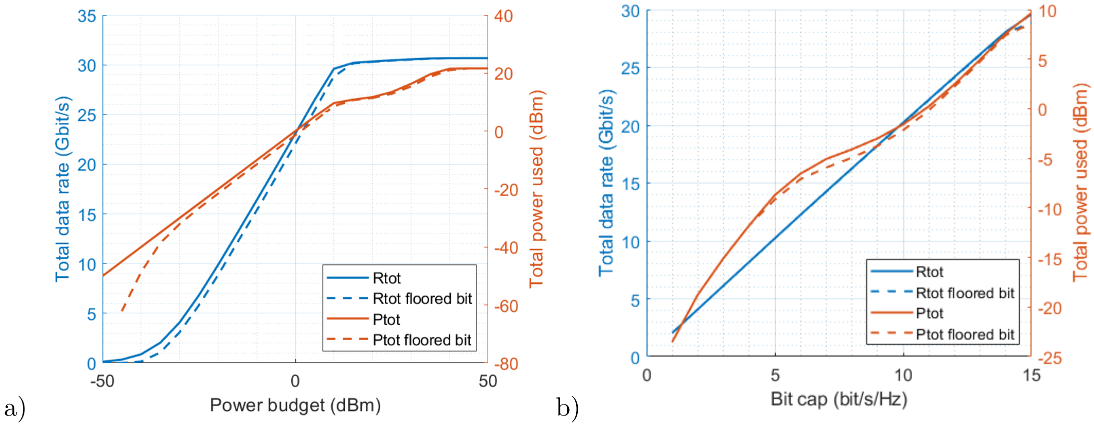

Figure 73: Calculated effect of a) total power budget (bit cap = 15) and b) bit cap (P_{budget} = 10 dBm) on the data rate and total transmitted power on a 6.1 m link with a max PSD of -50 dBm/Hz

The three different capacity calculation methods have been used to predict data rate, transmission distance and power budget of various scenarios and with more or less precision. The Shannon limit is used to calculate the theoretical maximum capacity of a surface wave link with parameters from Sommerfeld theory. Then, to give closer to expected predictions of data rates and transmission lengths, an extension of the Shannon-Hartley theorem can be used. It allows integration of modulation and coding as well as choosing a frequency dependent attenuation and noise level either from theoretical or experimental results. Finally, the water-filling algorithm allows precise calculation of bit and power loading for a known channel response and noise power spectral density. Such a simulation can be extended with attenuation and launcher response calculation and changing physical link parameters to go beyond the current laboratory capacity.

Simulations on the 6 m link showed that the operating bandwidth of surface wave transmission is much wider than differential signalling. Capacities have been predicted for a shorter wire (to compare with the lab experiment setup), however, data rates of up to 30 Gb/s were obtained for a spectra efficiency of 15 bit/s/Hz and 22 Gb/s for 12 bit/s/Hz. This is well beyond G.fast results with up to 2 Gb/s, even at more comparable lengths [2].

5 Experimental data transmission

Surpassing short to medium length current wired technology requires a large amount of bandwidth, but unlike twisted pair standards, surface wave will only accept bandpass data transmission. The frequency of operation, as mentioned earlier will depend on the designed surface wave launcher, the structure of the wire and most likely availability of unlicensed wireless frequency bands due to lateral wave propagation.

In this chapter, different setups were attempted in order to reach a proof-of-concept experimental link with maximised data transmission.

5.1 Wideband QAM data transmission

The initial surface wave experiments will be carried in the following section. A data transmission with QAM modulation was chosen due to its high spectral efficiency. The setups presented in section 3.4 were reviewed with the aim of reaching link maximum capacity and experimenting with different link structures and transmission parameters. The performance of data transmission was evaluated with the error vector magnitude (EVM) and BER as well as through several parameters and graphical representations.

5.1.1 Narrowband transmission

In the following experiments, the surface wave link consisted of a 6.1 cm (shorter) and a 41.2 cm (longer) planar link as in figure 61, they represent a close to ideal case scenario with perfect launcher to wire transition and a perfectly straight wire. Furthermore they do not require a specific setup such as launcher holds and wire straightening methods.

A vector signal generator and analyser combination was used for data transmission up to 100 MHz bandwidth (parameters in table 3); this setup allowed control over the data generation and processing as well as preloaded datasets (not used).

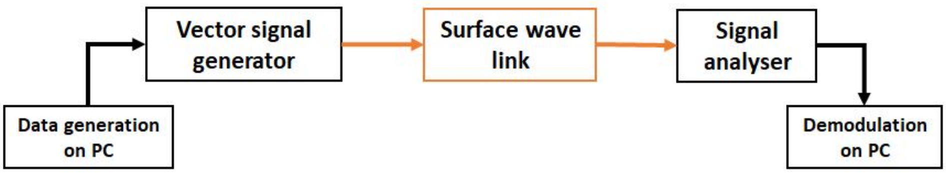

Figure 74: Diagram of the second VSG and VSA setup including on PC data generation and processing

A system diagram of the the data transmission process is shown in figure 74, the data was previously generated on a PC using a Simulink baseband QAM data generation simulation. The data is uploaded on the VSG which performs the frequency up-mixing and saved after transmission at the output of the VSA in IQ form. This received data is processed on the computer through another Simulink model shown in figure 75. In the simulation, the data first goes through some data correction (phase, symbol offset, amplitude), then a QAM demodulator and can then be compared to the data sent (saved beforehand) to obtain the bit error rate.

In figure 76, graphical representations of the received dataset and data processing steps are plotted. Plot a) is the raw IQ data received from the VSA, plot b), the points are still very scattered however the phase is corrected, plot c) the QAM structure is retrieved due to the symbols being synchronised (the sample offset from up-sampled signal has been removed).

For easier data processing, only 15 symbols were modulated to confirm the phase correction hence the 16th symbol on the constellation remained empty. In the figure, the EVM captured was around 6 % however over the full simulation, once stabilised, it was ranging between 4 and 13 %. Those results still allowed minimal errors with 16 QAM, however this range was caused by the automatic phase and amplitude adjustments which were good in an initial testing stage, were not stable enough for higher modulation orders. Therefore the interface was later changed to Matlab code with more control over the functions and also included an equaliser with a known training length so that the phase shift was properly corrected. It may be noted that the phase shift on short datasets, less than microseconds, is minimal so a single phase correction would give better results in this experiment.

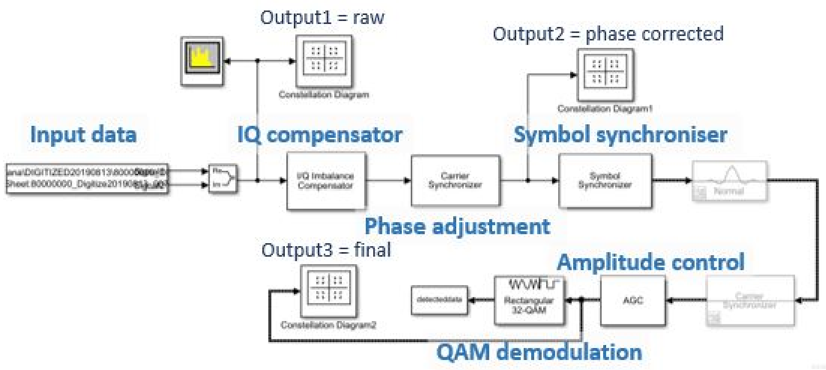

Figure 75: Diagram of the Simulink system for data post processing of VSA datasets (some simulation stages are transparent as they are left unused in the presented transmission results)

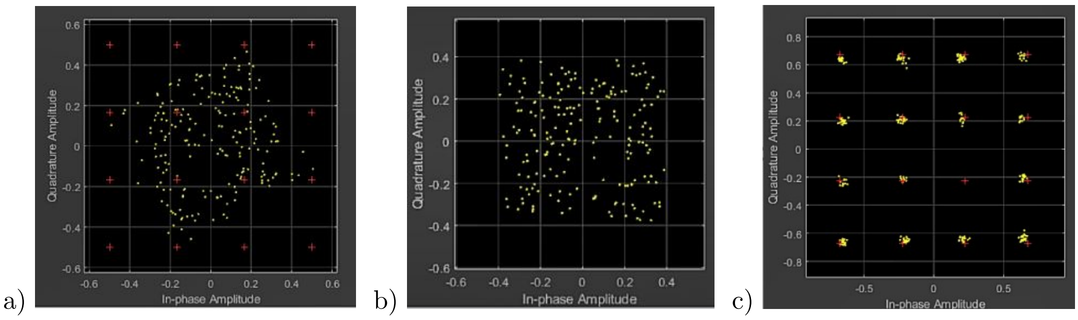

Figure 76: Output constellation diagrams from a test dataset with 16QAM modulation on a 41cm planar surface-wave link, representing a) raw data b) phase corrected data c) amplitude corrected and synchronised data - respectively Output1, 2 and 3 in figure 75

Using the described data processing, a few different modulation orders were tested: 16, 32, 64 and 256 QAM with the same transmit power. All of which had a different bandwidth and therefore data rate, being 160, 250, 180 and 80 Mb/s respectively. They all resulted in approximately the same average EVM = 6-7 % but lower minimum EVMs for the lower order modulation. This led to good data recovery for all of them, except for 256QAM, as an EVM of 6 % is generally too high for such an order and therefore the data correction was too unstable to retrieve the transmitted data.

In figure 77, the effect of the bandwidth on the EVM was measured for a 16 QAM modulated dataset. There is a very slight increase in the EVM with higher transmission bandwidths at both power levels of about 1%, however for the transmission bandwidths considered (10 to 100 MHz) the variation remains minimal. In the considered bandwidth range (and transmission length), the EVM is not limited by the transmission bandwidth.

It is good to note that the EVM numbers displayed are the minimum EVM recorded and that the average EVM of the whole data set generally lies around 2% above the minimum EVM. The minimum EVM was more representative of the transmission as the carrier synchroniser correction was a bit unstable; higher average EVM was due to an imprecise phase adjustment rather than actual data scattering in the constellation.

Figure 78 displays the effect of the VSG input power. The test data set was a 16QAM and 100 MHz bandwidth signal with a transmit power between -40 and 0 dBm. As expected the EVM is decreasing with the increasing transmit power and then stabilises from around -15 dBm at about 6.5 %.

In figure 79, the points on the constellation diagrams are well centred around their expected value however they are more and more scattered as the power decreases, once again the 16th bit has been removed for phase adjustment purposes. From this response, the link appears to be noise limited from the EVM increase but with no sign of distortion.

A new experiment was conducted in figure 80 a) to observe the impact of the carrier frequency on

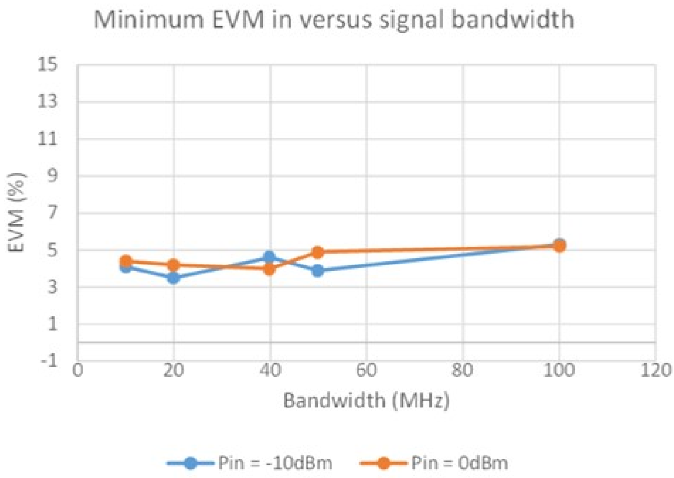

Figure 77: Minimum EVM at different transmitted bandwidth and powers for a 16QAM modulated data over a 41cm planar surface-wave link

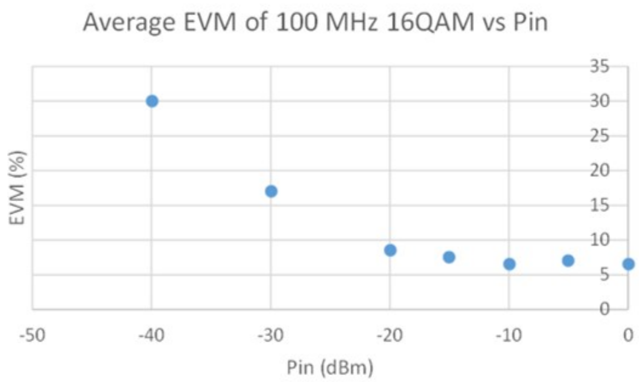

Figure 78: Average EVM at different transmitted powers for a 16QAM modulated data over a 41cm planar surface-wave link

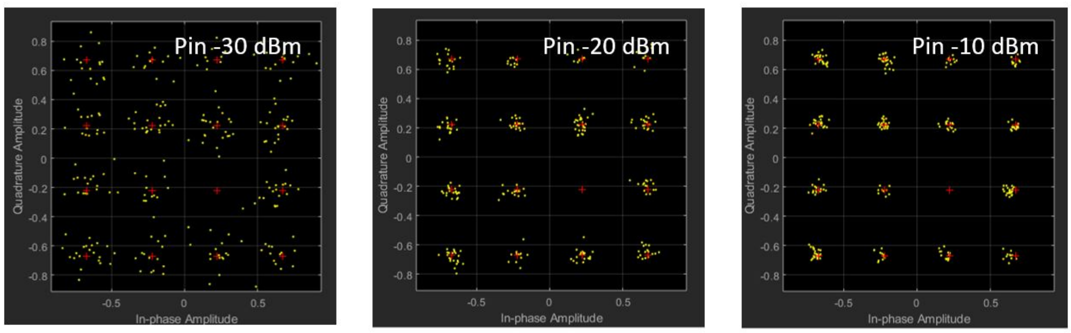

Figure 79: Constellation diagrams of 3 levels of transmit power (Pin) for the 16QAM signal over a planar surface-wave link

the performance of the data transmission, the surface wave link consisted of two planar launchers (same design as previously shown) and a single uncoated copper wire soldered onto the antennas (20 AWG and 150 cm long). The average EVM varies from 7.5 % to 11 %, which for a 16QAM modulation remains in the error free region but the frequencies with high EVM would result in errors for modulations such as 64QAM and beyond. The main purpose was to see how the data transmission would react compared to the link S-parameters (two lengths of the same wire type S-parameters are shown in figure 80 b)). And as expected, the EVM response follows the S-parameter trend, this means most likely the SNR is affecting the data transmission performance and potentially the $(S21 - S11)$ value as well (however the noise frequency response was not characterised for this link).

To note: because the data processing is done through Simulink, the EVM results obtained until this point were higher than recordings with the help of the inbuilt software, for example with the the Rhode & Schwarz VNA (see Appendix).

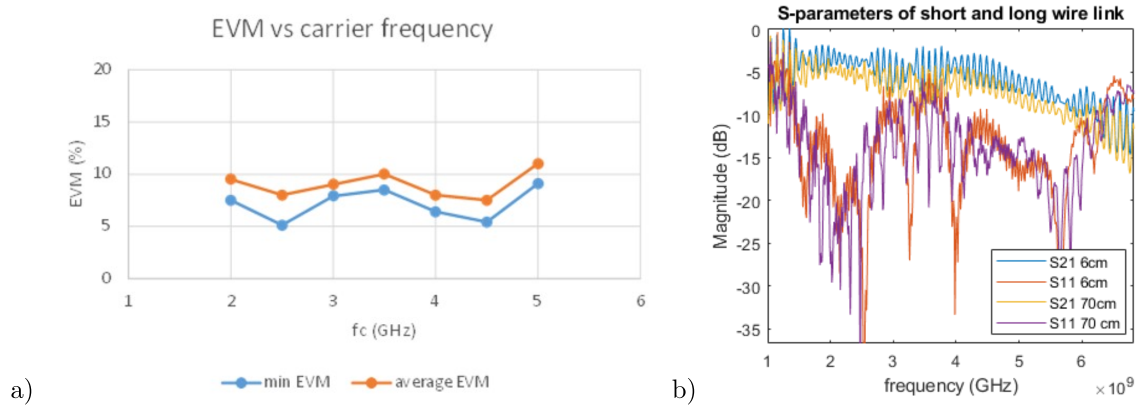

Figure 80: a) EVM performance at a range of carrier frequencies for a surface wave single wire link b) S-parameters of a 20 AWG bare Cu wire of 6 and 70 cm long

The data post-processing being very elementary, the resulting EVMs were higher than might be expected for a good channel. More advanced data processing and equalisation was applied to the system; figure 81 shows the improvement on a test link (using a standard coaxial cable - no SW link) with a new data set. Figure 82 shows the effect of the equaliser on some of the previously recorded datasets from the results shown above at 16QAM and 100 MHz bandwidth. The equaliser type used here is the decision feedback equaliser function from Matlab, as described in the theory section 2.3.4.

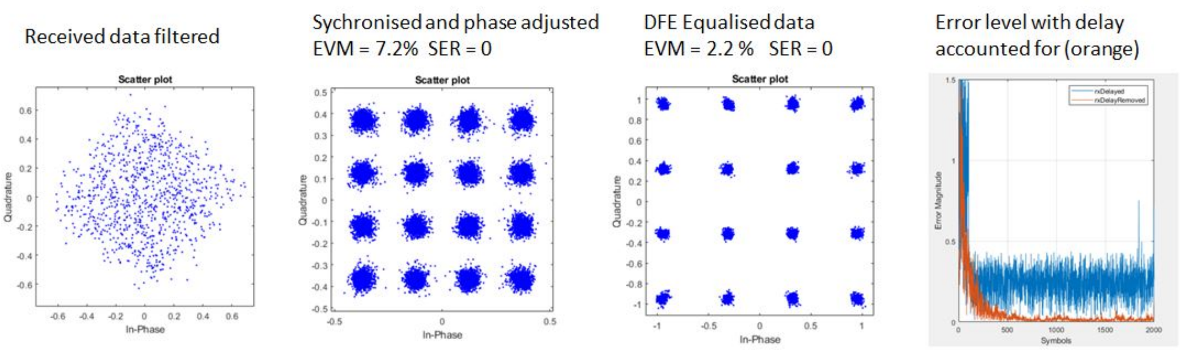

Figure 81: Comparison between simulink and Matlab DFE data-processing results for a commercial 1 m SMA cable transmission link (no surface wave link)

Looking at both figures 81 and 82, the coaxial link's EVM was greatly improved from 7.2 % to 2.2 % which is similar to that obtained using software within the other VSA (Rhode & Schwarz) but in this case, as explained earlier in the theory, a few of the symbols are known which induces a small overhead. In the case of the surface wave data set, an improvement of over 1 % was also obtained; even though the post-processing was adjusted, no new data was generated in the figure 82 experiment. Therefore a newly generated dataset with the equaliser processing has a good potential for improvement. One other

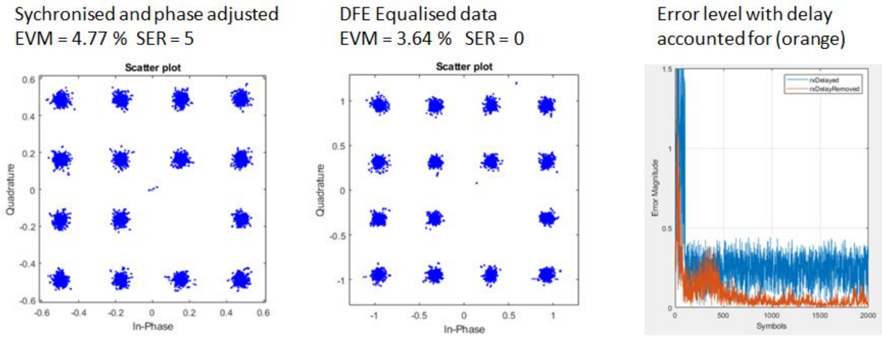

Figure 82: Comparison between simulink and Matlab DFE data-processing results for a wired surface wave transmission link

issue with this setup is still remaining, there is once again a bandwidth limitation both on the generator and analyser side in order to reach the datasets wanted.

A good initial overview of surface wave transmission was gained with several parameters characterised. However, the maximum capacity was limited by the device maximum transmission and detection bandwidth, inducing the need for another setup with better capabilities.

5.1.2 Wideband data transmission

A new setup was designed to overcome the bandwidth limitations from the previous narrowband setup, it consisted of an arbitrary waveform generator and a digital storage oscilloscope. The parameters of the devices used for wideband data transmission are described in tables 4 and 5.

This new setup gave total control over the data generation and processsing, therefore, new code was written for both of the steps. Fully upsampled and upmixed data is loaded onto the generator and the same format is captured by the oscilloscope. A setup similar to figure 57, is used in the following experiments.

Figure 83 represents the full system diagram of the data transmission setup using the AWG and DSO. It clearly shows the Matlab coding part in both data generation and processing on the computer and then the actual lab setup with the surface wave link. The new device parameters are up to 50 GS/s transmission and 20 GS/s detection which is far beyond previous devices and would allow for very high experimental data rates.

Some experiments using the new setup and coding were performed to verify hardware and software parameters in initial experimentation stages and allow the best possible performance in the next and more decisive stages, when pushing for highest data rates.

The first test was of the raised root cosine (RRC) filters used for pulse shaping and up-sampling in Matlab. The main two parameters of the RRC filter are its span and roll-off which directly change the shape of the pulse. A few combinations of span and roll-off were tested using only the Matlab code without any channel simulated to determine the optimum parameters to minimise the EVM. Following this, 4 combinations where selected to test in an experimental data transmission with the planar surface wave link of 41cm. The results are displayed in figure 84. The data sets were transmitted at different power levels as well as AC and DC modes on the Arbitrary Waveform Generator (once again to compare different settings of the setup).

From this figure there are a few trends to point out; firstly, the effect of the voltage level. For both DC and AC transmission, the EVM slightly increases with higher voltage level, but this may be due to having such a short link. Longer links would indeed require higher transmission voltages (and power) in order to compensate for the higher overall attenuation of the line. Secondly the comparison between the different RRC filter parameters, all datasets seem to have similar results with a range of 2-6 % however, one of the combinations results in lower EVM for both AC and DC settings, the data set A (in blue), hence choosing it's filter parameters for the rest of the experiments conducted. Finally, in terms of the

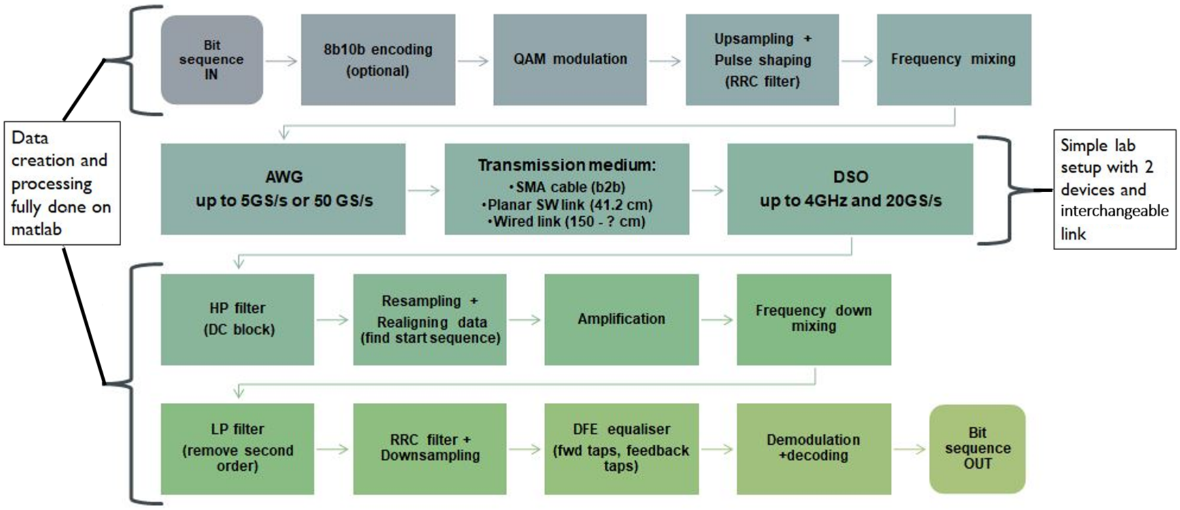

Figure 83: System diagram of the data generation transmission and processing for the AWG and DSO setup

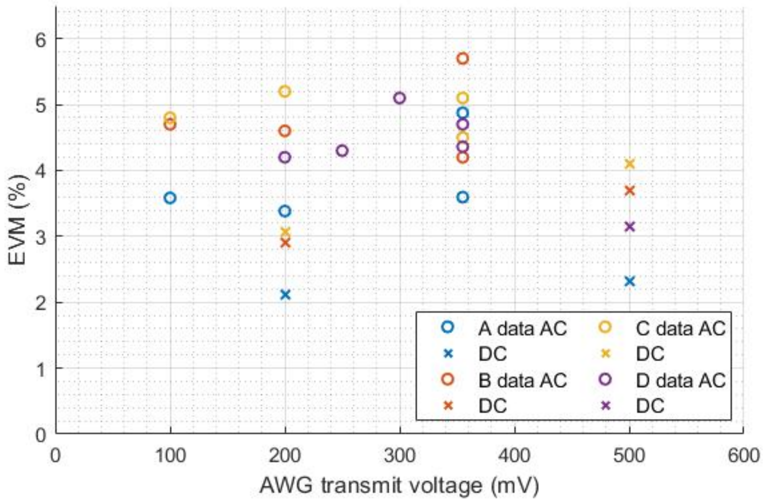

Figure 84: EVM against transmit voltage for 500 MHz QPSK datasets at $f_c = 2$ GHz for 4 combinations of RRC filter span and roll-off such that span$_A = 10$, r-o$_A = 0.22$, span$_B = 10$, r-o$_B = 0.5$, span$_C = 6$, r-o$_C = 0.43$, span$_D = 12$, r-o$_D = 0.34$

voltage setting on the AWG, the DC setting clearly gave much lower EVM results 2 - 4.1 % against 3.3 - 5.6 % for AC.

It is good to note that in the data processing, the training sequence of the equaliser was around 70 symbols and the EVM displayed is the EVM after about 500 symbols, so once the equaliser stabilised and the tap weights adjusted themselves to the optimum value.

Another aspect of interest is the carrier frequency, due to the radiation property of surface waves, it is important to consider which frequency bands of the spectrum it can reliably transmit data on. A first indicator of this is the links s-parameters shown in figure 61 and figure 80 b) (can be extrapolated for other lengths). The planar SW link would suggest a quite stable transmission band from 1.5 to 4 GHz and a decreasing one until just beyond 6 GHz, as for the wired SW link, the main transmission band would be from 1.3 to 3 GHz and another more attenuated band from 3.8 to 6 GHz.

In this experiment, only the flatter and more ideal parts of the link spectrum were tested, so 1.5 - 3 GHz and 1.5 - 2.3 GHz for the planar and wired link respectively. Despite the lower overall loss of the planar link (-3 to -4 dBm) compared to the wired one (-4.5 to -6 dBm), over the same frequency range (1.5 to 2.3 GHz) the wired surface wave link has slightly better EVM performance overall 0.8 % for 16QAM and 0.6 % for 32QAM and 256QAM. Besides that small difference, the performance of both links is very good, below 1 % for lower frequencies and 1.5 % for higher ones, demonstrating a low effect of the carrier frequency on the two media. However, in the results displayed, the transmission bandwidth is only 100 MHz meaning that the data rate remained quite low for all three modulations, being 400 Mb/s, 500 Mb/s and 800 Mb/s for 16, 32 and 256 QAM respectively, this explains the low EVM values but also shows that results remain stable with an increasing data rate.

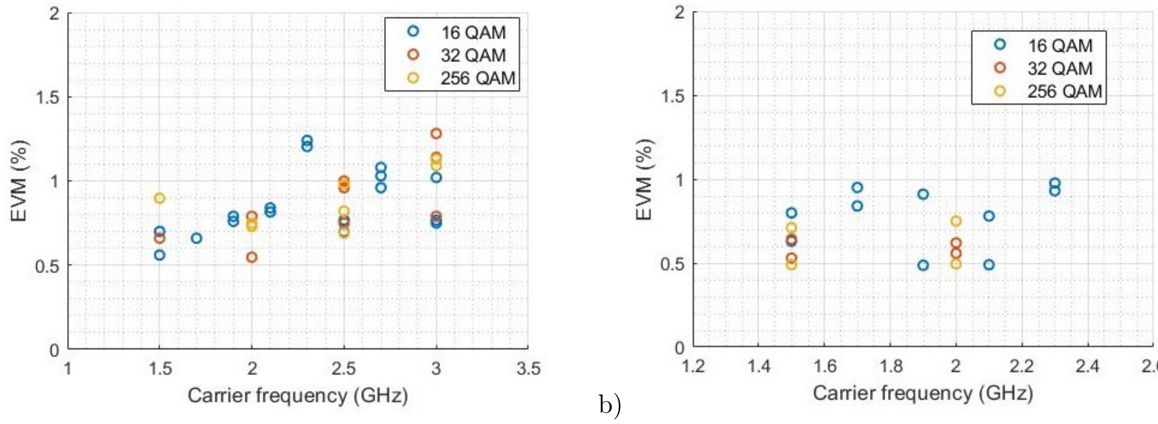

a) b)

Figure 85: Effect of the carrier frequency on the EVM for a) a planar surface wave link (41cm) and b) a wired surface wave link (150 cm) with different modulation orders and 100 MHz transmission bandwidth

The results were obtained using the decision feedback equaliser, with a training length of 70-90 symbols and the EVM stabilised after around 350 symbols. However, the values are already low enough from the 200th symbol, ranging from 0.7 to 2.5 % for the planar link and 0.7 to 1.9 % for the wired one.

In the planar link response, the EVM observes a slight increase with carrier frequency, whereas the wired surface wave link has a very stable response across all frequencies. The difference is not very significant especially considering short lengths of the links meaning most of the loss comes from the SW launcher (which is identical). The main difference may come from the wire attenuation , the planar link transmission media has a higher attenuation especially at higher frequencies according to surface wave theory.

In figure 85, all the transmitted data had a bandwidth of 100 MHz with a varying carrier frequency but also 3 orders of modulation. Therefore, three data rates are represented in the plot, 400, 500 and 800 Mb/s. All of which seem to be performing quite similarly, proving that the data rate limit is far from being reached.

The last main aspect of interest that was tested was the transmitted bandwidth, so far the bandwidth limit was not really reached, hence the potential data rate a surface wave data transmission could reach was yet to be known. In figure 86, the EVM against the transmitted bandwidth is displayed for high order modulations: 256 and 1024 QAM on a 41cm planar surface wave link with a 2.2 GHz carrier frequency. In these plots are displayed data rates from 800 Mb/s to 10 Gb/s, at lower bandwidths, the EVMs seem to be stable around 0.8 % but then from 500 MHz up, the EVMs start to increase, however, the 1024 QAM data points seem to have a better performance than the 256 QAM ones.

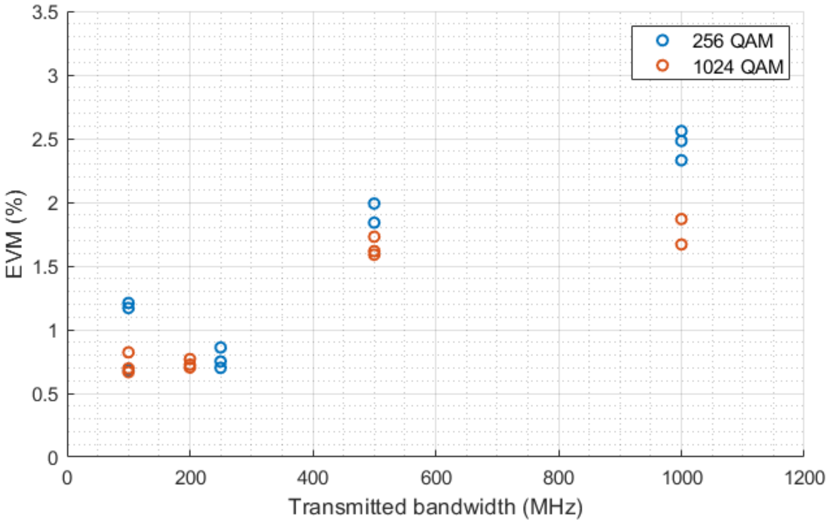

Figure 86: EVM performance against the transmission bandwidth over a planar surface wave link for multiple QAM modulations with $f_c = 2.2$ GHz

Rather than displaying the EVM once the equaliser has reached its best performance, which has slightly varied from one data set to another especially when measuring such wide range of bandwidths (from 100 MHz to 1 GHz of bandwidth). Figure 86 shows the EVM results after 200 symbols (including the training symbols), so that the data is more comparable. The equaliser taps were also adjusted for each test. Although for comparison sake, it was kept as low as possible and adjustments were mostly necessary when increasing the modulation order. For 256QAM datasets, the taps where as follows: forward = 12, feedback = 9, so in total 16 taps. Whereas the 1024QAM data required a slight increase of its taps for the 1000 MHz bandwidth data points, with up to forward = 19, feedback = 14, so up to 33 taps in total. As explained in section 2.3.5, the maximum EVM acceptable decreases with increasing modulation order as there is less and less space for error on the constellation. Therefore an errorless 256QAM data transmission will accept a higher EVM than a 1024QAM one, which is why the numbers are lower for the 1024QAM on the graph as it was requiring more complex equalisation (with more taps).

Even though the difference is noticeable through the numbers only, about 2 % against 1.35 %, it is a useful representation to look at the constellations and eye diagrams. With a higher number of taps the eyes are clearly more open even with as high an order as 256QAM and on the constellation, the data is concentrated around the ideal value (red crosses figure 87) such that there seems to be less data points displayed. When using less taps the points remain within the square space of their their symbol but some symbol points distribution seems to be a bit off center or more scattered around the ideal red cross.

When looking at similar figures and plots for a higher order such as 1024QAM, the error margin-between adjacent symbols is even more restricted, so an EVM below 2.5 % is required. As for the constellation plot, even though very close to ideal, it would show that a low number of data points are approaching the limited area of a neighbouring symbol due to even more precise phase and amplitude correction required for such data rates. Therefore the differences between an ideal and errorless data transmission and one with a less acceptable BER, are becoming difficult to spot.

5.1.3 Equaliser design for longer links

In the previous part, the work done on wideband data transmission and equalisation was explained. A few aspects still required further investigation such as the surface wave link length and media and the limitation from the equaliser taps.

Firstly, the data transmission was tested over a different link, a single bare copper wire of two different lengths 1.51 and 4.95 metres in between the same planar launchers as within the planar links.

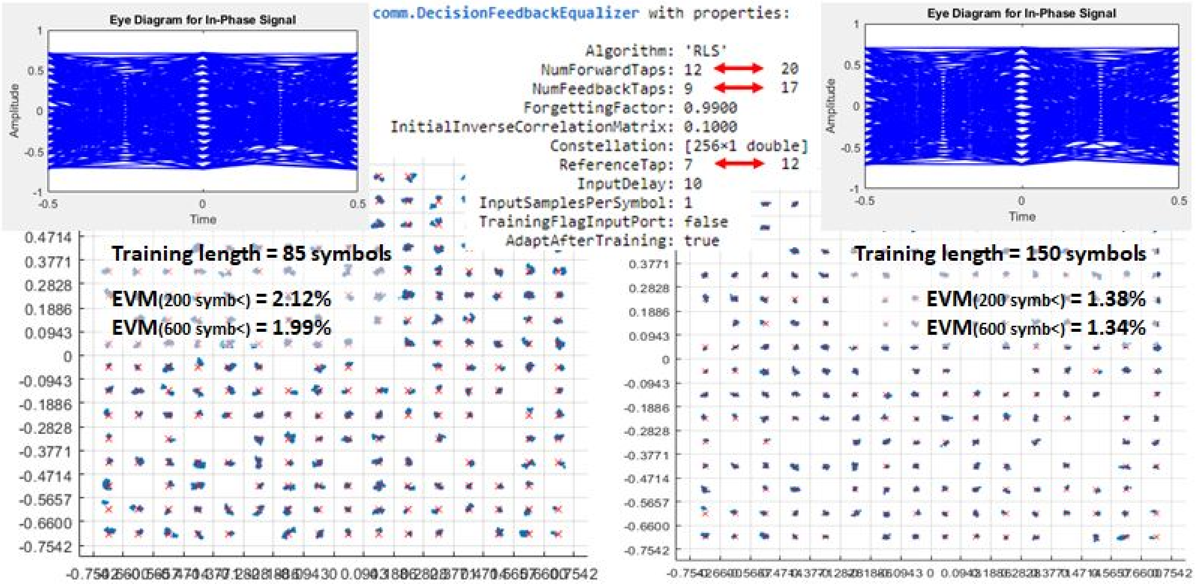

Figure 87: Comparison of different equaliser taps and training length on the same 256QAM dataset displaying the eye digram and constellation end EVM results for a total of 21 taps on the left side and 37 taps on the right side

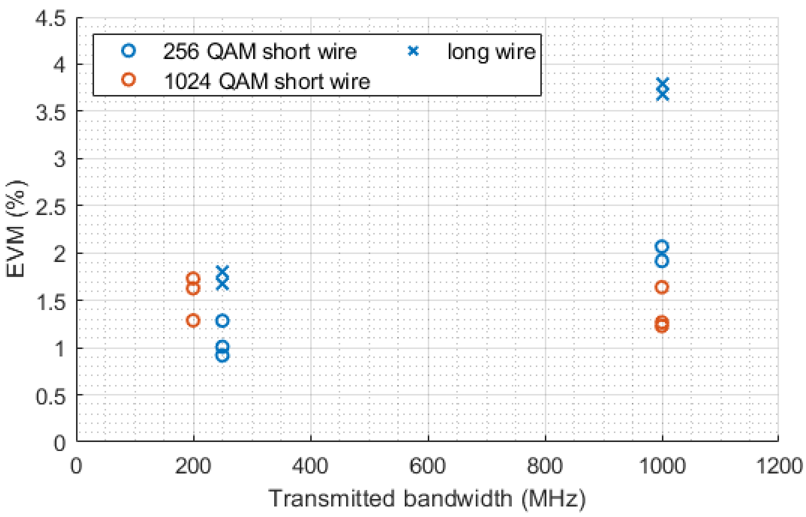

Figure 88: EVM performance against different bandwidths over two single copper wire lengths for 256QAM and 1024QAM with $f_c = 2.2$ GHz with short = 1.51 m and long = 4.95 m

In figure 88, the EVM against bandwidth is shown for two lengths of wire using both 256 and 1024 QAM modulation. Firstly for the higher order modulation, 1024QAM, lower bandwidths achieve comparable EVMs than 256QAM. However at higher bandwidths, the 1024QAM modulation reaches lower EVM than 256QAM although it required more taps, 36 total taps against 23. Then regarding the link length, measurements were only displayed for 256QAM as 1024QAM datasets required too many taps and were too unstable in the equaliser parameters for minimal errors in the data transmission. The longer wire data, displayed by blue crosses, resulted in a slightly higher EVM for 250 MHz bandwidth with 24 total taps instead of 11; and a much higher EVM for the 1000 MHz bandwidth. The EVM was approximately 2.5 % higher, with 36 total equaliser taps instead of 23 for the shorter wire.

It can therefore be concluded that the wire length and subsequently its attenuation are strongly affecting its performance for data transmission. It was not precisely determined whether it was the large bandwidth making the overall transmission spectrum less flat and stable for a single wideband QAM or if potentially longer lengths incurred higher phase delays which would result in intersymbol interference (ISI). However what can be mentioned is that some specific equaliser parameters could give acceptable results but these parameters were not stable from one data recording of the same data set to the other. And the computing powers required to find such specific parameters was also quite intensive and long (timewise) for the PC used, meaning even more intensive requirements for a longer, widespread and real-time setup.

As the equalisation became rather intensive and sometimes unstable/unreliable, further experimentation on the equalisation process was carried out. The current setup consisted of a single training sequence and then a decision feedback equaliser which would adapt after training but without any more known symbols (simply relying on knowing the modulation format and such). Therefore the equalisation was modified a little, firstly by comparing the same dataset with two different tap combinations, one with the minimum number of taps for error-free transmission and one choosing the taps such that the EVM is minimised (whilst keeping the total taps to a reasonable number).

Another experiment was to compare the basic equalisation to a packeted equalisation, as the current data sets are being taken over a short time period (1 to 10 μs) the single equalisation is still enough for the whole dataset, however, over a longer period of time the data would most likely shift away from the initial recording (either phase shifting or amplitude variations). The packet equalisation consists of dividing the dataset in packets, each packet starts with a known sequence of x points. On the processing side, the equaliser training length is constant ($= x$) and the sequence is equalised at each packet start. Therefore, longer data sets would still be resilient to phase, amplitude or other channel changes over time. The decision feedback equaliser function is the same as in the single equalisation process, only the equaliser training "moments" changes. The described equalisation process will be called packet or packetised equalisation, and in comparison, the processing with a single equalisation per data set will be called single equalisation.

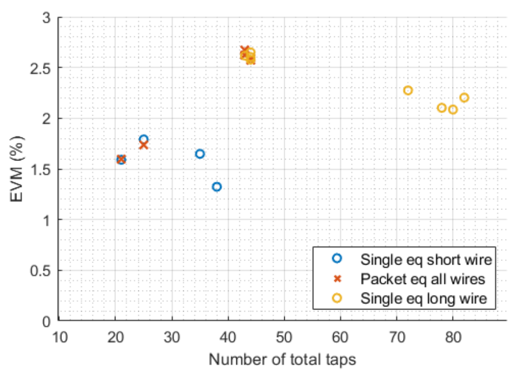

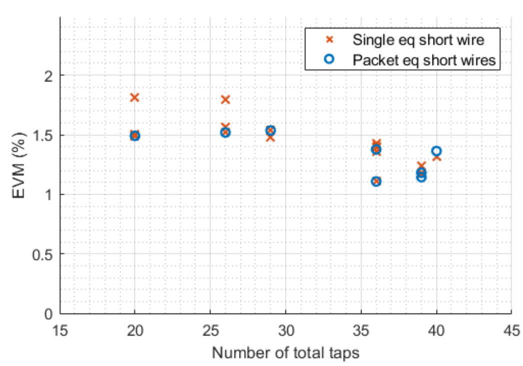

Figure 89: EVM performance against total number of equaliser taps used for single and packetised equalisation with a) 256QAM modulated (8 Gb/s) and b) 1024QAM modulated (10 Gb/s) data transmission over single copper wires

Figure 89 represents the different equalisation processes displaying the EVM against the number of total taps used for the equalisers. In both plot a) and b), the data sets are split into two parts: the exact same data sets are firstly evaluated with a lower number of taps for both single and packeted equalisation and then for a higher number of taps for single equalisation only for a) with 256QAM and both single and packed equalisation for b) with 1024QAM data.

A few conclusions can be drawn from these plots, the crosses representing packeted datasets result in either the same EVM performance or just a little higher than its single equalisation counterpart. This result may be because the channel is static, however due to memory limits, longer datasets were not tested and therefore the packetised equalisation could not outperform the single one in its expected use case scenario (long runs of data transmission).

Another comparison would be from lower to higher total equaliser taps used, either the left blue circles versus right side ones or the left yellow circles against the right side ones. In the plot displaying only 256QAM, shorter wire data transmission EVM decreased by about 0.2 % for an average of 12 taps increase, and the longer wire data transmission EVM decreased by around 0.4 % for an average increase of 25 taps. In the 1024QAM modulated data, an average of 13 more taps brought an improvement of about 0.35 % for a shorter wired link. Quantising such results to actual setup requirements would involve taking into account costs, computational power available and system reliability when using lower or higher number of taps in terms of BER. In the current project scenario, as explained for the previous plot, the total tap requirements for longer wire lengths is approaching high computational cost in order to find the correct number and repartition of taps. Therefore, at lengths of up to 100 m compared to 5 m such equalisers may be limiting for a solution aiming to be low cost and quick installation.

The detailed outputs of the packetised equalisation are displayed in figures 90 and 91. Packets are defined as sections of data sets with the one part known being the training length and the rest being the actual data. Packet equalisation incurs some overhead, however the overhead may be reduced with higher data to training length ratio and over in the case of time varying channel, it can improve the performance of the data transmission. In this example 256QAM modulated data with 1000 MHz bandwidth (8 Gb/s) and carrier frequency of 2.2 GHz is measured over a short copper wire and processed with a packet type equalisation. The equalisation is still using decision feedback equaliser with 10 forward taps and 11 feedback taps. The training length chosen was 39 symbols and full packet length 400 symbols (including the training symbols). The resulting error magnitude is shown in figure 90, a new peak appears every 400 symbols and the peaks lasting less than 50 symbols (data and training length respectively). In the data shown, the total number of packets equalised was 7.

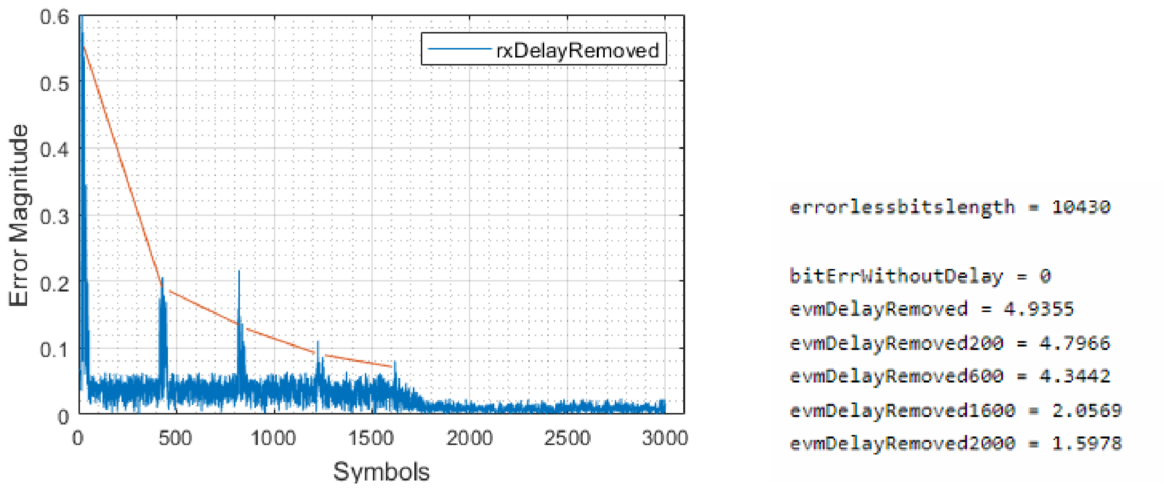

Figure 90: Packetised equalisation a) calculated error between the known and equalised data (outside of the training length, the known data is assumed resulting in inaccurate error magnitude) the red lines show an estimate of the actual error magnitude and b)resulting EVM after set number of symbols, BER and bit size of error-free (equalised) data

The error magnitude plot in figure 90, represents either an accurate error between known data and processed data during the training length (where the transmitted bits are known) or an estimated and inaccurate error (estimated from the modulation format). As the equalisation is progressing (longer training) the accurate error is decreasing with close to exponential decay as is indicated by the red lines of the plot. This pattern is similar to what was shown earlier in figure 81. After a few packets and equalisations, there is a steep decrease (around 1700 symbols) after which all symbol error is low. The sequence has then properly been equalised. In this case the parameters were such that this stage took a few packets to be reached whereas a different equalistation structure with an long initial training length (and recurring shorter ones with low overhead) may be more efficient.

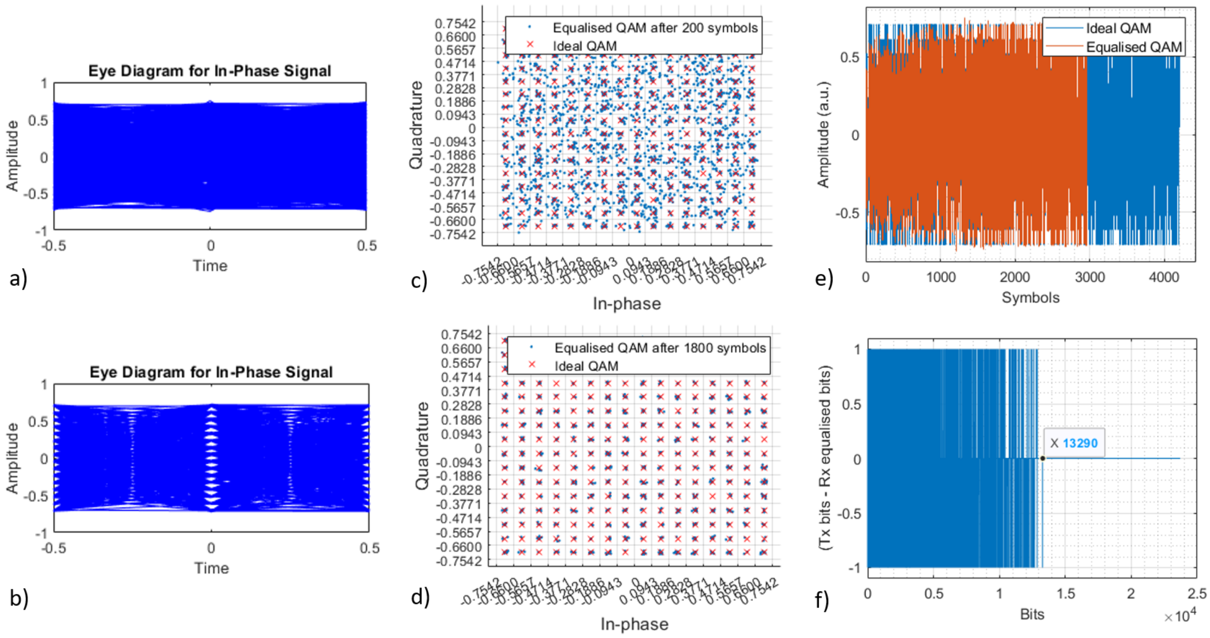

Figure 91: Packet equalisation results after 200 symbols (top) and 1800 symbols (bottom) with a) and b) the eye diagram, c) and d) the constellation diagram, e) the amplitude of the real QAM symbols for the transmitted and equalised data over time (in symbols) and f) bit errors (error if = 1 or -1) over time (in bits)

Figure 91 details the evolution of some characteristic plots such as the eye diagram and constellation before a) and c) and after the tap weights reach equilibrium b and d). After 200 symbols, one training sequence has already allowed to adjust the amplitude of the symbols as can be seen in c) and e). Looking at the plots b) and e) it is clear that there is now no error in the transmission as the eyes are open and equalised symbols very close to the ideal symbol location (red crosses) in the constellation; as for plot e) the equalised QAM symbols now overlap with the transmitted sequence (blue) and seems to match very closely. In plot f), the bit error is represented by plotting transmitted bit value (0 or 1) minus received corrected demodulated bit value hence the value varying from -1 to 1, the marker shows that no errors have been detected from the 13290th bit so the 1661th symbol whivh seems to correspond to just after the 5th training sequence in figure 90.

In order to get the best possible results, a recursive program was created to calculate the EVM and BER for each forward and feedback tap combinations. Some of the previous results were obtained and optimised using this code. An example of the results from the code is displayed in figures 92 and 93, were the data set chosen was a 1 GHz bandwidth 256 QAM data transmission with a carrier frequency of 2.2 GHz over a 4.95m single copper wire, the data processing was done using a training length of 150 symbols and the transmitted data rate is in those figures 8 Gb/s.

The scale on the right of the plots shows the values of EVM and BER varying with colour. In the EVM plot the darkest blue corresponds to the minimum EVM value from the data set with all taps combinations, and the highest value was truncated to 6 % so any yellow point has a value of 6 % or over (going all the way up to 70 % in this case). The settings were chosen in order to show a variation of taps. In the case of the BER plot the scale is logarithmic (more common for BER). The darkest blue points correspond to a BER of 0; due to the number of bits received, the BER corresponding to a single error is 3.39×10^{-5} so slightly above the minimum value's colour in the scale.

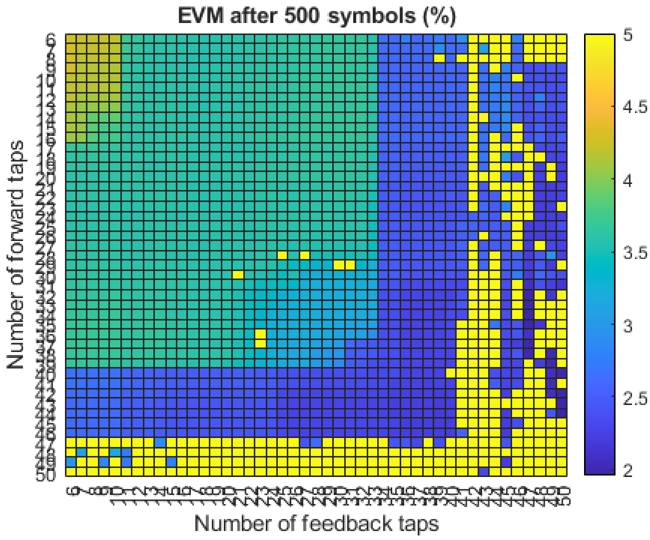

Figure 92: Heat map representing the EVM value depending on the number of taps chosen for the equaliser's forward and feedback taps - 256 QAM modulation over a 4.95m single wire link with 1GHz transmitted bandwidth (8 Gb/s)

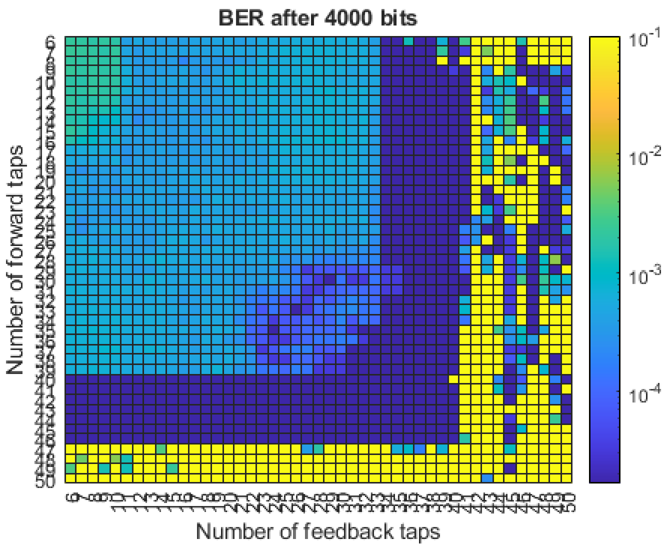

Figure 93: Heat map representing the BER value depending on the number of taps chosen for the equaliser's forward and feedback taps $BER_{min} = 0$ - 256 QAM modulation over a 4.95m single wire link with 1GHz transmitted bandwidth (8 Gb/s)

There are two areas were the EVM reaches low values, the main one is in a corner shape with one tap number rather high, 33-40 taps, and the other ranging from 6 to 40 taps, in this area the values are around 2.4 %. The points with best EVM require both tap numbers to be high, especially the number of feedback taps, but those data points are scattered within a very poor performance tap combination area, so are unlikely to be useful in practice. In the BER calculations, once again the inverted L shape error free area is present, however some data points whose EVM's values were too close to distinguish their performance are now clearly data with error-free transmission or with high error rate. The preceding results suggest that the total number of taps could be the determining quality factor in such equalisation, another possible explanation is that the performance of the equaliser function used may degrade after a too high number of taps.

Another aspect of interest for the reasearch aim is the link length. A comparison between the wire lengths for the tap requirements, stability and overall results was carried in figure 94 for a dataset of 10 Gb/s and wires of 1.51 and 4.95 m.

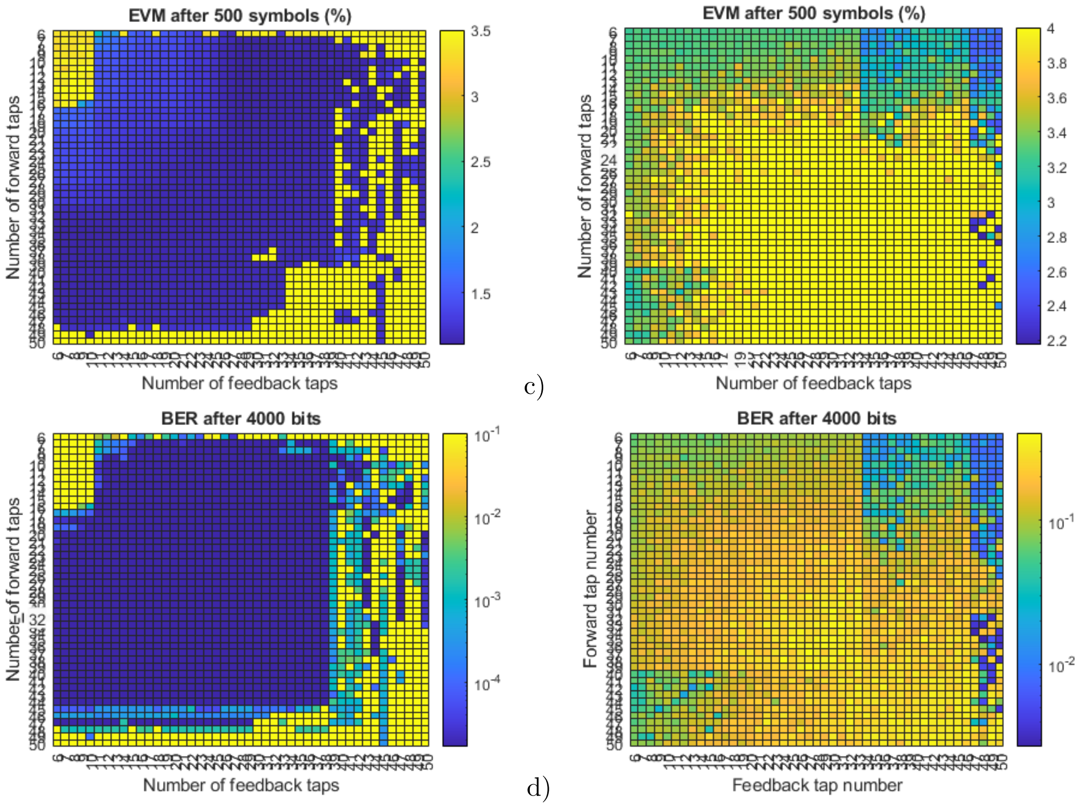

a) b) c) d)

Figure 94: 1024QAM with 1 GHz transmitted bandwidth 50x50 taps combination performance calculation using EVM and BER for short (left) and long (right) single copper wire

In figure 94, a) and c) represent the EVM and BER of different tap combinations for the 1.50 m wire link and b) and c) the ones for the 4.95 m wire link. In the shorter wire link, the lowest EVM is 1.1 % and the lowest EVM area is a combination of approximately 25-42 for the one tap and 7-35 for the other tap. In the BER representation the minimum value (darkest blue) is BER = 0 and that errorless area is approximately the same but other BER value are very distinguishable from the minimum points. In comparison, the longer wire results have slightly different scale and no points have a BER of 0,, the minimum bit error rate being 0.025 and 2.17 % for the EVM. From looking at both b) and d), most of the tap combinations have an EVM of above 4 %, which is very high for 1024 QAM and the best data points are around forward taps = 36-45 and feedback taps = 47-50, however once again they are scattered, unpredictable and not good enough for the current data transmission standards, especially for such transmission lengths.

The decision feedback equaliser has improved the performance of the surface wave data transmission processing greatly. Through the preceding experiments, a certain limit of the equaliser has been reached particularly for longer link lengths. As a single equalisation is used over the full transmitted bandwidth, wider bandwidths as well as longer link lengths, that both add irregularities the the channel response and increase the complexity of the equaliser. One of the main issues encountered was finding high performing tap combinations (highly time consuming even with some automation) as well as such tap combinations were not consistent from one measurement to another (even with the same input dataset). In theory, decision feedback equaliser is defined as a medium complexity equaliser, other equalisers may offer higher performance for wideband QAM transmission.

5.1.4 QAM transmission data rate and link structure summary

The previous section showed that the length of the wire has a strong effect on the transmission quality. However, it is also of interest to compare the different transmission media. This is especially of interest as the transmission wire set within the project, BT's drop wire DW11, has a more complex structure that a bare copper wire or a planar copper track.

In this section, a few of the results presented in the previous subsections will be reused but plotted against the data rate and using optimised numbers of equaliser taps, training length and carrier frequency.

The planar link results are displayed in figure 95, where most of the different parameters have been tested. As a perfectly straight and aligned with the antenna, shorter length (41 cm) and with a low ϵ_r dielectric "coating" so a more confined wave; this planar link is representative of a more ideal transmission medium which can act as a reference for comparison.

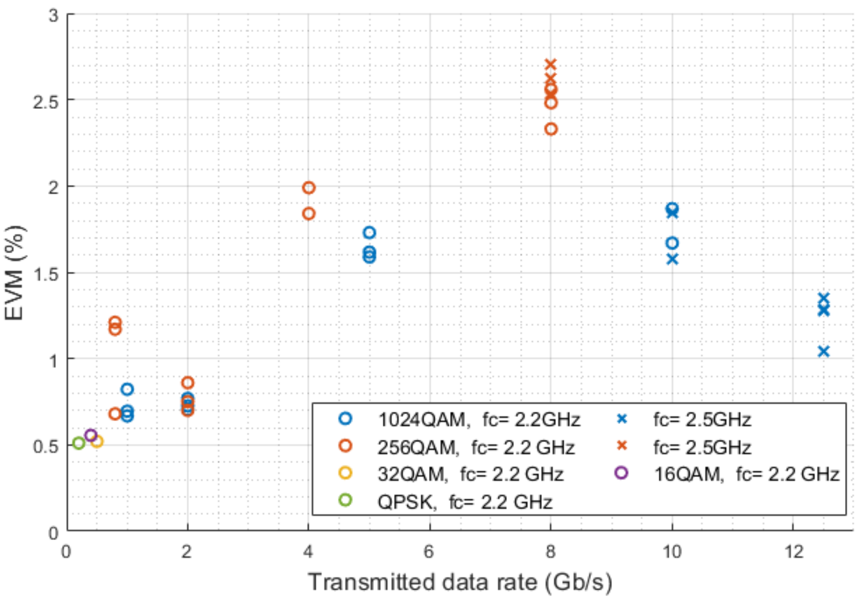

Figure 95: EVM against data rate for various modulation orders (colour) and carrier frequencies (shape) for SW data transmission over a 41 cm planar link

In this figure, a wide range of data rates is represented, from 0.2 to 12.5 Gb/s therefore a bandwidth of 200 to 1250 MHz with modulations between QPSK and 1024QAM. A lot of this data has been described in more depth earlier in the thesis, however, briefly, up to 5 Gb/s the data processing was kept quite basic and especially in terms of equalisation. From 8 Gb/s the equalisation has received a bit more attention and was adapted to keep a bit error rate of 0, this was especially the case for the 1024QAM at 12.5 Gb/s were the total number of taps was set to 36. As for the lower data rates area, the different modulation format performance can be compared, and their EVM results are generally quite similar up to 2 Gb/s (around 0.7 %) with slightly higher results for higher modulation orders.

The single copper wire link results were plotted against the transmitted data rate, with the interest of comparing the results from a 1.5 m wire and a 4.95 m wire, in figure 96 and 97 respectively. Such comparison allows rough projection to more practical lengths of over 50 m.

Similar to the planar link, the EVM results were obtained with a basic data processing for lower data rates and more advanced equalisers for the higher ones. For the values, looking at figure 96, the data rates below 1 Gb/s are on average similar to those for the planar link but low modulation orders are about 0.2 % higher. The 2 Gb/s measurements are now higher, especially for 1024 QAM by around 1 %. And finally the higher data rates are more spread out (different tap combinations) but averaging to slightly lower values (approx. 0.7%) except for the 12.5 Gb/s point that possibly started showing a bandwidth limit (see s-parameters). This former result may be explained by the fact that the planar link can be represented by the Goubau line theory and the dielectric coating would increase the attenuation of the line per unit distance, as well as the fact that more care was taken for the equalisation of theses data points in the wired links.

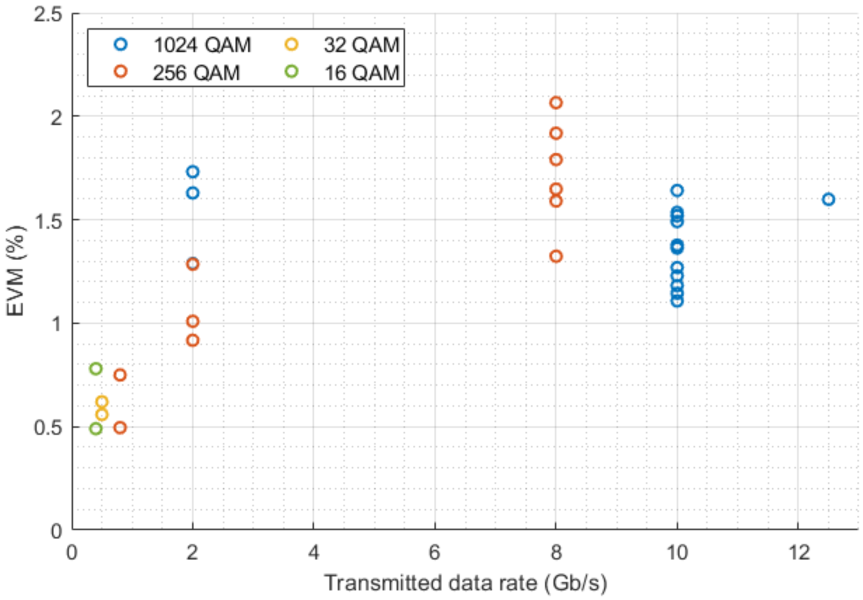

Figure 96: EVM against data rate for various modulation orders for SW data transmission over a 150 cm single copper link

Overall, the plot trend is quite similar to its planar equivalent with values increasing from lower to mid data rates and then decreasing at highest data rates as the equaliser requirements for errorless data transmission increased. As before, the 1024 QAM transmission resulted in lower EVMs than the 256 QAM data once again to meet the no error condition.

Results generally being worse with the longer wires, fewer measurements were taken for that setup. Hence, some of the data points displayed in figure 97 have a BER much higher than what would be acceptable for reliable data transmission (0.002 and 0.004).

Comparing figure 97 to figure 96, the 2 Gb/s points are about 0.5 % higher for the longer wire and the higher data rate ones are on average 1.2 % higher than its shorter wire equivalent. Compared to the current wire length objectives this large difference from 1.5 to about 5 m length is quite significant and especially when looking at the higher transmission bandwidths.

This shows that for longer links and reasonable equalisers, the channel becomes a limiting factor. Other modulation methods such as OFDM should therefore be considered to improve the performance.

As part of the industrial collaboration project, BT's DW11 cable was of particular interest as a SW transmission medium. Figure 98 displays the detailed results of wideband data transmission over a 5.5 m DW11 wire for a 16 QAM and a 256 QAM with 100 MHz transmission bandwidth (resulting in 400 and 800 Mb/s respectively) at 1.9 Ghz carrier frequency. Those initial results confirm the good performance of the DW11 cable. Compared to both planar and wired links at those data rates (and much shorter lengths), the EVMs obtained were within the same range if not better for the 256 QAM data

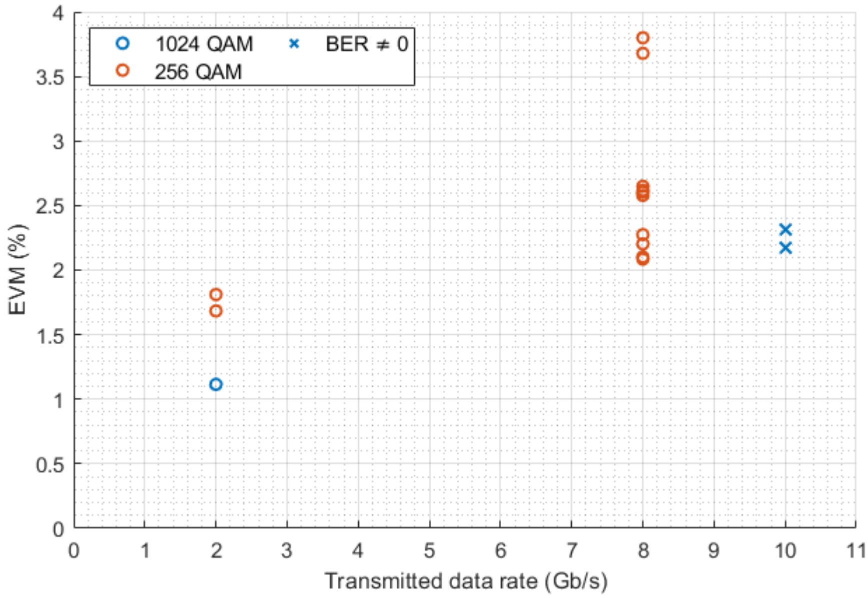

Figure 97: EVM against data rate for various modulation orders for SW data transmission over a 495 cm single copper link

transmission.

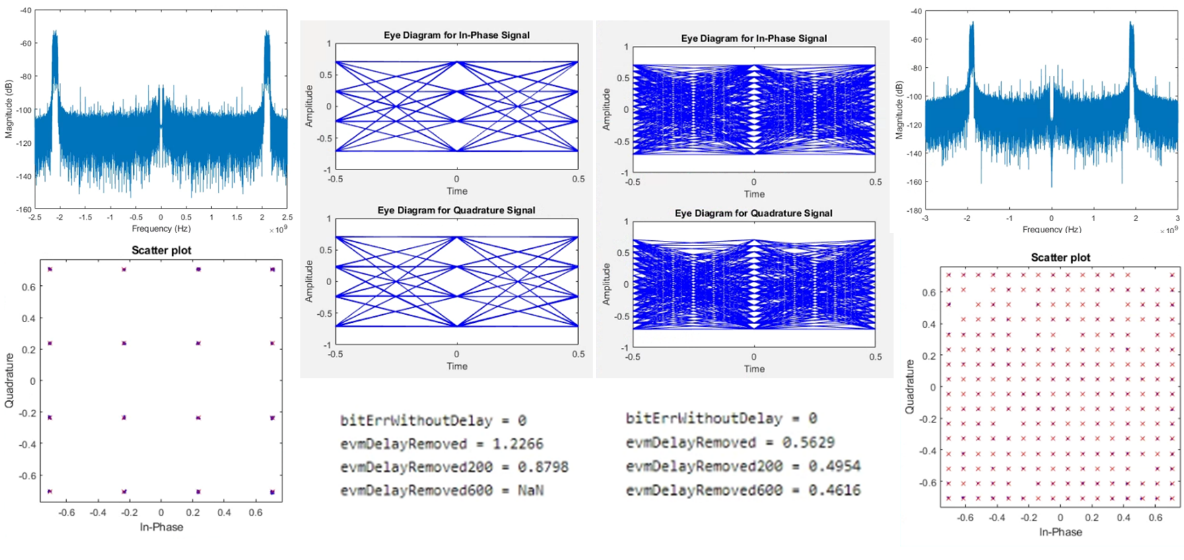

Figure 98: Wideband QAM transmission results over a DW11 cable with the received spectrum, equalised constellation and eye diagram and EVM results for two data transmission (left) a 16 QAM and (right) a 256 QAM 100 MHz bandwidth with $f_c = 1.9$ GHz

As a conclusion for the wideband QAM data transmission, most aspects of the data generation, processing and the actual setup were analysed and displayed in this section. Some high data data rates have been achieved over shorter surface wave links, 12.5 Gb/s over 1.5 m and up to 8 Gb/s over about 5 m.

Some drawbacks were discovered from transmitting very wide bandwidth data transmissions together with a decision equalisation. Such processing proved limited when the channel response became more complicated with increasing link lengths.

A thorough comparison of the data rates over different media types and lengths confirmed that wideband QAM was greatly affected by the longer wire length which was mostly due to attenuation becoming too irregular over the full bandwidth to be corrected by the current equaliser.

Such results point toward using a more advanced modulation formats, OFDM modulation, dividing the band into subchannels and therefore requiring much simpler equalisation over similar total bandwidths.

Initial experiments on the widely deployed DW11 proved it is a good candidate for surface wave data transmission as it performed similarly to a more ideal short planar link over narrow transmission bandwidths.

5.2 OFDM data transmission

5.2.1 Basic transmission

OFDM data generation and processing code was written in Matlab for the OFDM over surface wave experiments. The process is summarised in the block diagram of figure 22. Figure 99 shows various views of the coding and generation steps in order from a) to f).

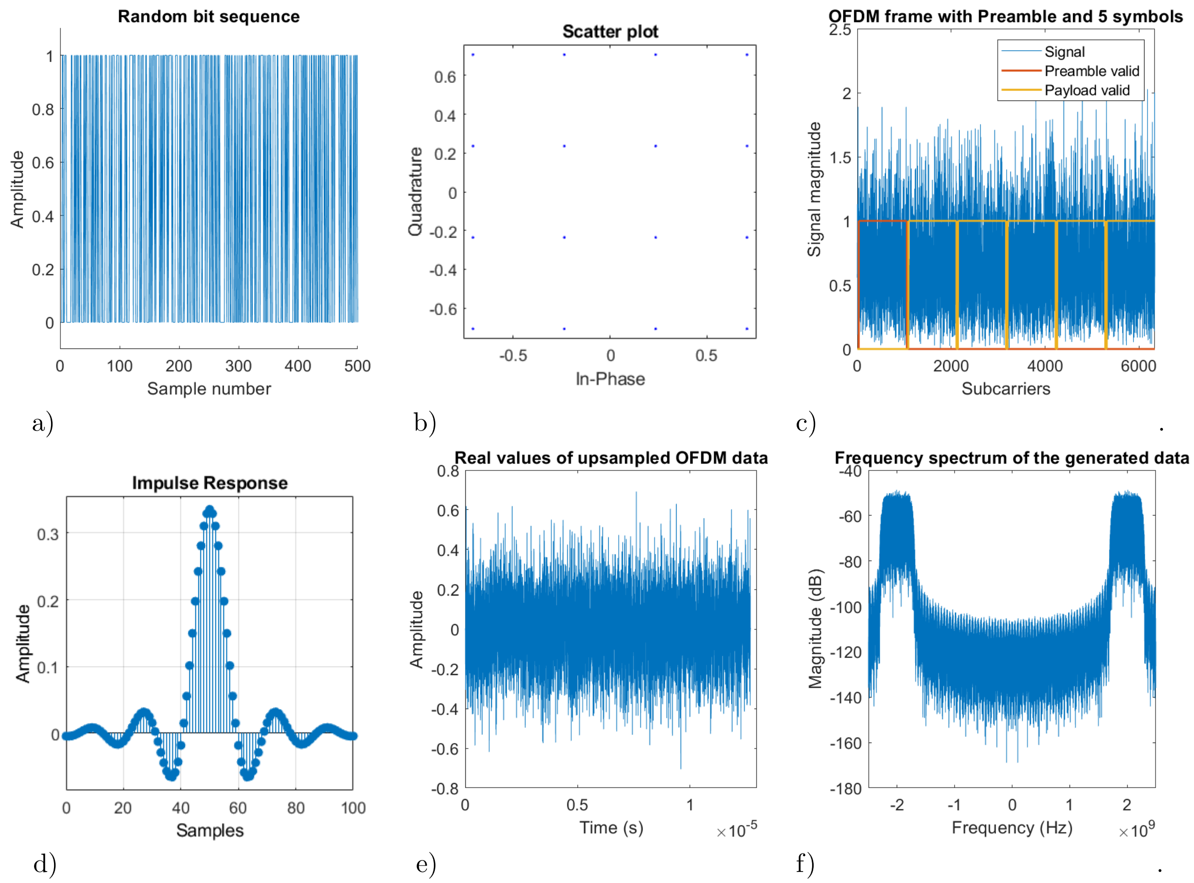

Figure 99: Data generation process plots with a) part of the random bit sequence, b) the modulated bit sequence using 16 QAM, c) The OFDM modulated frame with the preamble and data symbols, d) the impulse response of the upsampling square root filter e) the real values of the upsampled data set and f) the double-sided spectrum of the frequency mixed data which will then be inputted to the AWG

The modulation parameters of the example used to explain data generation and processing is a 16 QAM, 500 MHz with a 2.1 GHz carrier frequency. As shown in figure 99, from a) to f), the data bits are first generated randomly (including the preamble bits). The bit sequence is then modulated by a 16 QAM Gray coded modulator. The resulting signal is passed to the OFDM modulator, consisting of 1024 subcarriers, a cyclic prefix length of 32 and 5 symbols per frame. The OFDM modulated preamble symbol is added to the data symbols (also called payload in the figure). The signal is upsampled as well as shaped using a square root shape filter with a span of 10 symbols and a roll-off factor of 0.22. In order to reach the wanted carrier frequency, the number of samples per symbol is 10, following equation (36). The upsampled signal is numerically mixed with the carrier frequency, and the resulting spectrum is shown in plot f); the generated samples can then be passed to the AWG with a clock or sample frequency of 5 gigasamples per second, to experimentally generate the modulated signal at the expected data rate.

Once the data is loaded onto the AWG and transmitted through the surface wave link, it is captured by the oscilloscope as a time series and processed as explained in figure 22 b) and in the plots figure 100 a) to f) in order.

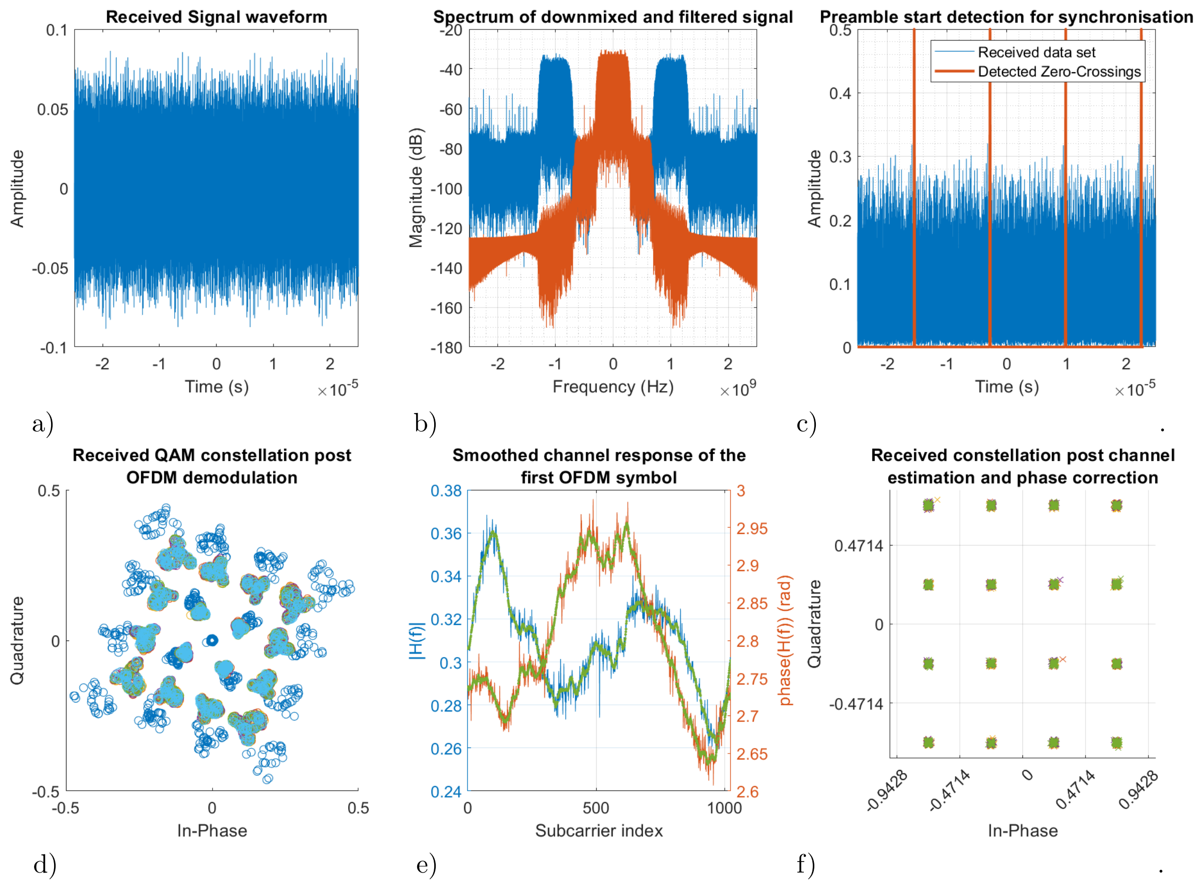

Figure 100: Data processing plots from the test data set with a) the time data captured from the DSO, b) the frequency downmixed spectrum (blue) and low pass filtered (orange), c) the preamble start detection using Schmidl and Cox's method [49], d) the QAM constellation post downsampling and OFDM demodulation, e) the channel estimate calculated from the first symbol and used for equalisation and f) the constellation of the equalised QAM symbols

As shown in figure 100 a), the data is resampled from the capture sample rate to the required sampling rate. A high pass filter is applied to remove any DC or low frequency components. The data is then numerically downmixed and passed through a low pass filter (orange curve in b)). Whilst it is still oversampled, the preamble is detected for the timing synchronisation. In figure c) several preamble starts are detected as orange peaks (due to continuous transmission of the dataset). Once the frame start is identified, the signal is downsampled using the reverse square root shape filter, and the data is passed through the OFDM demodulator. The output constellation is shown in figure d) with the preamble data in dark blue. From the received constellation, the 16 QAM modulation can already be distinguished; however, it has some phase and amplitude impairments due to the channel response, which affect the signal performance. As described in equation (42), the channel response is estimated using the first OFDM symbol of the frame, considering the data to be known to the receiver, and the equaliser taps calculated. In order to have a better channel estimate, the outlier points are removed and some smoothing is applied to the detected channel response. The equalised QAM constellation is displayed in figure f). To analyse the signal quality, the post-processing EVM is calculated, in this case, EVM = 1.46 %; the data is then demodulated, and the BER can be calculated as well as the overhead and post overhead data rate, here BER = 0 and the post overhead data rate is 1.29 Gb/s.

The data set and results presented serve as an example dataset to illustrate the data generation, processing, and output calculations used. The primary purpose of using OFDM modulation was to overcome the wideband transmission restrictions and transmit high data rates on longer DW11 cables. As explained in the experimental setup, the laboratory's dimensions limit the cable length. Therefore, the aim is to maximise the data rate limits of such a link for a low output BER with a single bit level and no FEC coding, for the longest cable which can be physically accommodated without bending (6.1 m).

5.2.2 High throughput datasets (single frame)

Tests were conducted on single frame data sets of various modulation orders and bandwidths to reach data transmissions allowing minimal errors and maximal data rates. Due to the dataset size of around 20 OFDM symbols and 2048 subcarriers being a little limited, the initial goal was to get error-free data transmissions. Furthermore, this solution aimed to compare to the current technologies such as G.fast which transmits 1 Gb/s over 100 m. The experimental setup presented, while having a high data rate capacity, has a few limitations such as the link length, the output power of the AWG and the data generation being single level modulation and non-coded. The relationship between the link length and data rate remaining unknown, a focus on achieving beyond 10 x the data rate for below 1/10 the link length was set as only a linear relationship may be assumed (such a relationship is true for most data systems).

From the experiments, a high throughput data transmission was found and its parameters are described in the table figure 101 a) and the measured transmit power spectrum taken directly from the AWG's output is shown in b). Comparative to the the generated OFDM spectrum (similar to figure 100 f)), the spectrum measured from the AWG has a flat response (pre-channel impairments) and the structure as expected from an OFDM data set.

a)

Property	Value
Carrier frequency (fc)	2.1 GHz
Bandwidth	2083 MHz
Subcarriers (Nc)	2048
Cyclic prefix length	64
OFDM symbols/frame	20
Number of frames	1
Number of Nulls	2 (at 1.6 GHz)
Samples per symbol	6
Transmit power	-10 dBm
Data rate pre-overhead	12.5 Gb/s

b)

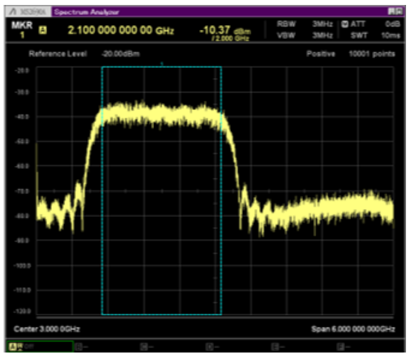

Figure 101: Input parameters of the 12.5 Gb/s 2083 MHz 64 QAM data transmission with a) the parameters table and b) the spectrum of the input signal measured at the output of the AWG showing a power of -10.37 dBm

The signal is transmitted through the 6.1 m SW DW11 link and the data received and then processed is shown in figure 102.

The down mixed and filtered spectrum shows the transmitted bandwidth of the signal and the constellation in b) the downsampled and OFDM demodulated data, unlike the example, the expected 64 QAM constellation is not clearly seen due to the channel effects. Then in c) the detected channel response from OFDM symbol (1 out of 20) is plotted; the magnitude of $H(f)$ decreases and oscillates with increasing frequency and the phase goes up and down whilst also oscillating (unlike the magnitude, the phase trend is not repeatable).

The equalised QAM signal is shown in the constellation figure 102 d), where the square grid shows the symbol limit for the hard-decision QAM demodulator. Most of the points are well centred to their

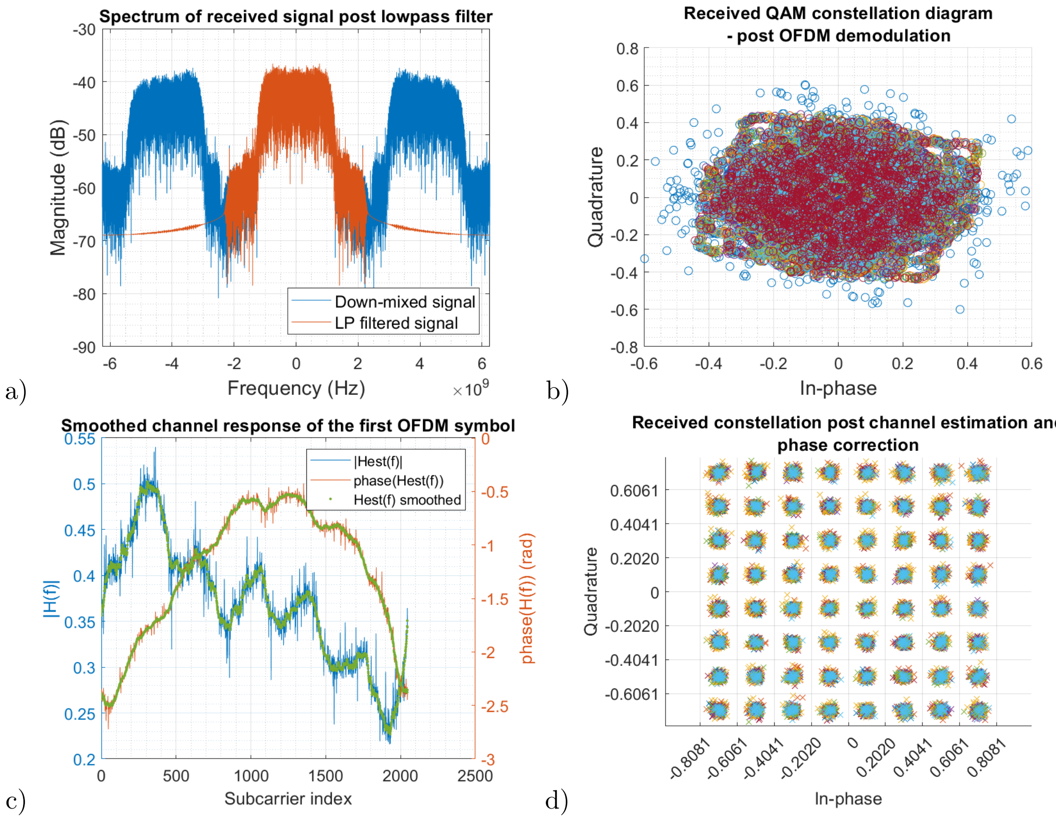

Figure 102: Results of the wideband high throughput 64 QAM dataset with a) the received down-mixed and LP filtered spectrum, b) the OFDM demodulated QAM constellation, c) the calculated channel response and d) the equalised QAM constellation

expected symbol however some symbols are slightly scattered, worsening the resulting EVM and potentially resulting in errors. In this case BER = 0, EVM = 2.98 %, overhead OH = 0.8773 and therefore the post overhead data rate is 10.97 Gb/s (limited by the number of symbols/frame and the number of frame).

A few different data sets were tested with the presented parameters, they generally resulted in a number of errors equal to 0. Occasionally 1-2 odd errors were observed, these to be at subcarriers in the 2.4 GHz ISM band and could be attributed to interference from the Wi-Fi band. The length of the data sets only went up to 40 symbols which is quite limited for a proper BER measurement, follow up experiments presented in section 5.2.3 perform a more rigorous BER evaluation .

Further analysis of the transmission can be don by plotting the EVM against firstly the OFDM symbol (in the order of serial transmission) and secondly the OFDM subcarrier, each subcarrier is the average of the 19 data symbols, which can then be converted to the corresponding transmit frequency.

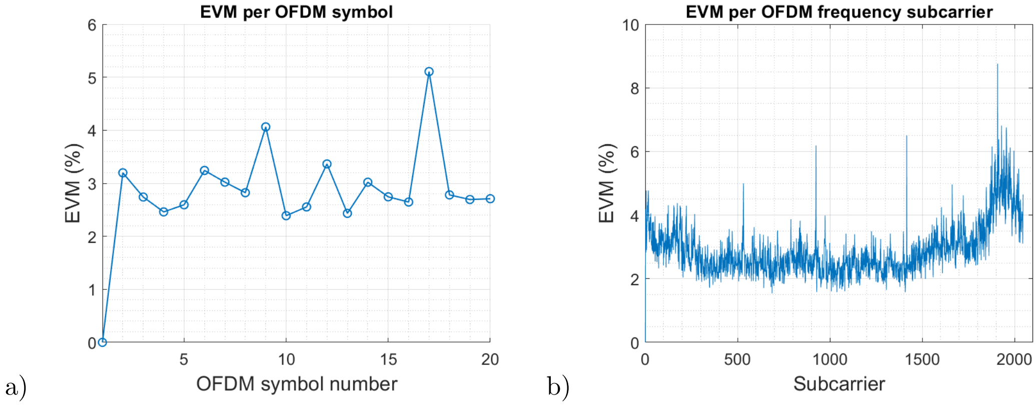

Figure 103: EVM characterisation of the 12.5 Gb/s 64 QAM transmission against a) the OFDM symbol number and b) the OFDM subcarrier

The first plot figure 103 a) shows that the lack of change suggest the channels is stable, therefore through time (even though very short). It is worth noting that symbol number 1 has an EVM of 0 as it is the (known) symbol used for equalisation. The second plot b), however shows a certain difference between the subcarriers, the general trend seems to follow what would be expected when looking at the channel response, meaning a lower channel loss gives lower EVM and vice versa. A few specific subcarriers show a much higher EVM, making them likely to produce errors and likely represent the scattered points observed in the constellation.

By comparison, the capacity estimates in section 4.2.3 for a 6.1 m link, with a -10 dBm power budget, resulted in a data rate of 16 Gb/s for a spectral efficiency of up to 15 bit/s/Hz. This is well above from the maximum transmission. Considering the bit and power loading plots figure 72 with a 6 bit/s/Hz cap, most of the bits were allocated to the 6th order so resulted in a similar total data rate, in the simulation the total power predicted was -7.1 dBm which is slightly above the one measured for the data transmission.

Furthermore, the water-filling model assumes a high coding gain not added to this scenario and a BER limit of maximum 10^{-7}. This shows that the experimental performance matches relatively well in terms of data rate and power usage therefore the water-filling algorithm may be a good tool for data rate predictions of the presented system together with precise characterisation of the link response and noise level.

To achieve high throughput, another data transmission scheme was considered. In this case a higher order modulation: 256 QAM was used with a smaller bandwidth. The carrier frequency was swept to establish is multiple bands could be supported. In this experiment, a 500 MHz bandwidth 256QAM signal was swept though several carrier frequencies, from f_c = 1.4 GHz to f_c = 3 GHz.

The use of multiple bands could allow a shared medium with each user assigned a carrier and therefore reducing the required analogue front end bandwidth compared with a wideband solution. Furthermore the chosen bands can avoid interfering bands in the wireless spectrum as seen through the noise measurements with the 2.4-2.5 GHz peak figure 70 (although may need to consider licence-free ISM band transmission in further developments).

Each carrier frequency dataset was measured separately in the experiments, but with guard band implementation, the three presented bands can be sent as a single data set. The parameters of the datasets and received (and high-pass filtered) spectrums are represented in figure 104 a) and b) respectively. The total pre-overhead data rate is similar to the previous case but due to the higher modulation order, it only requires a total bandwidth of 1.5 GHz rather than over 2 GHz, furthermore there is no transmission over the 2.4 GHz Wi-Fi band.

Property	Value
Carrier frequency (fc)	1.4/2/2.8 GHz
Bandwidth	500 MHz
Subcarriers (Nc)	1024
Cyclic prefix length	32
OFDM symbols/frame	15
Number of frames	1
Number of Nulls	0
Samples per symbol	12/14 (for 2.8 GHz)
Data rate pre-overhead	3 x 4 = 12 Gb/s

a)

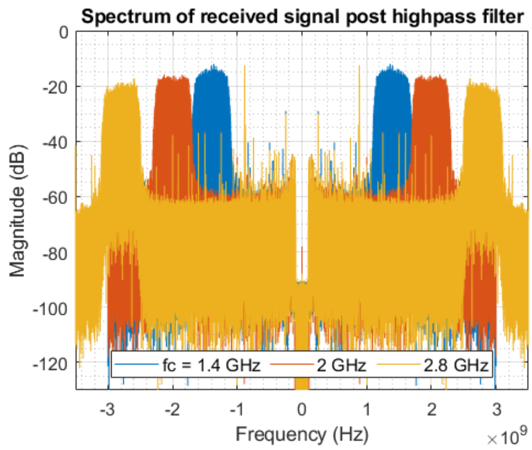

b)

Figure 104: Input parameters of the three 500 MHz 256 QAM datasets with a) the parameters table and b) the received spectrum of the three transmissions superimposed post HP filtering

The equalised constellations of each carrier 256 QAM received data are displayed in figure 105 a) to c), with the average EVM being lower at $f_c = 1.4$ GHz, which can be seen from the constellation. When plotting the EVM against the subcarrier figure 105 d) to f) (easily convertible to the corresponding frequency), the different EVM averages can be detected but also the subcarriers where errors may arise. Even though the average EVM is lower for $f_c = 1.4$ GHz than that of $f_c = 2.8$ GHz, with more EVM peaks at specific subcarriers are present for $f_c = 1.4$ GHz resulting in more errors. This idea was verified as amongst all the measurements for all carrier frequencies, $f_c = 2.8$ GHz was the data set with the least total errors. The displayed data sets all had 0 errors repeated measurements resulted in a range of errors between 0 and 9 for a total of 114688 bits sent (further characterised in section 5.2.5).

In conclusion a low error data transmission over 3 different bands using 256 QAM was acheived with a post overhead data rate of 3 x 3.39 Gb/s and in total 10.17 Gb/s; this value could once again be increased by decreasing the overhead with more data symbols and frames.

5.2.3 BER measurements

To further evaluate the BER performance, two data sets were generated with a larger number of bits transmitted over a longer time period.

In the results presented, two data sets were analysed with the properties presented in table 6, the first data set has a total of 4902912 bits and the second one 11820168 bits, one error would result in a BER of 2.04×10^{-7} and 8.46×10^{-8} respectively. The data rate post overhead of each data set is 12.06 and 12.08 Gb/s and the running length in time is 0.407 ms for the 20 frames one and 1 ms for the 50 frames one.

A few runs of each of the two data sets were measured and the results are displayed in table 7. In the second data set, the 2.4 GHz ISM band was excluded by nulling 76 subcarriers which correspond to the band. Looking at the results, both data sets had similar results in terms of EVM (2.59 % data set 1, 2.31 % data set 2) and BER with an overall bit error rate of 2.25×10^{-5} over the 10 signals measured.

Further detail on the errors is given in the "Frequency of error subcarriers" column, in the first data set, three error bands are detected including one in the early Wi-Fi band and two othere at 1.06 and

Property	Value
Modulation	64 QAM
Carrier frequency (fc)	2.1 GHz
Bandwidth	2083 MHz
Subcarriers (Nc)	2048
Cyclic prefix length	64
OFDM symbols/frame	20 / 50
Number of frames	20
Number of Nulls	0 / 76
Samples per symbol	6
Data rate pre-overhead	12.5 Gb/s

Table 6: Parameters table for the BER test data sets

Dataset	Symbols in 1 frame	Frames	Total EVM	Errors number	BER	Frequency of error subcarriers
			%			GHz
1	20	20	2.46	0	0.00E+00	NA
1	20	20	2.61	0	0.00E+00	NA
1	20	20	2.83	384	7.83E-05	1.061 & 1.960-1.964
1	20	20	2.42	0	0.00E+00	NA
1	20	20	2.61	183	3.73E-05	2.403-2.4009
2	50	20	2.23	0	0.00E+00	NA
2	50	20	2.54	0	0.00E+00	NA
2	50	20	2.20	0	0.00E+00	NA
2	50	20	2.39	584	4.94E-05	2.885-2.890
2	50	20	2.20	713	6.04E-05	2.847-2.851
Average BER					**2.25E-05**	

Table 7: Detailed BER experiment results with the total average BER for both data sets being 2.25×10^{-5}

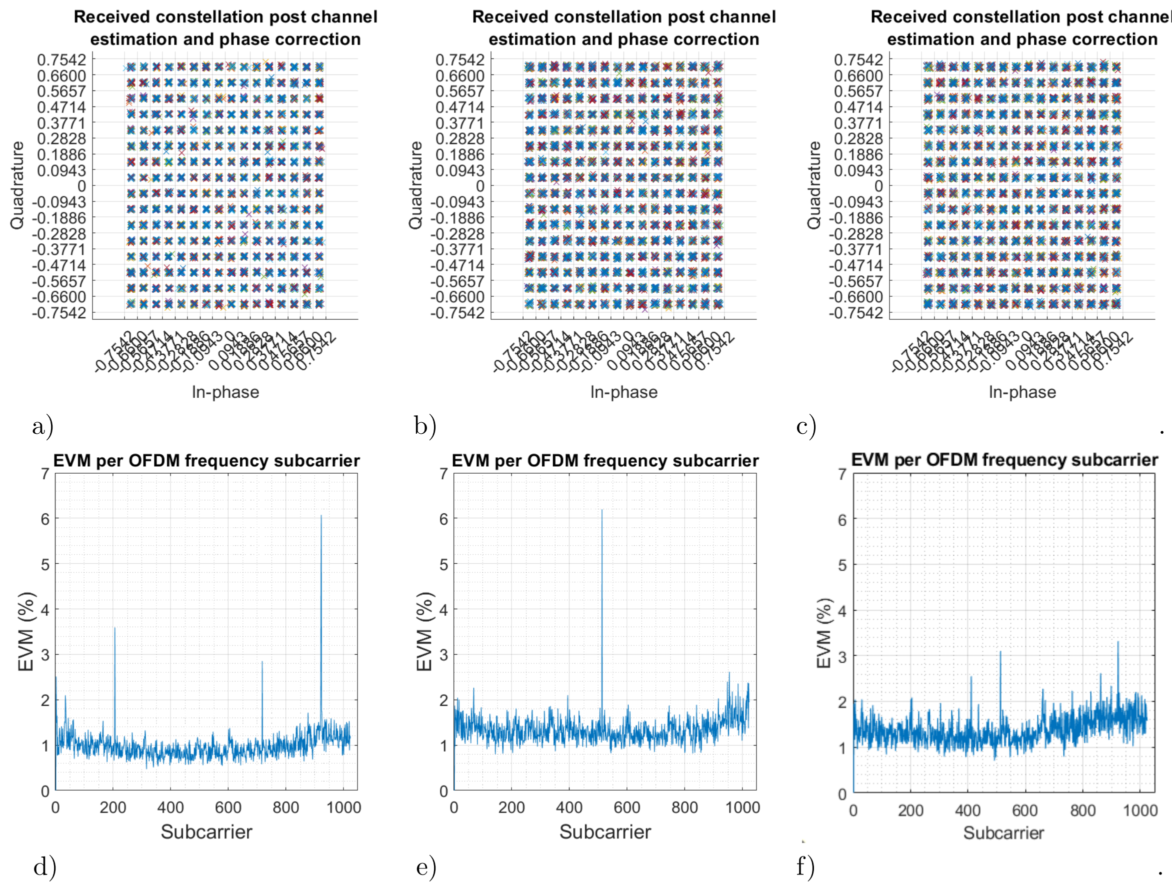

Figure 105: Results post processing of the three 256 QAM data transmission with the constellations at a) f_c = 1.4 GHz, EVM = 1.06 % b) f_c = 2 GHz, EVM = 1.41 % and c) f_c = 2.8 GHz EVM = 1.44 % and the corresponding EVM against subcarrier plots in d), e) and f)

1.96 GHz. In the second one, the error bands were at much higher and closer frequencies around 2.85 and 2.89 GHz.

The errors observed in the BER datasets table 7 only occured on a few measurements, 6 out of 10 measurements were error-free. The error frequency location were on one or two narrow bands for the measurements exhibiting errors, with a maximum width of 6 MHz (very narrow compared to the 2 GHz transmission). The error bands varied from one measurement to another even within the same dataset.

Nulling such error bands with real-time feedback implementation would result in practically unchanged data rates, and noticeably decrease the error rate. Furthermore the error rate remained below 8×10^{-5} across all measurements which is still within acceptable limits for error corrections.

Compared to current high data rate standards, the obtained error rate is a bit higher, however the the generator design does not include any coding, neither does it include feedback on the channel response to adjust the channels nulled or bit loading. Looking at literature [116], various LDPC and RS-FEC codes have been demonstrated for a range of input BER in the region of 1×10^{-3} to 1×10^{-2} resulting in an error corrected BER of 1×10^{-12}. Should such a scheme be implemented in the data generation and processing of our SW link, the BER of the experiment can be expected to similarly reduce, therefore fitting the error requirements of telecommunications standards. This error reduction would also allow higher order modulation and data rate as well as allowing better performance of longer links.

5.2.4 High frequency data transmission

The results presented in the previous sections show the potential of the system in the 1 to 3.2 GHz band, however the overall transmission band of the surface wave does not suffer a theoretical cut off frequency as seen in other transmission lines.

When looking back at the s-parameters figure 54 a), another transmission band can be exploited, the 4.2 to 6.5 GHz band described in the thesis as the high frequency band. Moreover, surface wave was defined as having a low attenuation at high frequencies, only limited by the dielectric insulation of the conductor and the design of the launchers.

As explained in the launcher part, the antenna was designed for a broadband performance but was not optimised for the higher frequency range especially due to the FR4 substrate.

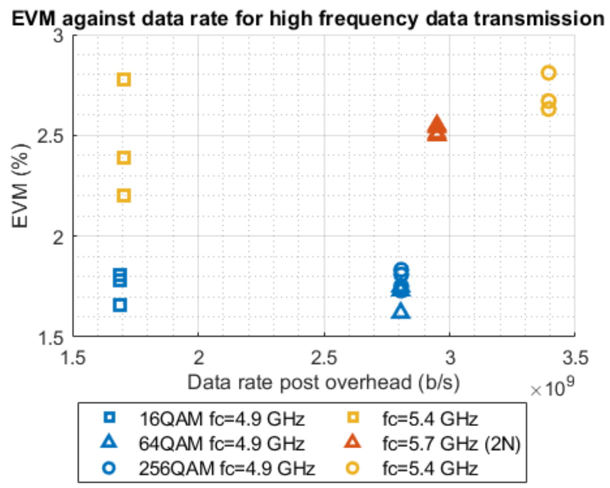

a)

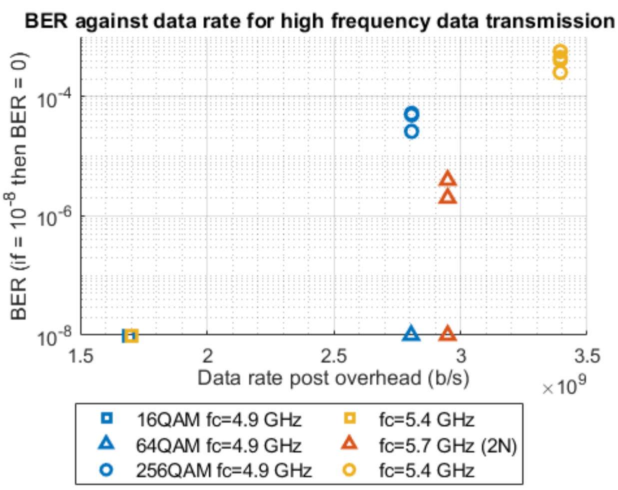

b)

Figure 106: Results of data transmission over the 5 GHz frequency band with a) the EVM and b) the BER against the calculated post-overhead data rate - bit error rates of 10^{-8} show an transmission with 0 errors due to the logarithmic scale

To show the potential at higher frequencies further transmission tests were carried out between 4.5 and 6 GHz, with various modulation orders, transmission bandwidth and carrier frequencies. The summary of the obtained results is shown in figure 106 a) and b) with the calculated EVM and BER respectively post-processing against the post-overhead data rate.

In the figure legend, the marker colour represents the carrier frequency (4.9 blue, 5.4 yellow and 5.7 GHz red), the marker shape represents the modulation format (square 16 QAM, triangle 64 QAM and circle 256 QAM) and the writing (2N) means that two subcarriers have been nulled.

The data sets have been designed separately, with various symbols per frame, number of subcarrier and nulled subcarriers but a single frame for all, hence displaying the results against the post overhead data rate which is more representative of the transmissions.

The results from lower modulation order resulted in no errors over the dataset length, as would be expected. However, once the QAM order was increased, some errors arose. Both 64 QAM datasets were improved by having a couple of nulled subcarriers meaning their resulting error rate was 0 or below 0.5 $\times 10^{-5}$, which with no coding or DMT implemented remains a low BER. For the 256QAM measurements, the 3.4 Gb/s transmission outputted an error rate of 4×10^{-5} to 5×10^{-4}. Looking at both BER and EVM plots, between similar datasets at 2 carrier frequencies, lower frequencies generally performed better, which follows expectations from the link's channel response being approximately low pass.

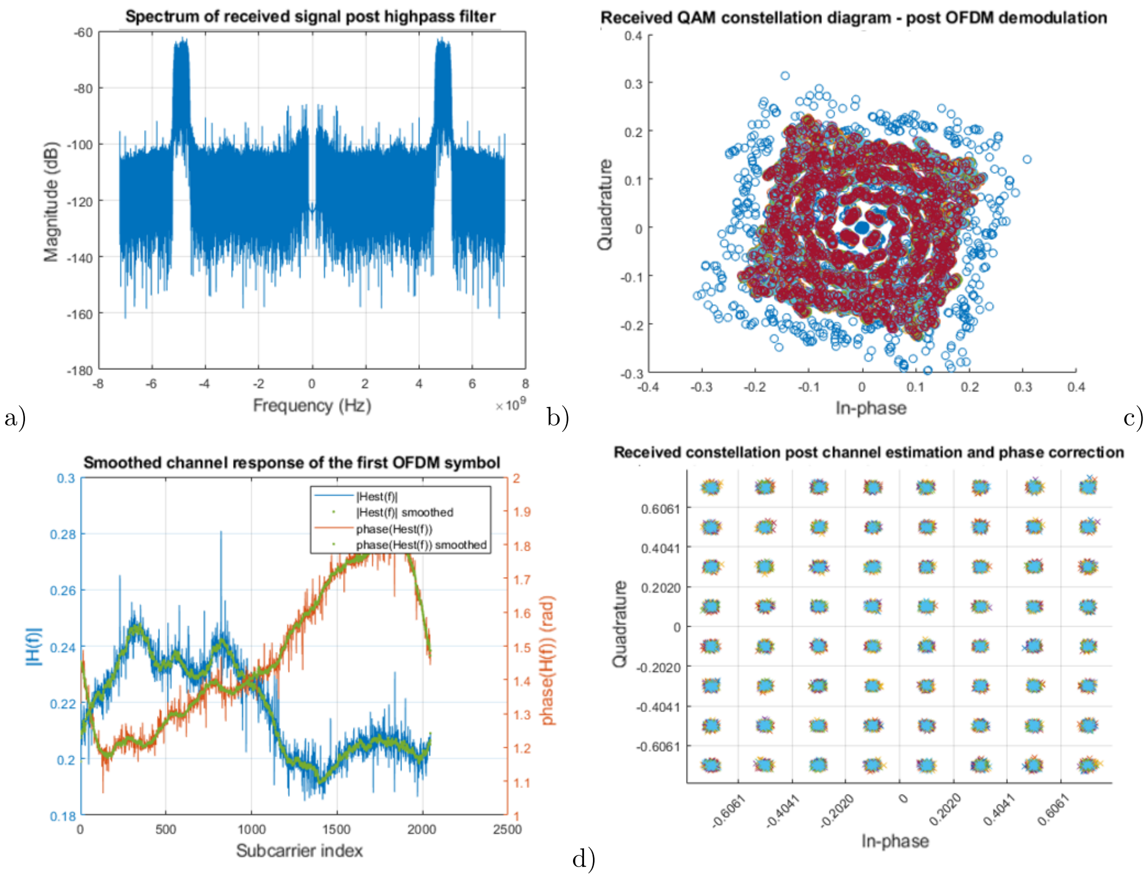

Figure 107: Results of a single high frequency band data transmission of a 64 QAM 533 MHz bandwidth at f_c = 4.9 GHz with a) the received and HP filtered spectrum, b) the constellation post OFDM demodulation, c) the channel response estimate and d) the equalised constellation with EVM = 1.75 %

One of the higher data rate and lower BER data set was chosen for a more detailled analysis on the high frequency transmission, a 64 QAM at 4.9 GHz transmitting 3.2 Gb/s pre-overhead (blue triangles on figure 106). The detailed processing results of the data set displayed with 64 QAM, 533 MHz bandwidth with a carrier frequency of 4.9 GHz, 2048 subcarriers (with 2 nulls at 5 GHz) and 20 symbols per frame is displayed in figure 107. The overall result post data processing and equalisation was EVM = 1.75 % and BER = 0, with no scattering in the equalised constellation.

Compared to the lower carrier frequency (besides the narrower bandwidth), the constellation is less scattered resulting in the lower EVM, this may be due to the channel response being flatter, less oscillating and over a smaller amplitude range, 0.19-0.25 compared to 0.24-0.5 for the lower carrier frequency band. Another possibility is the subchannel bandwidth, both channels are divided in 2048 subchannels (including 2 nulls), but the lower f_c is 2083 MHz wide and the higher f_c 533 MHz wide, resulting in a subchannel bandwidth of 1017 kHz and 260 kHz respectively, which is closer to the G.fast subchannel bandwidth of 51.75 kHz [117].

5.2.5 Error and interference analysis

Throughout the experiments one of the main aims is to reduce the number of errors and have a higher quality of transmission.

The errors observed could be split into two categories: firstly subcarriers with errors over many or all symbols, which were generally repeatable. These subcarriers also exhibited a poor H(f) compared to neighbouring subcarriers, so the SNR at the receiver may have been insufficient for the chosen modulation order, which could be resolved by bit loading with minimal reduction in the overall data capacity, since few subcarrier were affected. Secondly, bursts of errors on subcarriers which were not repeatable but often occur on the same subcarrier or group of subcarriers; it is thought that these are caused by RF interference.

In theory surface waves do not radiate, yet interference in common wireless bands could be seen with a spectrum analyser for example in the noise level figure 66, a possible explanation is radiation occurring from the launchers at the EM mode conversion.

To investigate the nature of the errors, the 256 QAM data type presented in figure 104 was swept over 8 overlapping carrier frequencies: $f_c = [1.4, 1.6, 1.8, 2, 2.2, 2.6, 2.8, 3]$. The resulting errors (peaks at either 1 or -1) and channel estimates against the frequency are plotted in figure 108.

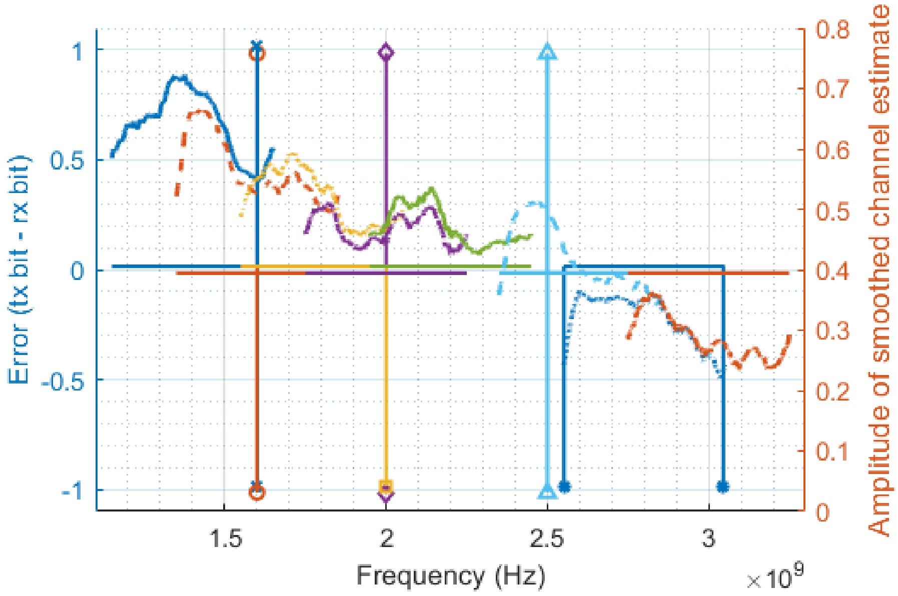

Figure 108: Error characterisation over the 1 to 3.3 GHz frequency range with 8 carrier frequencies showing on the left side the errors calculated by substracted the expected bit to the detected one and on the right side the calculated channel estimate amplitude - a slight offset between the error lines was added on the y-axis for clarity purposes

This plot summarises the relationship between the error location and channel response trend and consequently the SNR. Each colour and marker represents a different carrier frequency allowing clarity for overlapping errors and channel response. From an initial overview, the estimated channel responses (H(f)) seem to match from one data set and carrier frequency to another, but tend to differ at the begining and end of the measured band. As for the error frequency locations, both $f_c = 1.4$ GHz the blue cross and $f_c = 1.6$ GHz the orange circle produce an error frequency = 1.6 GHz, (same goes for the purple diamond ($f_c = 2$ GHz) and the yellow circle ($f_c = 1.8$ GHz) at the error frequency of 2 GHz). The error locations also seem to correlate with local minima parts of the channel response, as seen at 1.6, 2. As for 2.55 and 3.05 GHz they seem to be resulting from edge effects low pass response.

This exhibits a poor performance at the specified subcarriers due to either one of the reasons mentioned earlier. In a practical system, a feedback mechanism could be employed so such frequencies would be either nulled or filled with a lower modulation order symbol, reducing the recurring error points greatly.

In more detail, the number of errors varies from 0 to 19 out of 114688 transmitted bits for each data set plotted. The BER is then ranging from 8.72×10^{-6} for 1 error and 1.66×10^{-4} for 19 errors. Their EVM ranges from 1.7 to 2.9 % and averages at 2.3 %, as predicted by the S21 trend, its value increases as the carrier frequency increases. Nevertheless, lower EVM values do not correlate with lowest error number and vice versa. Meaning that local irregularities (especially minima) of the channel response may be more of a cause to recurring errors. The reason needs to be explored further but may be because of a bad channel estimate or unfitting for the considered frequency band (high variation over the whole subchannel band). The only point that was not located in such an area on the corresponding $| H(f) |$ was found just below 2.5 GHz which can be then linked to Wi-Fi interference. Beyond characterising the error location, source and how to avoid them, this experiment has witnessed the potential to transmit low error and high modulation order data sets over a 2.15 GHz wide frequency range.

Another aspect from the channel estimate in figure 108 that was noticed, is the slight mismatch between the calculated frequency response of the link through the equalisation compared to the measurements through the VNA figure 54 a) (comparison when both are either on a linear or a logarithmic scale).

5.2.6 Length and power comparison

Although surface wave application will require longer transmission distances, practical constraints prevent longer distance transmissions experiments, therefore we compare a shorter link to obtain trends of the link performance with distance. In this case the 6.1 cable used throughout the OFDM experiments results and a shorter 3.15 m wire shown in the s-parameter measurements and used for attenuation and launcher loss calculations are compared.

The same data set was tested on both links using the same launchers and overall setup as presented in figure 57. The data created was kept simple with a 16 QAM modulation, 500 MHz bandwidth at f_c = 2.2 GHz and with 10 symbols per frame resulting in a post overhead data rate of 1.59 Gb/s.

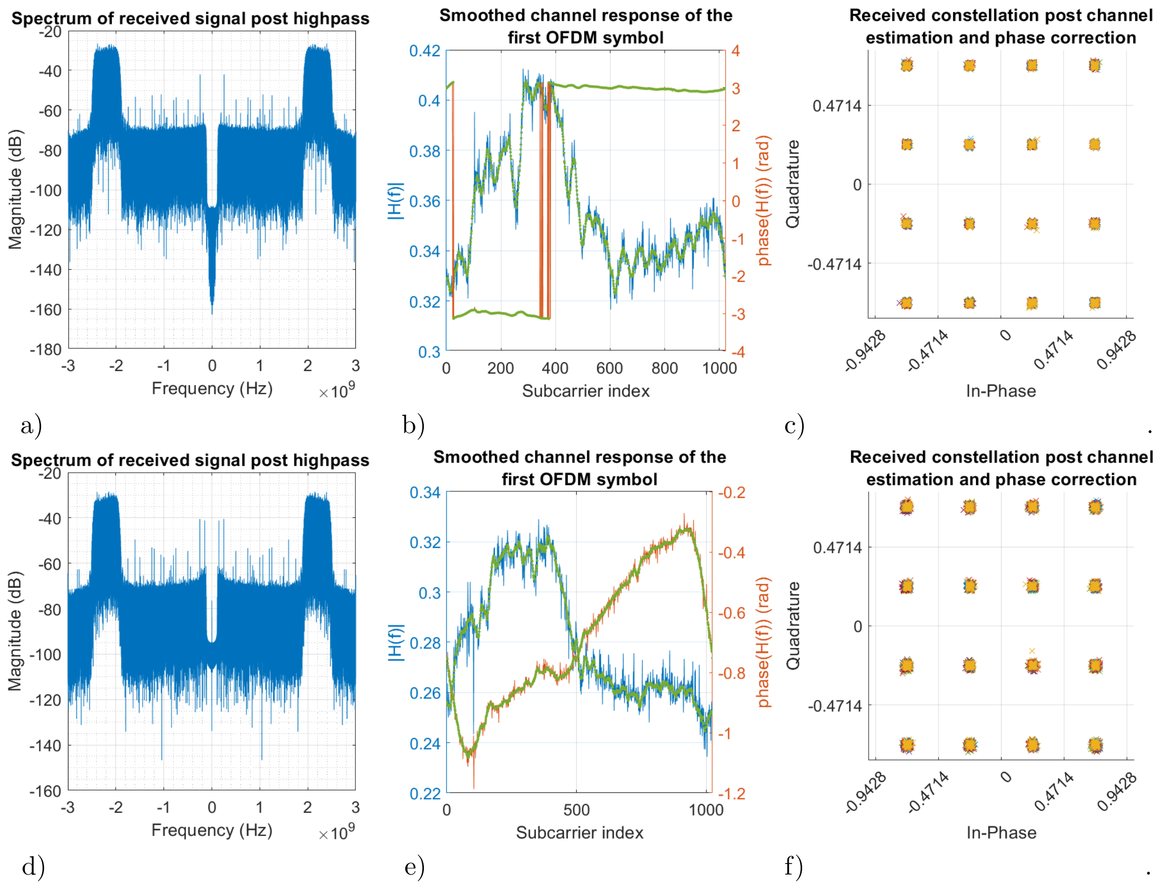

Figure 109: Result comparison of a 16 QAM 500 MHz datset between the two wire lengths with at the top the 3.15 m link resulting in EVM = 0.95 % and at the bottom the 6.1 m link resulting in EVM = 1.91 % a) and d) the received and HP filtered spectrum, b) and e) the channel amplitude and phase estimates, c) and f) the equalised constellations

The results from the two transmission lengths are displayed in figure 109. Firstly, the spectrum of the received signal is displayed, looking at the amplitude, a very slight difference can be seen in the measurements, same goes for the time domain signal captured from the oscilloscope ($\pm 0.08V$ for the 3 m link and $\pm 0.06V$ for the 6 m link). Looking at the channel estimate, the magnitude trend is similar but with a few dissimilarities and with a lower amplitude, as for the phase response it was mentioned previously that even with the same link and data set it varies against time. Finally the constellation is once again comparable with slightly higher EVM results for the longer link, 0.95 % at 3 m and 1.91 % at 6 m.

From the two measurements, 3 and 6 metre links output comparable results with slight EVM degradation for the longer one. Further work on different link length data transmission may be explored for comparing with extrapolation results in terms of data transmission.

The highest data rate of 12 Gb/s was demonstrated on a 6.1 m surface wave link, with an average error rate of 2.25×10^{-5}. OFDM modulated signals were transmitted with a variety of modulation orders, transmission bandwidth and frequency ranges, showing a strong potential of surface wave data transmission. Error characterisation allowed to determine the need for feedback implementation both in bit loading (or channel allocation) and forward error coding. This would result in much lower error rates and allow high performance over longer links.

Single carrier modulation has also displayed high data rates (up to 12.5 Gb/s pre-overhead) but due to a more challenging equalisation for such a wide bandwidth, the transmission length was limited and results were unpredictable.

Compared to the single carrier QAM transmission, OFDM modulation allowed similar data rates over more complex and longer wire structure . Furthermore, the data processing complexity was significantly decreased, and low error results more easily reproducible. This confirms the use for frequency multiplexing in wideband data transmission, including surface wave communications.

Transmitting signal over multiple bands with a high order modulation has demonstrated good performance and the potential of data rate increase with narrower total transmission bandwidth.

Error characterisation has proven that further improvement could be brought to surface wave data transmission by implementing forward error coding, bit loading and subcarrier nulling through feedback implementation. Such processes would allow significant BER reduction and make surface wave good candidate for high throughput wired data transmission.

6 Results extrapolation the using water-filling algorithm

Following the experimental data transmission results where the length was limited by experimental constraints, a strong interest lied in knowing how much data could be transmitted over longer cable links. Such predictions could be calculated using the earlier presented water-filling algorithm with an extrapolation of the surface wave channel.

The code was modified to calculate the cable attenuation per unit length from at least two different lengths measurements (in this case 3 and 6 m) and then multiplying it by the desired link length. It was shown earlier that in the case of a few surface wave links, cascading S-parameters resulted in very similar responses as S to ABCD parameters conversion. In a similar manner, the response of the two SW launchers was removed and added back to the channel response unmodified. Their respective response are shown in figures 54 b) and 63 b). The overall calculated response for a 100 m DW11 link with the launcher from figure 63 a) is plotted in figure 110 as well as the measured response for two lengths links.

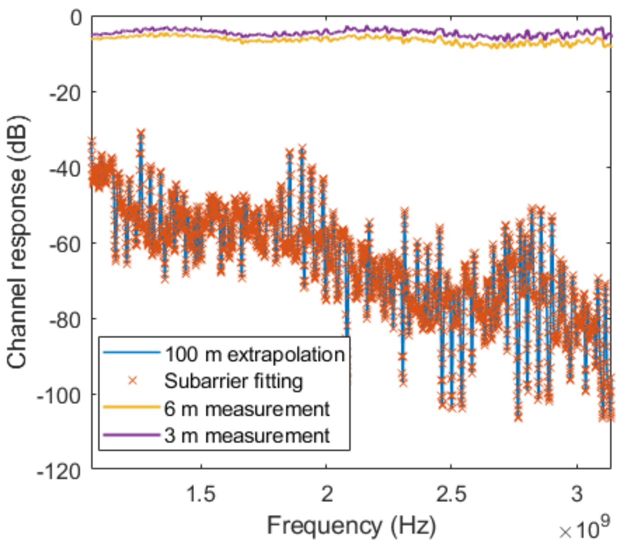

Figure 110: 100 m DW11 link extrapolated channel response magnitude with the fitted subcarrier points and the two shorter measured S21

In the extrapolation, the noise level was taken as a fixed -150 dBm/Hz because interference measurements in the laboratory were mostly affected by indoor wireless signals, such as Wi-Fi. Due to less predictable interferences in other environments especially over longer lengths up to 100 metres, the response measured in an indoor lab was less relevant for the extrapolation of an underground access network application.

The total bit rate and transmit power were calculated for the power budget of 10 and 20 dBm, displayed in figure 111. Comparing to the 6.1 m results, both from the simulations and experiments, the predicted data rate is greatly reduced from about 29 Gb/s and 12 Gb/s over 6 m respectively to 3 or 6 Gb/s over 100 m depending on the defined power budget.

6.1 Extrapolation for multiple lengths

Beyond the initial 100m extrapolation, one of the first parameters of interest is the effect of length on the transmission properties such as transmit power and data rate.

The channel response at various lengths is represented in figure 111 a) where 4 different lengths are represented. In figure 112 b), the total power transmitted and data rate generated are plotted from 10 to 200 m links, with P_{budget} = 20 dBm and *bit cap* = 15 bit/s/Hz.

It can be seen that the power and data rate curves have an inverse relationship with respect to the link length. From about 40 metres, the data rate starts decreasing while the power saturates to the

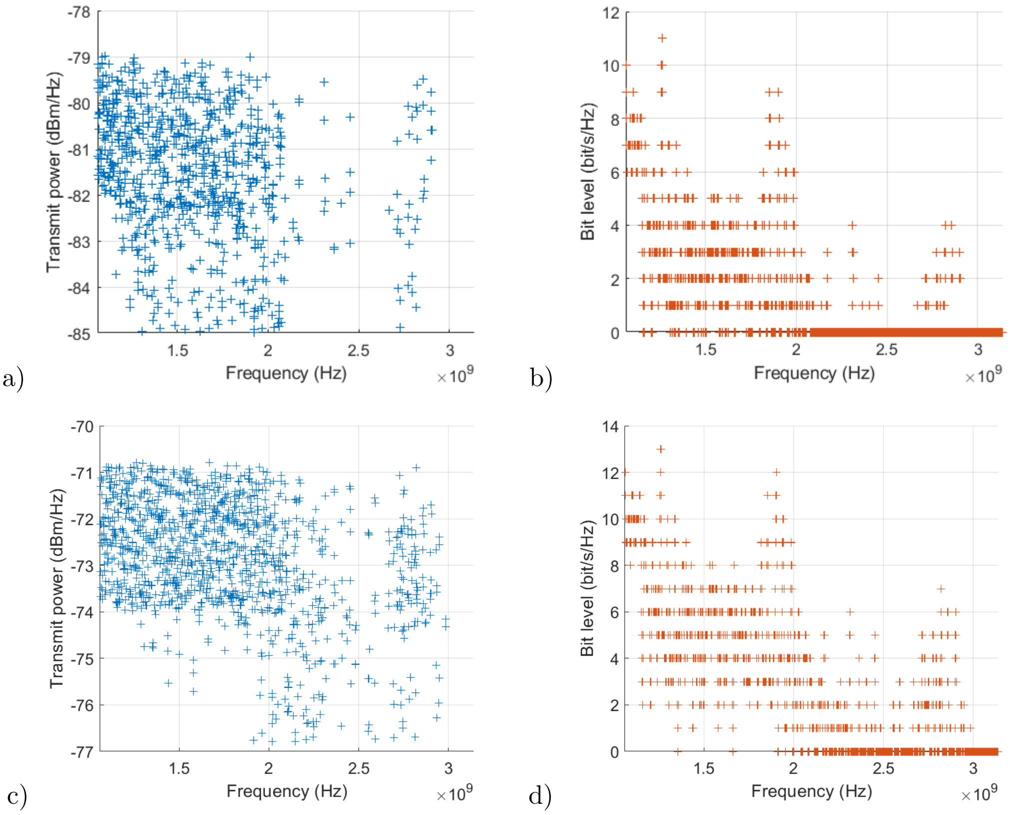

Figure 111: Water-filling bit and power loading of a 100 m link with a power budget of 10 dBm (top) and 20 dBm (bottom) resulting in the total transmit power and data rate: a) P_{tot} =**8.1 dBm** b) b_{tot} **= 2.89 Gb/s** c) P_{tot} **= 18.3 dBm** and d) b_{tot} **= 6.02 Gb/s**

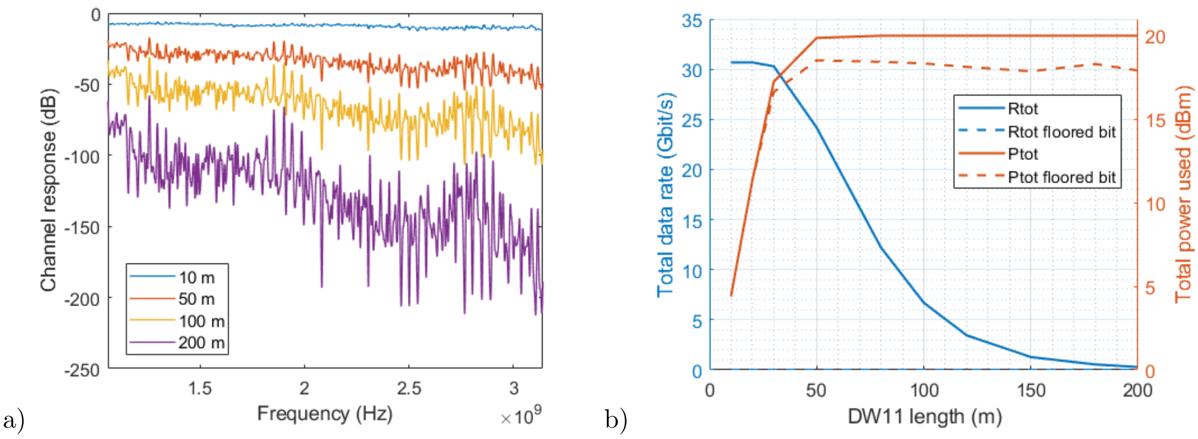

Figure 112: Results of various length extrapolations with a) the calculated channel response of 4 cable lengths and b) the total transmit power and bit rate with *bit cap* = 15 bit/s/Hz and P_{budget} = 20 dBm

available budget, with the steepest points between 50 and 100 m reducing from about 25 Gb/s to around 7 Gb/s. Using a higher power budget would likely reach higher data rates at longer lengths, yet this would still reach a limit with the available SNR between the channel responses and noise level.

6.2 Effect of smoothed attenuation

In figure 112 a), it is clear that some of the irregularities from the experimental VNA measurement of 3 and 6 m links have been amplified by the extrapolation process. It was observed from shared (unpublished) measurements that when calculating the attenuation from multiple cable lengths, the average attenuation results in a smoothed version of the individual calculated attenuations (using only 2 cable lengths). It was therefore of interest to observe the extrapolated channel response and water-filling results when using a moving average (Matlab function) over the attenuation calculation.

In figure 113, the channel response and capacity calculation is given for various moving average windows on a 100 m DW11 line. This means that the attenuation is initially calculated as before and then processed by taking a moving average of each points over a specified window length, x, consisting of $x/2$ points on each side of the current data point.

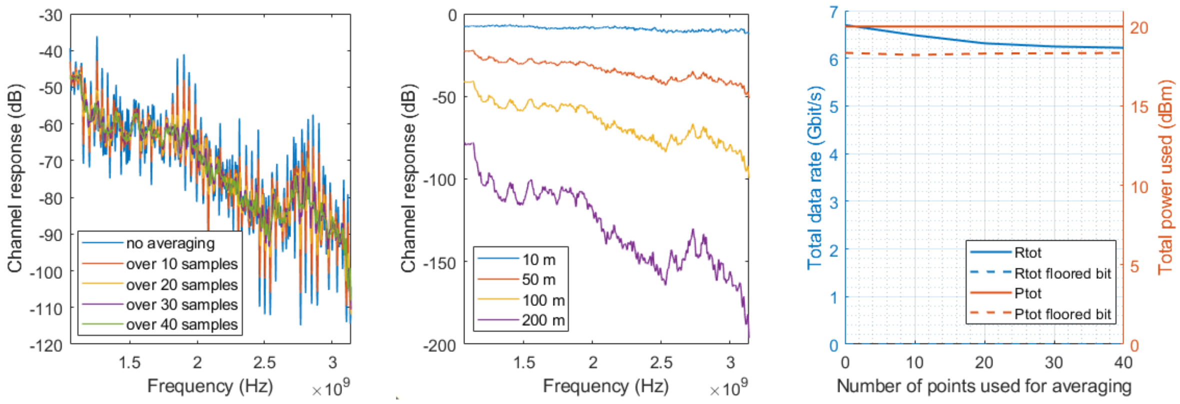

Figure 113: Calculated DW11 100 m water-filling results with smoothed attenuation using various moving average window lengths (none, 10, 20, 30 and 40 samples) with a) the channel response of a 100 m link, b) the response with a window length of 40 samples for 4 lengths (can be compared with the previous plots) and c) the obtained data rate and transmit power against the window length in samples

From the plots, the calculated power and data rate undergo very little change with increasing smoothing, other than a loss of about 0.4 Gb/s in capacity and no change in terms of transmitted power. This may due to some of the variations predicting much higher SNR (as well as lower) and therefore allowing higher bit loading.

It is worth noting that smoother results for longer lines would be consistent with the ripples from impedance mismatch reducing over longer lengths.

6.3 Fixed length, power bit loading and bandwidth effects

Similar to the capacity calculations section, one of the main interests is to observe the system response to various parameters, in this case the power budget and the bit cap.

Simulations were carried on a 100 m line with on the one side a fixed power budget of 20 dBm and on the other side a fixed bit cap of 15 bits/s/Hz.

Figure 114 a) shows that both the data rate and total transmit power both increase with the increasing bit cap, however they reach a maximum value around 10 bit/s/Hz limited by the available SNR (dependent on the channel response and noise floor).

Figure 114 b) shows variation with power budget, both the transmitted power and total data rate increase with increasing available power until they reach a maximum with P_{budget} = 45 dBm when all subcarriers reach their maximum bit loading. The transmitted power saturates at about 42 dBm and the data rate around 17 Gb/s; compared to the 6 m link, the power necessary is doubled and the maximum

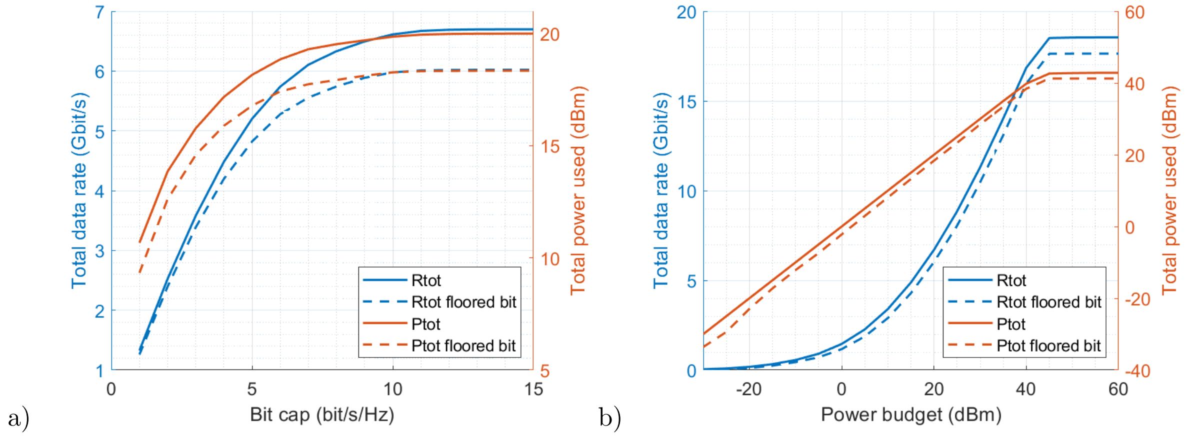

Figure 114: Total bit rate and power used varying cap parameters with a) varying bit cap between 1 and 15 bit/s/Hz and b) varying power budget between -30 and 60 dBm over a 100 m extrapolated DW11 link

achievable data rate is almost halved but the trends are similar.

So far the calculations have mostly been focussed on extrapolating the experimental results to longer links but keeping the same frequency band as in section 5.2.2. However, looking at the channel response, a bandwidth larger than 2 GHz is available for data transmission, even in the low frequency range. The bit and power loading is then simulated for a link of variable transmission bandwidths, the centre frequency was taken as 2 GHz and the results for two links lengths is plotted in figure 115 a) 100 m and b) 50 m.

In the calculations, the number of subcarriers was adjusted as the bandwidth was increasing in order to keep the subchannel bandwidth approximately constant.

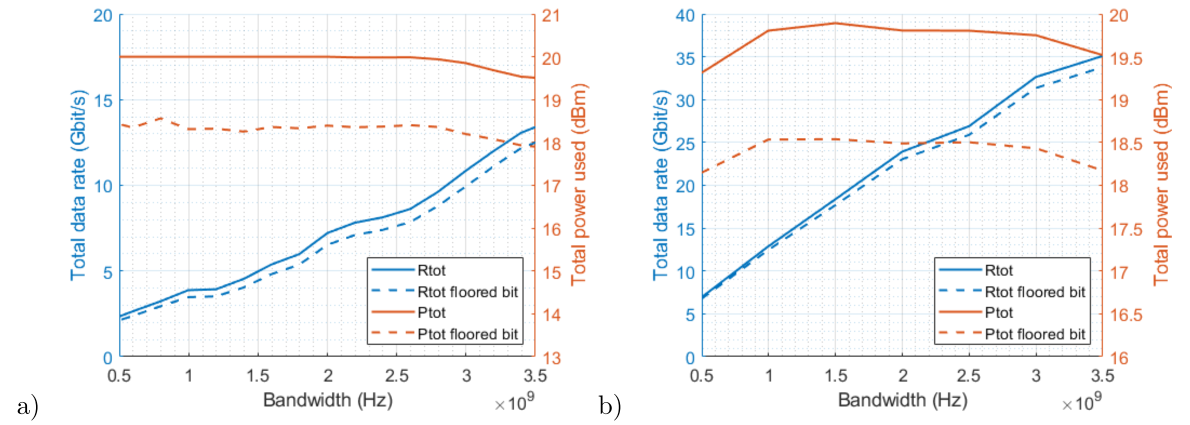

Figure 115: Total bit rate and power used against varying transmission bandwidth (0.5 to 3.5 GHz) over a) a 100 m DW11 link and b) a 50 m DW11 link with $bit\ cap$ = 15 bit/s/Hz and P_{budget} = 20 dBm

The power and data rate trends are very similar between the 100 and 50 m plots. The total power is relatively constant with the choice of bandwidth, this may be due to power being allocated to lower SNR subchannels which would achieve lower data rates with higher power necessity but using all the power available. On the contrary, the data rate increases (almost linearly) with the transmission bandwidth as expected from the initial capacity formulas. The data rates reach values of up to 13.5 Gb/s at 100m and 35 Gb/s at 50 m for bandwidths of 3.5 GHz.

6.4 High frequency transmission extrapolation

Other than the 0.5-3.5 GHz frequency range, another transmission range is distinguishable when looking at the measured s-parameters (figure 54), the 4.2-6.5 GHz range. A few experiments were once again carried out over this range in the previous chapter, but unlike the lower frequency range, the data transmission was not fully optimised.

The results for the water-filling algorithm over the 5 GHz frequency range are shown in figure 116 and 117. Unless specified otherwise, the plots are using a carrier frequency of 5.2 GHz, a bandwidth of 1.6 GHz, a power cap of 20 dBm and bit cap of 15 bit/s/Hz.

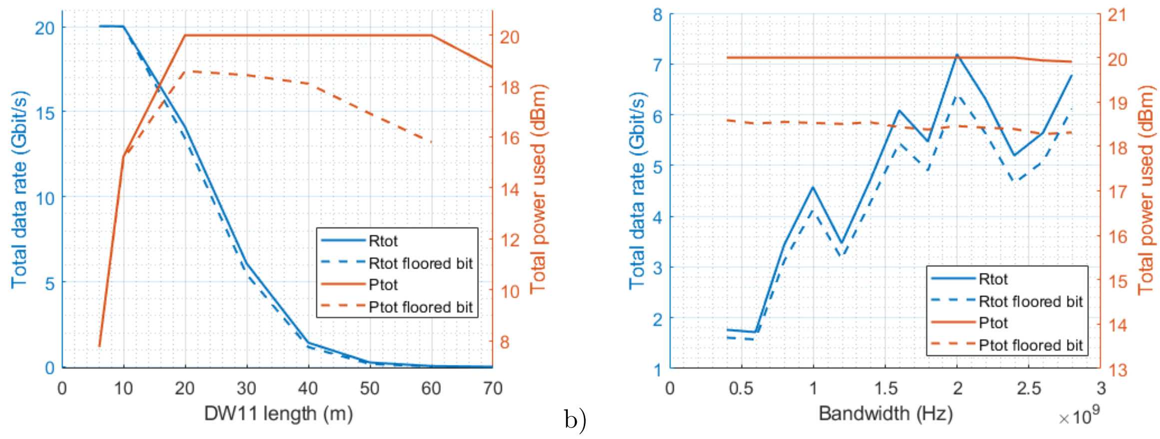

a) b)

Figure 116: High frequency range water-filling results with $f_c = 5.2$ GHz against a) the link length (bandwidth = 1.6 GHz) and b) the transmission bandwidth (cable length = 30 m) and *bit cap* = 15 bit/s/Hz, $P_{budget} = 20$ dBm

Looking at the response against the link length and with a fixed 20 dB power budget, almost no data is transmitted beyond 50 metres. Hence a length of 30 m was chosen for the following plots, which for the parameter set predicts a data rate of around 6 Gb/s. At the lowest length link, the data rates reach a value of 20 Gb/s for length of 6 and 10 metres, which could be taken as an absolute maximum with all subchannels capped loaded with 15 bit/s/Hz.

In figure 116 b), the effect of transmission bandwidth was plotted for the defined high frequency link. The response is quite similar to the 0.5 - 3.5 GHz frequency range, with a constant power for all bandwidths and an increasing data rate from around 1.5 to 7 Gb/s for the considered bandwidth range.

Unlike the 0.5 - 3.5 GHz frequency range, the data rate to transmission bandwidth relation is less smooth, this may be due to the code not using enough iterations to get convergence (although it did not seem to be an issue until this point).

The other two parameters of interest are the bit cap and the power budget set for the water-filling simulations, the obtained results are shown in figure 117.

In figure 117 which shows the effect of varying bit cap, both data rate and transmission power can be seen to saturate from about 7 bit/s/Hz to the values of 5.5 (floored) and 6 Gb/s and 18.5 (floored) and 20 dBm. In terms of varying the power budget, with more power available, higher data rates are reached, until saturation from $P_{budget} = 42$ dBm with the maximum data rate being about 17.5 Gb/s. This value is still a little inferior to data rates obtained in the different lengths simulations (figure 112), which is therefore limited by the system's SNR.

The results obtained for the high frequency range are a fair amount lower than the ones obtained for the 2 GHz frequency range, especially since the simulations for the 5 GHz frequencies are over a 30 m line compared to the 100 m line for the 2 GHz range. With the given power budget, the SNR is limiting the number of bits allocated to the subcarriers, as the calculated channel amplitude ranges between -27 and -38 dB in the 5.4 to 6 GHz frequency range (compared to -16 to -50 dB for the 2 GHz carrier frequency channel). The antenna used was designed to have a wideband operating range, however due to the substrate of the launcher being FR4 its response at high frequencies may be worsened.

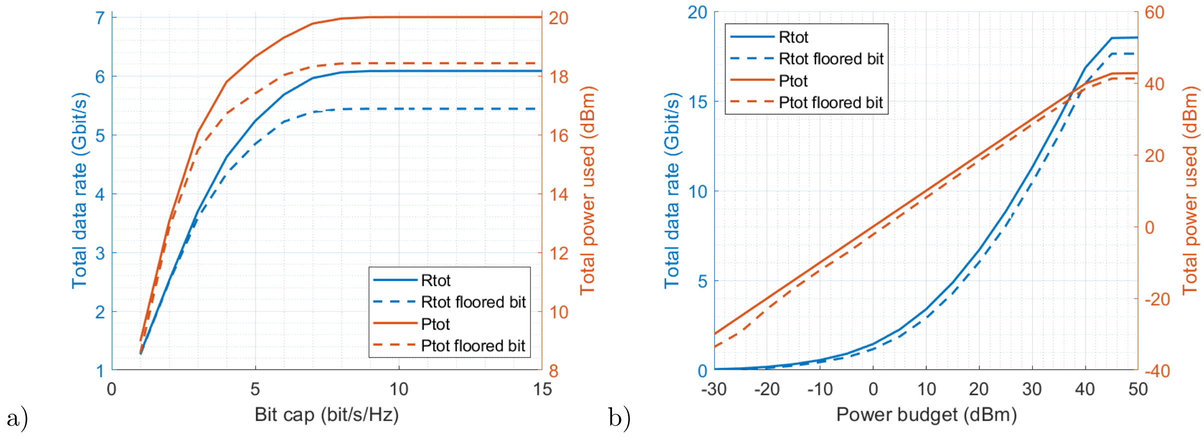

Figure 117: High frequency range water-filling results with $f_c = 5.2$ GHz against a) the bit cap from 1 to 15 bit/s/Hz ($P_{budget} = 20$ dBm) and b) the power budget ($bit\ cap = 15$ bit/s/Hz) and with a fixed cable length of 30 m and transmission bandwidth of 1.6 GHz

Other methods of extrapolating results either to longer lengths or simply with higher precision have been explored within the research group. It is a higher end version of the process presented in the Simulink simulation (Appendix). A fitting of the measured s-parameters is done in the time domain and used as a transmission link. Once again with multiple length links on the same antennas and cable type, various length links can be calculated and therefore used as transmission links themselves. Simulations of such links using the same data generator and processor have shown encouraging results. Furthermore having the fitting going between time and frequency domains, it has allowed further processing using time gating. Such a process will then remove any signal due to reflections at certain time intervals and give a cleaner response of the signal sent only. This was especially an issue in the measured link as they are of shorter lengths and hence more susceptible to reflection impairments.

An estimate of longer length transmission over the DW11 surface wave link was obtained with channel response extrapolated through S-parameter calculations and water filling simulation.

Using similar parameters to the 64 QAM BER lab experiments, with a power budget of 20 dBm, bit loading up to 15 bit/s/Hz and a link length of 100 m, data rates of 6 Gb/s were reached with 18 dBm of transmit power.

Comparing such results with G.fast transmission, SW over DW11 data rates are about 4 times the data rate obtain in G.fast for 100 m links [2], this is due to a much wider operating bandwidth in the case of surface wave transmission.

The effect of parameters such as cable length, power budget, maximum bit loading, transmit bandwidth and channel response smoothing were explored. This showed that for longer lengths, one of the main factors for data rate increase is the available power budget. Another parameter which had an impact on the link capacity was the transmission bandwidth. From 0.5 to 3.5 GHz of bandwidth, data rates varied from 2 to 14 Gb/s over a 100 m link and from 6 to 35 Gb/s over 50 m.

Lastly, the higher frequency transmission band was explored between 4.2 and 6.5 GHz, similar to the experiments. With a power budget of 20 dBm, bit loading up to 15 bit/s/Hz and a link length of 30 m, data rates of 6 Gb/s were reached with 18 dBm of transmit power. Once again the power budget was the main limiting factor for higher data rates over longer links. The 5 GHz frequency band may also be limited by the SW launcher design wich was optimised for lower frequency bands.

7 Conclusion and future work

In the thesis, a full system was designed to demonstrate the capabilities of surface wave data communications. The system was then simulated and built for experimental tests on data transmission and capacity estimation. Experimental and extrapolated transmission results have shown that surface waves on legacy cables are a possible candidate for broadband communications. To implement a deployable standard from this novel transmission further work is required

The key novel findings of the research are:

– An experimental data transmission was demonstrated on a surface wave link with modulated data sets and in the excess of 10 Gb/s (12.5 Gb/s with a BER of 2.2×10^{-5}). Furthermore, the data transmission was launched from a planar horn antenna to a complex wire structure (other than a single or parallel coted or uncoated wire).

– A capacity model was built using experimental measurements of a surface wave channel response, which showed agreement with the experimental transmission (when the parameters were matched).

– Further processing on the channel response allowed the extrapolation of longer cable lengths for surface wave transmission, which was used to calculate capacity for potential applications of surface wave data communications, predicting up to 14 Gb/s at 100 m and 35 Gb/s at 50 m.

Conclusion

In the presented research, an experimental communications setup was built and data was successfully transmitted over a surface wave link.

Initial tests were performed using a data generation with QAM modulation on surface wave links with several cable types and cable lengths. In order to achieve high data rates and good performance, a wide transmission bandwidth was necessary together with an equaliser. Data rates of up to 12.5 Gb/s were reached over a 1.5 m link and up to 8 Gb/s over about 5 m. However, it was found that the link's length had a strong impact on the transmission performance in terms of EVM and bit errors. With a bandwidth of 1 GHz or above and the increasing links lengths, the channel response became less uniform and the equaliser used was not sufficient for such correction.

A modulation adapted to wide bandwidth transmission was then chosen for a setup closer to the desired application, orthogonal frequency division multiplexing. A 12 Gb/s SW data transmission was achieved over a 6.1 m DW11 cable with a resulting BER of 2.2×10^{-5} at $f_c = 2.1$ GHz. In this experiment the transmission length was limited by the laboratory's dimensions hence requiring extrapolation for longer length transmission. Solutions were proposed to improve the output BER based on existing data transmission standards results.

To our knowledge this is the first demonstration of a modulated data transmission over a surface wave link, as well as data rates transmission beyond 10 Gb/s [118]. Comparatively to G.fast, the demonstrated data rates are up to 6 times higher than the 200 MHz bandwidth G.fast transmission (up to 50 m). Such data rate increase comes from the much wider bandwidth available to surface wave transmission, with over 2 GHz in the OFDM data demonstration. Another main difference besides the length and bandwidth is the modulation used, G.fast used bit loading with up to 14 bit/s/Hz whereas the presented data uses a single order modulation of 64 QAM (6 bit/s/Hz).

Surface wave capacity was estimated using various calculation models, data rates close to theoretical limits were calculated using Shannon models, using both theoretical and experimental wire attenuation values for various frequency ranges. Similar models for surface wave capacity estimations have been demonstrated in [11][119][120] using theoretical SW attenuation and mostly focussing on the mm-Wave to THz frequency range. Data rates of 1.7, 17 and 170 Gb/s were predicted for $f_c = 1$, 10 and 100 GHz with a constant fractional bandwidth of $f_c/5$ for link lengths of 1500, 500 and 100 m with a modulation of 256 QAM.

Another simulation for capacity calculation was presented, the transmitted data rate is calculated by a water-filling algorithm together with the transmitted power. A measured surface wave link channel response together with background noise measurements were to represent the channel to which the water-filling is applied. The simulation was applied to the experimental link used in the OFDM experiment, similar results were obtained when adjusting the parameters to the experiments setting. The simulation was adapted to settings similar to G.fast standard, with a power budget of 20 dBm and a bit loading of 15 bit/s/Hz (but keeping 2 GHz bandwidth), resulting in a data rate of 30 Gb/s (with a total power of 9 dBm).

Furthermore, the channel response of various DW11 lengths were extrapolated from two lengths channel measurements (3 and 6 m). Such channel extrapolations were used to simulate data transmission over longer wire lengths with the water-filling algorithm. Therefore target lengths for surface wave data transmission may be achieved. Extrapolating the OFDM experiments results to 100 m, with up to 15 bit/s/Hz and 20 dBm, a data rate of 6 Gb/s was achieved. And when the transmission bandwidth was maximised to 3.5 GHz, data rates of 14 and 35 Gb/s were achieved for cables of 100 and 50 m. Longer lengths extrapolations have shown that surface waves indeed have the potential of reaching data rates beyond the current G.fast standard, and potentially the most recent DSL standard, G.mgfast (predicting up to 10 Gb/s for up to 30 m) [111].

In conclusion, a novel simulation approach was demonstrated in the application of surface wave capacity calculation, it is believed that with further link characterisation, this simulation could become a useful tool to predict data rates over adaptive link designs.

Additional experiments and extrapolations included data transmission over a different frequency band, between 4.2 and 6.5 GHz. The results for this frequency band were not optimised especially because of the launcher design, however, data rates of up to 3 Gb/s were demonstrated experimentally over 6.1 m and up to 7 Gb/s in simulation over a link of 30 m.

The work presented has demonstrated multigigabit experimental data transmission over a proof-of-concept SISO twisted pair surface wave link of 6.1 m. The simulation as well as the experimental results agree with the potential of reaching higher data rates with surface wave modes over copper cabling compared to the current solution. However a lot of research is still ahead in the field of surface wave data transmission to reach standards such as G.fast. Even though, G.fast and other access network standards are the result of 30 + years of research and work on data transmission, and surface wave communications is still in the early stages of its design and development.

Future work

The research carried in the PhD was an initial inspection of the potential of surface wave links with the aim of building a proof of concept data transmission setup. Several conclusions have been drawn where the limitations of the research and the necessary improvements have been highlighted in the corresponding chapters.

A data generation and processing aspect that has been mentioned throughout the experimental results, is the implementation of bit loading modulation and forward error coding both aiming to reduce errors and increase output data rates. This work would involve finding the best suited channel coding and how much it reduces the error rate and defining the bit loading limit for surface wave links (this limit varies depending on the standard).

Even though a good correlation was obtained between the simulations and experiments, one of the project's main objective was to characterise the data transmission over long link lengths. Therefore, a continuation of the work link's behaviour with increasing length is necessary, both for experimental and simulation purposes. With a better understanding of scalability simulations can become a true to experiment extrapolation tool: allowing launcher design, data processing techniques and other modification tests in reduced time and cost.

One of the points that some further simulations have shown is that a single level bit loading against a multiple level bit loading may not achieve quite as high data rates but will be much more power efficient.

Power constraints have not yet been applied to the system (experimentally) but when extending to longer links this will be an important limiting parameter.

With a successful proof-of-concept single line link, the next step is to focus on multiple input multiple output (MIMO) transmission. Twisted pair communications networks are deployed in large twisted pair cable bundles (sometimes up to 100 pairs). MIMO transmission would consist in having signal launched on separate twisted pairs at the same time. This would be a challenge for surface waves specifically because of their large field extent, resulting in large crosstalk (vectoring can be a solution in this case). MIMO implementation would allow narrower bandwidth usage for higher total data rates.

Furthermore as a part of the general project frame, a few questions remain unclear from the initial simulation, designs and experimental results. Amongst those, single or multiple modes propagating in complex cable structures such as twisted pairs, the potential for through wall and underground applications (and how much it affects the transmission), surface wave field extent and interference complications being due only to mode conversion or to the actual line, surface wave transmission performance over higher frequency bands and scenarios with bends and irregularities and how to cope with them. Many of these factor will determine actual deployment scenarios and how usable surface waves are in in such scenarios. Some of the question are not so related to the data communication aspect of the research and will be covered mostly by the project collaborators.

Looking at the industrial side of the research some regulations will have to be considered. Such regulations would be whether surface waves fall under wireless transmission, therefore complying licence-free bands frequency and power. This would have to be tested experimentally and would again depend on the chosen operating frequency (may not be the case for higher frequencies such as mm-Waves).

Another major aspect is to test the transmission of SW transmission and differential mode transmission over the same link. The aim is to have technologies that would complement one another, similar to G.fast and VDSL operating on the same network but being used for different link lengths.

References

[1] M. Jackson, "Who is Building - UK Summary of Full Fibre Broadband Plans and Investment (update 9)," *ISPreview UK.*

[2] M. Timmers, M. Guenach, C. Nuzman, and J. Maes, "G.fast: Evolving the copper access network," *IEEE Communications Magazine*, no. 8, pp. 74–79.

[3] T. Karl Gärtner, "Data/Network Technology: Basic Knowledge including Network Dictionary." [Online]. Available: https://files.telegaertner.com/1914/6554/3695/DNT{_}Basic{_}Knowledge.pdf

[4] S. J. Orfanidis, *Electromagnetic Waves and Antennas*, Rutgers University, no. Rutgers University.

[5] L. Brillouin, *Wave propagation and group velocity.* Academic Press.

[6] C. R. Pollock and M. Lipson, "Dispersion in Waveguides," in *Integrated Photonics.* Springer US, ch. 6, pp. 125–148.

[7] T. Schaich, D. Molnar, A. Al Rawi, and M. Payne, "Analytic modelling of a planar Goubau line with circular conductor," *Scientific Reports*, no. 1, p. 20754, dec.

[8] UMaine, "Networking And Telecommunications - Lecture slides," nov 2009. [Online]. Available: https://www.slideshare.net/mgraham213/networking-and-telecommunications

[9] Ethernet Alliance, "2020 Ethernet Roadmap," 2020. [Online]. Available: https://ethernetalliance.org/technology/2020-roadmap/

[10] G. Lerude, "AT&T's Project AirGig Seeks Equipment Suppliers ," *Microwave Journal*, feb.

[11] J. M. Cioffi, K. J. Kerpez, C. S. Hwang, and I. Kanellakopoulos, "Terabit DSLs," *IEEE Communications Magazine*, vol. 56, no. 11, pp. 152–159, nov 2018.

[12] J. Proakis and M. Salehi, *Digital Communications Fifth Edition.* New York: McGraw-Hill.

[13] R. A. Thompson, D. Tipper, P. Krishnamurthy, and J. Kabara, *The Physical Layer of Communications Systems*, ser. Artech House telecommunications library. Artech House.

[14] J. D. Matyjas, F. Hu, and S. Kumar, *Wireless Network Performance Enhancement via Directional Antennas: Models, Protocols, and Systems.* CRC Press.

[15] MathWorks, "Decision Feedback Equalizer." [Online]. Available: https://www.mathworks.com/help/comm/ref/decisionfeedbackequalizer.html

[16] L. Frenzel, "Understanding Error Vector Magnitude," oct 2013. [Online]. Available: https://www.electronicdesign.com/resources/engineering-essentials/article/21799720/understanding-error-vector-magnitude

[17] T. Akalin, A. Treizebré, and B. Bocquet, "Single-wire transmission lines at terahertz frequencies," *IEEE Transactions on Microwave Theory and Techniques*, vol. 54, no. 6, pp. 2762–2767, 2006.

[18] D. G. Kiely, "Experiments With Single-Wire Transmission Lines At 3-Cm Wavelength *," *Journal of the British Institution of Radio Engineers*, no. 4, pp. 194–199, apr.

[19] B. W. B. W. Griffith, *Radio-electronic transmission fundamentals.* Noble Pub. Corp.

[20] G. Goubau, "Single-Conductor Surface-Wave Transmission Lines," *Proceedings of the IRE*, 1951.

[21] A. P. King, "The Radiation Characteristics of Conical Horn Antennas," *Proceedings of the IRE*, vol. 38, no. 3, pp. 249–251, 1950.

[22] C. A. Balanis, *Antenna Theory: Analysis and Design*, 2012.

[23] G. J. E. GOUBAU, "Surface wave transmission line," 1954. [Online]. Available: https://patentimages.storage.googleapis.com/d3/2b/48/4ddca159384a2f/US2685068.pdf

[24] A. Sharma, A. T. Hoang, and M. S. Reynolds, "A Coplanar Vivaldi-Style Launcher for Goubau Single-Wire Transmission Lines," *IEEE Antennas and Wireless Propagation Letters*, vol. 16, pp. 2955–2958, 2017.

[25] G. Elmore, "Single conductor surface wave transmission line system for terminating E field lines at points along the single conductor," pp. 2762–2767.

[26] ——, "Introduction to the Propagating Wave on a Single Conductor," Tech. Rep.

[27] S. Kotethota, G. Hada, P. Ramaswamy, and D. Gope, "Feasibility of single wire communication for PCB-level interconnects," in *2017 IEEE 21st Workshop on Signal and Power Integrity, SPI 2017 - Proceedings*. IEEE, may, pp. 1–4.

[28] R. N. Simons, *Coplanar Waveguide Circuits, Components, and Systems.*

[29] A. Treizebré, T. Akalin, and B. Bocquet, "Planar excitation of goubau transmission lines for THz BioMEMS," *IEEE Microwave and Wireless Components Letters*, vol. 15, no. 12, pp. 886–888, 2005.

[30] A. K. Horestani, W. Withayachumnankul, A. Chahadih, A. Ghaddar, M. Zehar, D. Abbott, C. Fumeaux, and T. Akalin, "Metamaterial-Inspired Bandpass Filters for Terahertz Surface Waves on Goubau Lines," *IEEE Transactions on Terahertz Science and Technology*, no. 6, pp. 851–858, nov.

[31] N. Tevar, P. Mehta, and K. Bhatt, "A review paper on conical corrugated horn antenna," in *Proceedings of the 2016 IEEE International Conference on Wireless Communications, Signal Processing and Networking, WiSPNET 2016*, 2016.

[32] M. N. Alam, R. H. Bhuiyan, R. Dougal, and M. Ali, "Novel surface wave exciters for power line fault detection and communications," in *IEEE Antennas and Propagation Society, AP-S International Symposium (Digest)*. IEEE, jul, pp. 1139–1142.

[33] L. Chusseau and J.-P. Guillet, "Coupling and Propagation of Sommerfeld Waves at 100 and 300 GHz," *J Infrared Milli Terahz Waves*, pp. 174–182.

[34] K. Wang and D. M. Mittleman, "Guided propagation of terahertz pulses on metal wires," *Journal of the Optical Society of America B*, pp. 2001–2007, 2005.

[35] T.-i. I. Jeon, J. Zhang, and D. Grischkowsky, "THz Sommerfeld wave propagation on a single metal wire," *Applied Physics Letters*, vol. 86, no. March, 2005.

[36] Y. B. Ji, E. S. Lee, J. S. Jang, T.-I. I. Jeon, Y. Bin Ji, E. Su Lee, J. Seok Jang, and T.-I. I. Jeon, "Enhancement of the detection of THz Sommerfeld wave using a conical wire waveguide," *Optics Express*, vol. 16, no. 1, pp. 271–278, 2008.

[37] Z. Wang, Y. Zhang, R. Xu, and W. Lin, "Accurate calculation of terahertz attenuation of a dielectric-coated metal wire with an intervening air gap using the engineering approach," *OPTICS*, pp. 3990–3995.

[38] J. Zha, G. J. Kim, and T.-I. Jeon, "Enhanced THz guiding properties of curved two-wire lines," *Optics Express*, no. 6, pp. 6136–6144.

[39] A. Markov, H. Guerboukha, T. Ma, and M. Skorobogatiy, "Hybrid metal-dielectric THz fibers design and perspectives - A Markov," *2014 39th International Conference on Infrared, Millimeter, and Terahertz waves (IRMMW-THz)*, pp. 1–3, sep.

[40] British Cables Company, "Datasheet for Dropwire 11." [Online]. Available: http://britishcablescompany.com/wp-content/uploads/2019/04/BCC-Dropwire-11.pdf

[41] Rohde and Schwarz, "R&S ZVA vector network analyzer - ZVA67." [Online]. Available: https://www.rohde-schwarz.com/hk/products/test-and-measurement/network-analyzers/rs-zva-vector-network-analyzer_63493-9660.html

[42] Keysight Technologies, "The RF/Microwave Signal Chain," Tech. Rep., may 2016. [Online]. Available: https://slideplayer.com/slide/13644976/

[43] Anritsu, “Understanding spectrum & signal analysis,” 2013, Tech. Rep., sep. [Online]. Available: https://www.academia.edu/11834728/Anritsu_Understanding_spectrum_signal_analysis

[44] Keysight Technologies, “VMA Vector Modulation Analysis X-Series Measurement Application, Multi-Touch,” Keysight Technologies, Tech. Rep., dec 2017. [Online]. Available: www.keysight.com/find/X-Series_trial

[45] Tektronix, “AWG70000B Series Datasheet.” [Online]. Available: https://www.tek.com/datasheet/arbitrary-waveform-generators-2

[46] Keysight, “DSOS404A High-Definition Oscilloscope: 4 GHz, 4 Analog Channels.” [Online]. Available: https://www.keysight.com/gb/en/support/DSOS404A/high-definition-oscilloscope-4-ghz-4-analog-channels.html#drivers

[47] M. Grzeskowiak, J. Emond, and G. Lissorgues, “Coplanar-Pgl Transitions on High Resistivity Silicon Substrate in the 57-64 GHz Band and Influence of the Probe Station on the Performances,” *Progress In Electromagnetics Research*, no. Ea 2552, pp. 79–87.

[48] T. Antonakopoulos and N. Papandreou, “Bit and power allocation in constrained multicarrier systems: The single-user case,” *Eurasip Journal on Advances in Signal Processing*, vol. 2008, p. 14, 2008.

[49] T. M. Schmidl and D. C. Cox, “Robust frequency and timing synchronization for OFDM,” *IEEE Transactions on Communications*, vol. 45, no. 12, pp. 1613–1621, 1997.

[50] IEEE Standards Association, “IEEE Standard for Ethernet Amendment 4: Physical Layer Specifications and Management Parameters for 1 Gb/s Operation over a Single Twisted-Pair Copper Cable,” *IEEE Std 802.3bp-2016 (Amendment to IEEE Std 802.3-2015 as amended by IEEE Std 802.3bw-2015, IEEE Std 802.3by-2016, and IEEE Std 802.3bq-2016)*, pp. 1–211.

[51] IEEE Standard Association, “IEEE Standard for Information Technology - Telecommunications and information exchange between systems - Local and Metropolitan Area Networks - Part 3: Carrier Sense Multiple Access with Collision Detection (CSMA/CD) Access Method and Physical Layer Specifications - Physical Layer Parameters and Specifications for 1000 Mb/s Operation over 4 pair of Category 5 Balanced Copper Cabling, Type 1000BASE-T,” *IEEE Std 802.3ab-1999*, pp. 1–144.

[52] IEEE Standards Association, “ISO/IEC/IEEE International Standard for Ethernet Amendment 7: Media Access Control Parameters, Physical Layers, and Management Parameters for 2.5 Gb/s and 5 Gb/s Operation, Types 2.5GBASE-T and 5GBASE-T,” *ISO/IEC/IEEE 8802-3:2017/Amd.7:2017(E)*, pp. 1–188.

[53] G. B. Ungerboeck, “10GBASE - T : 10Gbit / s Ethernet over copper,” in *NEWCOM-ACoRN Joint Workshop*, Vienna, 2006.

[54] IEEE Standards Association, “ISO/IEC/IEEE International Standard for Ethernet Amendment 3: Physical Layer and Management Parameters for 25 Gb/s and 40 Gb/s Operation, Types 25GBASE-T and 40GBASE-T.” *IEEE Std 802.3bq-2016 (Amendment to IEEE Std 802.3-2015 as amended by IEEE Std 802.3bw-2015, and IEEE Std 802.3by-2016)*, pp. 1–211.

[55] S. Ghosh, “BT quietly drops 25% fibre-to-the-premises target,” *Alphr.*

[56] R. Fontana, A. Nuvolari, and B. Verspagen, “Mapping technological trajectories as patent citation networks. An application to data communication standards,” *Economics of Innovation and New Technology*, no. 4, pp. 311–336.

[57] International Telecommunications Union (ITU), “ITU-T G.992.5 - Asymetric Digital Subscriber Line (ADSL) tranceivers – Extended bandwidth ADSL2 (ADSL2+),” Tech. Rep., 2005.

[58] ——, “ITU-T G.993.2 - Very high speed digital subscriber line transceivers 2 (VDSL2),” Tech. Rep., 2019.

[59] Y. Zhang, R. Zhang, J. Zhang, T. Bai, A. F. Al Rawi, M. Moonen, and L. Hanzo, “Far-end crosstalk mitigation for future wireline networks beyond G.mgfast: A survey and an outlook,” *IEEE Access*, vol. 8, pp. 9998–10 039, 2020.

[60] International Telecommunications Union (ITU), "ITU-T G.9700 - Fast access to subscriber terminals (G.fast) – Power spectral density specification," Tech. Rep., 2019.

[61] A. Sommerfeld, "Ueber die Fortpflanzung elektrodynamischer Wellen längs eines Drahtes," *Annalen der Physik*, no. 2, pp. 233–290, jan.

[62] J. C. Wiltse, "Surface-Wave Propagation on a Single Metal Wire or Rod at Millimeter-Wave and Terahertz Frequencies," *IEEE MTT-S International Microwave Symposium Digest*, pp. 970–973, 2006.

[63] R. B. Gary, "The "G-Line" Community TV System," *Radio & Television News*, pp. 40–41, nov.

[64] J. S. A. Cioffi, K. Kerpez, C. S. Hwang, and I. Kanellakopoulos, "Terabit DSL (TDSL) (Use of a copper pair's sub-millimeter Waveguide modes) (ASSIA)," in *G.fast Conference*, Paris, 2017.

[65] AT&T, "AT&T Labs' Project AirGig Nears First Field Trials for Ultra-Fast Wireless Broadband Over Power Lines."

[66] P. S. Henry, R. Bennett, F. Barzegar, I. Gerszberg, D. J. Barnickel, and I. Thomas M. Willis, "Method and apparatus for adjusting a field of a signal to mitigate interference."

[67] T. Akalin, A. Treizebre, and B. Bocquet, "High resolution biosensor based on surface wave transmission lines at THz frequencies," in *European Microwave Conference*, vol. 2, 2005, p. 4 pp.

[68] H. Barlow and A. Cullen, "Surface waves," *Proceedings of the IEE-Part III: Radio and Communication Engineering*, vol. 100, no. 68, pp. 329–341, 1953.

[69] G. Goubau, "Surface Waves and Their Application to Transmission Lines," *Journal of Applied Physics*, vol. 21, pp. 1119–1128, 1950.

[70] F. Harms, "Elektromagnetische Wellen an einem Draht mit isolierender zylindrischer H??lle," *Annalen der Physik*, no. 6, pp. 44–60, jan.

[71] M. J. King and J. C. Wiltse, "Surface-Wave Propagation on Coated or Uncoated Metal Wires at Millimeter Wavelengths," *IRE Transactions on Antennas and Propagation*, vol. 10, no. 3, pp. 246–254, 1962.

[72] International Telecommunications Union (ITU), "ITU-T G.652 Characteristics of a single-mode optical fibre and cable," Geneva, Tech. Rep.

[73] G. Zheng, J. Papapolymerou, and M. M. Tentzeris, "Wideband Coplanar Waveguide RF Probe Pad to Microstrip Transitions without via Holes," *IEEE Microwave and Wireless Components Letters*, vol. 13, no. 12, pp. 544–546, 2003.

[74] R. G. Bosisio and Y. Xu, "A comprehensive study on the planar type of Goubau line for millimetre and submillimetre wave integrated circuits," *IET Microwaves, Antennas & Propagation*, no. 3.

[75] W.-C. Chen, J. J. Mock, D. R. Smith, T. Akalin, and W. J. Padilla, "Controlling Gigahertz and Terahertz Surface Electromagnetic Waves with Metamaterial Resonators," *Physical Review X*.

[76] Y. Xu and R. G. Bosisio, "A study of planar goubau lines (PGLs) for millimeter- And submillimeter-wave integrated circuits (ICs)," *Microwave and Optical Technology Letters*, vol. 43, no. 4, pp. 290–293, 2004.

[77] L. Goleniewski and K. W. Jarrett, "Traditional Transmission Media for Networking and Telecommunications," in *Telecommunications Essentials, Second Edition: The Complete Global Source*, ch. 2, p. 928.

[78] IEEE Standards Association, "Standard for Information Technology - Telecommunications and Information Exchange Between Systems – LAN/MAN - Specific Requirements Part 3: CSMA/CD Access Method and Physical Layer Specifications - Amendment: Physical Layer and Management Parameters for 1," *IEEE Std 802.3an-2006 (Amendment to IEEE Std 802.3-2005*, pp. 1–181.

[79] K. Wang and D. M. Mittleman, "Metal wires for terahertz wave guiding," *Nature*, vol. 432, no. November, pp. 376 – 379, 2004.

[80] AT&T, "AT&T's Project AirGig Gets Closer to Commercial Deployment," sep 2018. [Online]. Available: https://about.att.com/story/2018/airgig.html

[81] T. M. Henry, Paul Shala and Vannucci, Giovanni and Willis III, "Methods and apparatus for exchanging wireless signals utilizing electromagnetic waves having differing characteristics."

[82] F. Barzegar, I. Gerszberg, T. M. Willis III, P. S. Henry, R. Bennett, D. J. Barnickel, and G. Vannucci, "Surface wave communication system and methods for use therewith," jul.

[83] R. Shrestha, K. Kerpez, C. S. Hwang, M. Mohseni, J. Cioffi, and D. M. Mittleman, "Two-wire waveguide for terabit DSL," in *Optics InfoBase Conference Papers*.

[84] LitePoint, San Jose, Tech. Rep.

[85] Y. B. Ji, E. S. Lee, J. S. Jang, T.-I. Jeon, M. H. Kwak, K.-Y. Kwang, Y. Bin Ji, E. Su Lee, J. Seok Jang, T.-I. Jeon, M. Hwan Kwak, and K.-Y. Kwang, "Guidance Properties of Metal Wire Waveguide by Terahertz Pulse Propagation," *Journal of the Korean Physical Society*, vol. 50, no. 5, pp. 1238–1242, 2007.

[86] J. S. Jo and T. I. Jeon, "Characteristics of THz pulse propagation on Teflon covered two-wire lines," *Journal of the Optical Society of Korea*, vol. 19, no. 6, pp. 560–565, 2015.

[87] M. G. Schorr and F. J. Beck, "Electromagnetic Field of the Conical Horn," *Journal of Applied Physics*, no. 8, pp. 795–801, aug.

[88] N. A. Aboserwal, C. A. Balanis, and C. R. Birtcher, "Conical horn: Gain and amplitude patterns," *IEEE Transactions on Antennas and Propagation*, no. 7, pp. 3427–3433.

[89] M. Cohn and M. J. King, "Excitation of the Sommerfeld Wave by a Uniform Magnetic Ring Source," *IEEE Transactions on Antennas and Propagation*, no. 5, pp. 651–653, sep.

[90] N. Alam, S. Member, R. H. Bhuiyan, R. A. Dougal, S. Member, and M. Ali, "Design and Application of Surface Wave Sensors for Nonintrusive Power Line Fault Detection," *Ieee Sensors Journal*, vol. 13, no. 1, pp. 339–347, 2013.

[91] S. M. Amjadi and K. Sarabandi, "A compact single conductor transmission line launcher for telemetry in borehole drilling," *IEEE Transactions on Geoscience and Remote Sensing*, vol. 55, no. 5, pp. 2674–2681, 2017.

[92] M. Gatti, H. Lin, E. Long, J. Sosnowski, and V. Jamnejad, "A test-bed validation of electromagnetic surface wave propagation along a dielectric-coated metal pipe," in *IEEE Aerospace Conference Proceedings*. IEEE, mar, pp. 1–13.

[93] X.-Y. He, "Investigation of terahertz Sommerfeld wave propagation along conical metal wire," *Journal of the Optical Society of America B*, no. 9, p. A23, sep.

[94] G. Goubau, "Open Wire Lines," *IRE Transactions on Microwave Theory and Techniques*, 1956.

[95] H. Pahlevaninezhad and T. E. Darcie, "Coupling of terahertz waves to a two-wire waveguide," *Optics Express*, no. 22, p. 22614.

[96] H. Gao, Q. Cao, D. Teng, M. Zhu, and K. Wang, "Perturbative solution for terahertz two-wire metallic waveguides with different radii," *Optics Express*, no. 21, p. 27457.

[97] D. Molnar, T. Schaich, A. Al-Rawi, and M. Payne, "Interaction between surface waves on wire lines," *Proceedings of the Royal Society A: Mathematical, Physical and Engineering Sciences*, no. 2246, p. 20200795, feb.

[98] M. K. Mridha, A. Mazhorova, M. Clerici, I. Al-Naib, M. Daneau, X. Ropagnol, M. Peccianti, C. Reimer, M. Ferrera, L. Razzari, F. Vidal, and R. Morandotti, "Active terahertz two-wire waveguides," *Optics Express*, no. 19, p. 22340.

[99] M. Mbonye, R. Mendis, and D. M. Mittleman, "A terahertz two-wire waveguide with low bending loss," *Applied Physics Letters*, vol. 95, no. 23, pp. 1–4, 2009.

[100] J. S. Jo, T. I. Jeon, and D. R. Grischkowsky, "Prototype 250 GHz bandwidth chip to chip electrical interconnect, characterized with ultrafast optoelectronics," *IEEE Transactions on Terahertz Science and Technology*, vol. 3, no. 4, pp. 453–460, 2013.

[101] A. M. Hejazi, G. J. Stockman, Y. Lefevre, V. Ginis, and W. Coomans, "Calculating Millimeter-Wave Modes of Copper Twisted-Pair Cables Using Transformation Optics," *IEEE Access*, vol. 9, pp. 52 079–52 088, 2021.

[102] Rohde and Schwarz, "R&S SMW200A vector signal generator." [Online]. Available: https://www.rohde-schwarz.com/uk/products/test-and-measurement/vector-signal-generators/rs-smw200a-vector-signal-generator_63493-38656.html

[103] ——, "R&S FSQ Signal Analyzer ." [Online]. Available: https://www.rohde-schwarz.com/us/product/fsq-productstartpage_63493-7994.html

[104] ——, "R&S SMIQ Vector Signal Generator." [Online]. Available: https://www.rohde-schwarz.com/us/product/smiq-productstartpage_63493-7561.html

[105] Anritsu, "Vector Signal Generator MG3710A." [Online]. Available: https://www.anritsu.com/en-us/test-measurement/products/mg3710a

[106] ——, "Signal Analyzers MS2690A." [Online]. Available: https://www.anritsu.com/en-us/test-measurement/products/ms2690a

[107] Teledyne LeCroy, "Teledyne LeCroy - WavePro 804HD." [Online]. Available: https://teledynelecroy.com/oscilloscope/wavepro-hd-oscilloscope/wavepro-804hd

[108] E. Sayre, M. Baxter, and J. Chen, "Limits of FR-4 in High-Speed Designs," NESA, Dallas, Tech. Rep., jan.

[109] P. Puttaswamy, P. K. S. Murthy, and B. A. Thomas, "Analysis of loss tangent effect on Microstrip antenna gain," *International Journal of Applied Science and Engineering Research*, no. 6, pp. 1102–1107.

[110] J. M. Cioffi, "A multicarrier primer," *ANSI T1E1*, vol. 4, pp. 91–157.

[111] V. Oksman, R. Strobel, T. Starr, J. Maes, W. Coomans, M. Kuipers, E. B. Tovim, and D. Wei, "MGFAST: A New Generation of Copper Broadband Access," *IEEE Communications Magazine*, vol. 57, no. 8, pp. 14–21, aug 2019.

[112] Ofcom, "Ofcom UK Spectrum Map." [Online]. Available: http://static.ofcom.org.uk/static/spectrum/map.html

[113] OFCOM, "Release of the 59 – 64 GHz band," Tech. Rep. December, sep 2009. [Online]. Available: https://www.ofcom.org.uk/consultations-and-statements/category-1/59_64ghz

[114] S. Bicheno, "Ofcom wants 57-71 GHz band to be free for fixed wireless," jul 2018. [Online]. Available: https://telecoms.com/490698/ofcom-wants-57-71-ghz-band-to-be-free-for-fixed-wireless/

[115] A. Leke and J. Cioffi, "A maximum rate loading algorithm for discrete multitone modulation systems," in *GLOBECOM 97. IEEE Global Telecommunications Conference. Conference Record.* IEEE, pp. 1514–1518.

[116] B. Powell and E. Harstead, "FEC Selection for 25G/50G/100G EPON," Tech. Rep., 2017. [Online]. Available: http://grouper.ieee.org/groups/802/3/ca/email/pdfeaRSFFdtqi.pdf

[117] S. M. Zafaruddin, I. Bergel, and A. Leshem, "Signal Processing for Gigabit-Rate Wireline Communications: An Overview of the State of the Art and Research Challenges," *IEEE Signal Processing Magazine*, vol. 34, no. 5, pp. 141–164, 2017.

[118] K. Zhan, A. Agrawal, M. Johnson, A. Ramachandran, T. Anand, and A. Natarajan, "An integrated 7-Gb/s 60-GHz communication link over single conductor wire using sommerfeld wave propagation in 65-nm CMOS," in *IEEE MTT-S International Microwave Symposium Digest.* IEEE, jun, pp. 797–800.

[119] S. Galli, J. Liu, and G. Zhang, "Bare metal wires as open waveguides, with applications to 5G," in *IEEE International Conference on Communications.* IEEE, may, pp. 1–6.

[120] D. D. Souza, B. P. Sousa, G. S. Borges, R. M. Rodrigues, A. M. Cavalcante, I. M. Almeida, and J. C. Costa, "Evaluation of Copper Cables as Waveguides in Next-generation Wireline Technologies," in *2019 SBMO/IEEE MTT-S International Microwave and Optoelectronics Conference, IMOC 2019.* Institute of Electrical and Electronics Engineers Inc., nov 2019.

Appendix

Ethernet alliance interface and nomencalture table naming explanation from figure 19

The naming of the standard in the form **"R mTYPE - L C n"** can be interpreted as [16]:
- **R**: data rate in Mb/s unless followed by a G when it becomes in Gb/s.
- **mTYPE**: in this case only "BASE" meaning it is a baseband transmission.
- **L**: medium types including wavelength and reach of the transmission: B $\rightarrow$ Bidirectional optics, C $\rightarrow$ Twin axial copper, D $\rightarrow$ Parallel single mode (500 m), E $\rightarrow$ Extra-long optical with λ 1510/1550 nm and reach 40 km, F $\rightarrow$ Fiber 2 km, K $\rightarrow$ Backplane, L $\rightarrow$ Long optical with λ 1310 nm and reach 10 km, P $\rightarrow$ Passive optics, RH $\rightarrow$ Red LED plastic optical fiber, S $\rightarrow$ Short optical with λ 850 nm and reach 100 m, T $\rightarrow$ Twisted pair.
- **C**: Physical coding sublayer (PCS) either R being scrambled coding or X external coding.
- **n**: number of lanes, if left blank only 1 lane.

Cascading ABCD-parameters for surface waves systems

ABCD-parameters, also known as cascading parameters, are used in transmission line theory for this very property. The rsulting ABCD-parameter of two cascaded RF systems can be calculated as follows:

$$\begin{bmatrix} A_3 & B_3 \\ C_3 & D_3 \end{bmatrix} = \begin{bmatrix} A_1 & B_1 \\ C_1 & D_1 \end{bmatrix} \cdot \begin{bmatrix} A_2 & B_2 \\ C_2 & D_2 \end{bmatrix} = \begin{bmatrix} A_1A_2 + B_1C_2 & A_1B_2 + B_1D_2 \\ C_1A_2 + D_1C_2 & C_1B_2 + D_1D_2 \end{bmatrix}$$

And also,

$$\begin{bmatrix} V_1 \\ I_1 \end{bmatrix} = \begin{bmatrix} A_3 & B_3 \\ C_3 & D_3 \end{bmatrix} \cdot \begin{bmatrix} V_3 \\ I_3 \end{bmatrix}$$

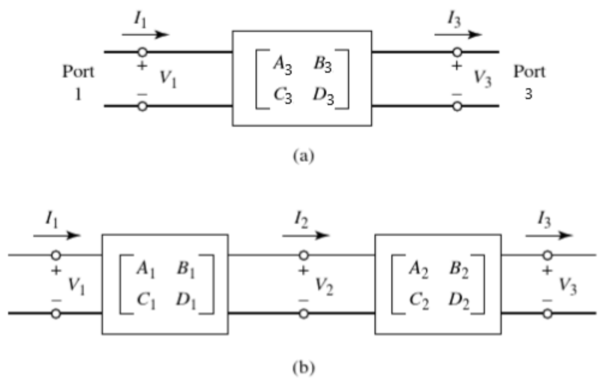

ABCD parameters a) overall link b) two cascaded links from Pozar, *Pozar, David M. Microwave Engineering. Chichester: Wiley, 2012.*

$$\begin{bmatrix} A_2 & B_2 \\ C_2 & D_2 \end{bmatrix} = \begin{bmatrix} A_3 & B_3 \\ C_3 & D_3 \end{bmatrix} \cdot \begin{bmatrix} A_1 & B_1 \\ C_1 & D_1 \end{bmatrix}^{-1}$$

In the case of this research, two S-parameters were measured for two links mostly similar except for the wire length. In the figure below, the long link is L_{long} converted from S to ABCD parameters, and the same was done for the short wire link L_{long}. Therefore the system is composed of a transmitting launcher L1, a wire L2 (long) or L3 (short) and a receiving launcher L1, identical to the transmitting one.

Following the theory from above, the ABCD parameter of the wire difference between long and short can be obtained as:

$$L_{long-short} = \left(\sqrt{L_{short}}\right)^{-1} \cdot L_{long} \cdot \left(\sqrt{L_{short}}\right)^{-1}$$

The ABCD parameter is then converted back to an S-parameter, and using the length difference an attenuation per unit length of the link can be calculated.

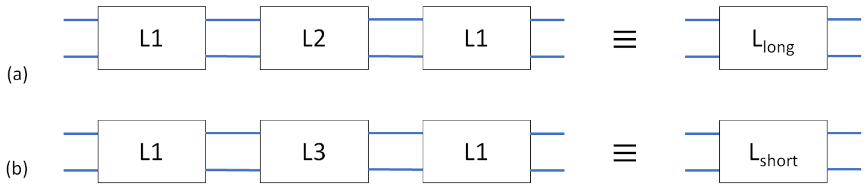

Graphical representation of the cascading ABCD parameters of a) the long wire SW link and b) the short wire SW link

Narrowband QAM transmission with R&S VSG and VSA

In the initial stage, different setups were attempted; the first one was using in-built data correction giving a very low EVM but unable to look at the actual BER as there could be some phase offset (however easily adjustable).

The first one was using in-built data correction giving a very low EVM but unable to look at the actual BER as there could be some phase offset (however easily adjustable).

This setup consisted in a combination of one of the Rohde & Schwarz vector signal generators (VSG) depending on the operating frequency, and the vector signal analyser from table 2.

Results on long planar link for QPSK to 64QAM and 8PSK at 2 Msym/s and 20 Msym/s and with a carrier frequency of 2.8 GHz (from 4 Mb/s to 120 Mb/s). There is a large difference between the best performance of both symbol rates, but all modulation levels have the same minimum EVM.

In a similar manner as before, showing results with the second VSG at f_c = 4 GHz with only QPSK and 64QAM on both the short and long planar links. With both having SR = 13 Msym/s, so a bit rate ranging from 26 Mb/s to 78 Mb/s. Both lengths have the same EVM min. In all cases, EVM low is reached from as low as Pin = - 30 dBm but such high performance can be expected from surface wave links of less than 50 cm.

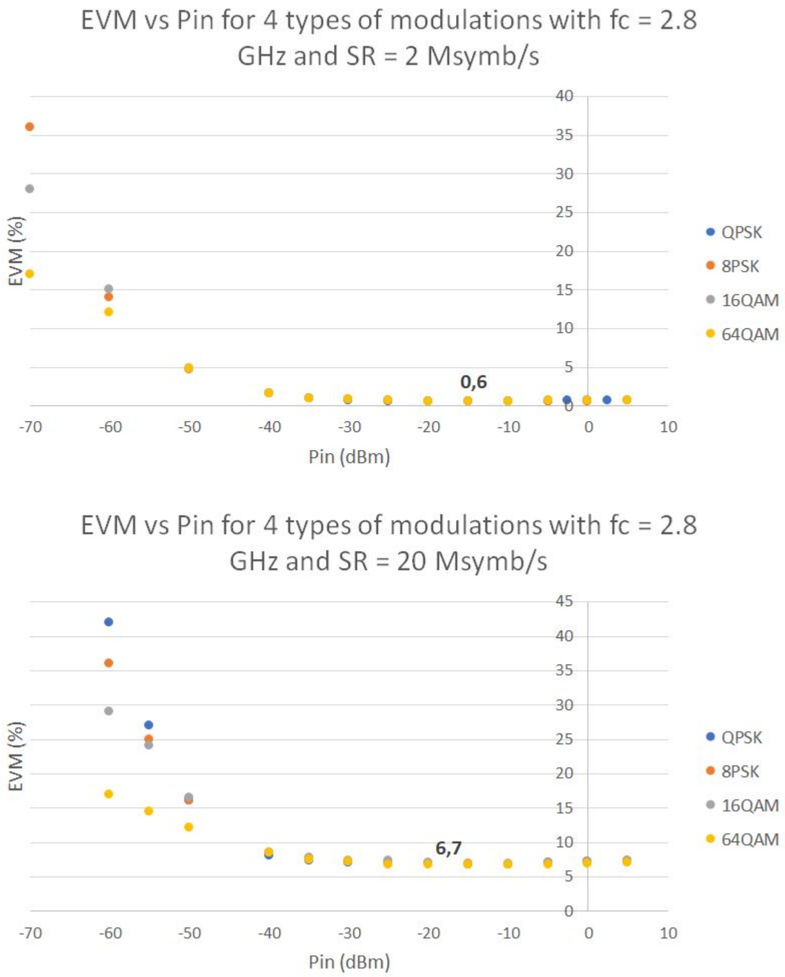

EVM against input power for different modulation schemes using VSG and VSA setup on long planar surface wave link

EVM against input power for different modulation schemes using VSG and VSA setup on long and short planar surface wave links

14.7 Gb/s transmission on a single frame with errors

$f_c = 2.1$ GHz with 2667 MHz bandwidth test on a Rogers antenna supplied by the Astophysics department group, The overall S21 response at low frequencies was worst than the FR4 antenna one, with higher attenuation but potentially a flatter response.

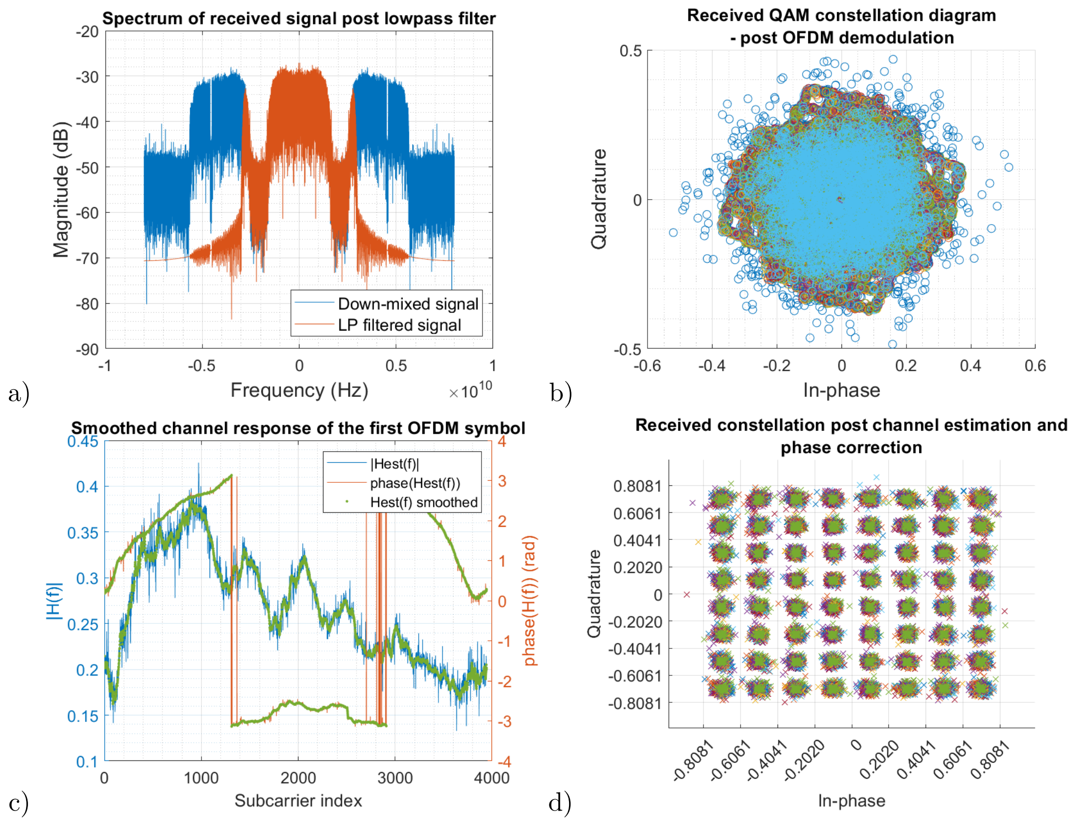

Results of the wideband high throughput 64 QAM dataset with a) the received down-mixed and LP filtered spectrum, b) the OFDM demodulated QAM constellation, c) the calculated channel response and d) the equalised QAM constellation

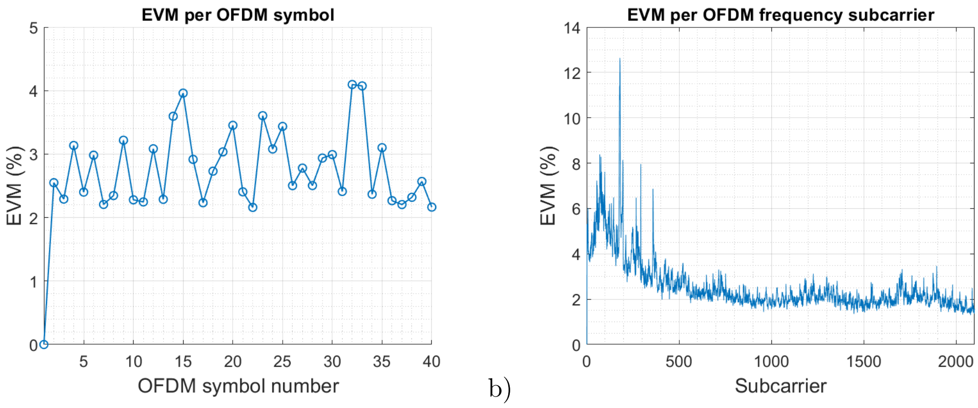

Figure 118: EVM characterisation of the 14.7 Gb/s 64 QAM transmission against a) the OFDM symbol number and b) the OFDM subcarrier

QAM	BW	NFFT	Fc	CP	Nulls	OH	evmtot	nb err	BER	DR post OH	err freq		
	MHz		GHz				%			b/s	MHz		
64	2667	4096	2.1	128	152	0.921319	4.28	94	9.68E-05	1.47E+10	854.4016	2400.168	3232.954
64	2667	4096	2.1	128	152	0.921319	2.73	17	1.75E-05	1.47E+10	804.2651	2399.517	3399.642
64	2667	4096	2.1	128	152	0.921319	2.81	37	3.81E-05	1.47E+10	816.6365	881.7488	2400.168

Table with detailled results

Extrapolation using S-parameters fitting on Simulink

A Simulink model was built to predict the behaviour of data transmission over SW link. The model is shown in the figure below with the different transmission blocks: Modulation, frequency upconversion, RF domain transmission, frequency downconversion, signal correction, demodulation and BER calculation.

The main particularity of this link is the RF domain block containing experimental measurements of surface wave S-parameters. In this block the experimental S-parameters are fitted in the time domain (using rationalfit function) to a defined number of poles. The number of poles defines the precision of the fitting, as well as a chosen fitting option.

This model can then emulate data transmission over a surface wave link using experimental S-parameters.

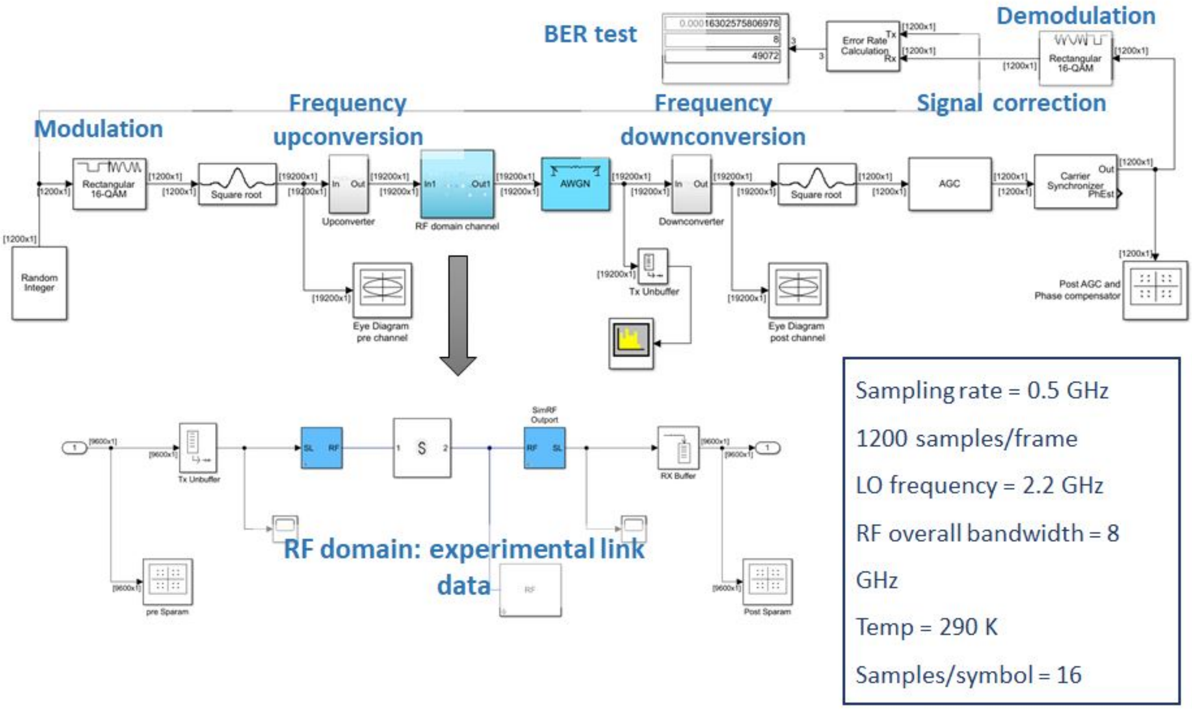

Simulink surface-wave transmission channel diagram

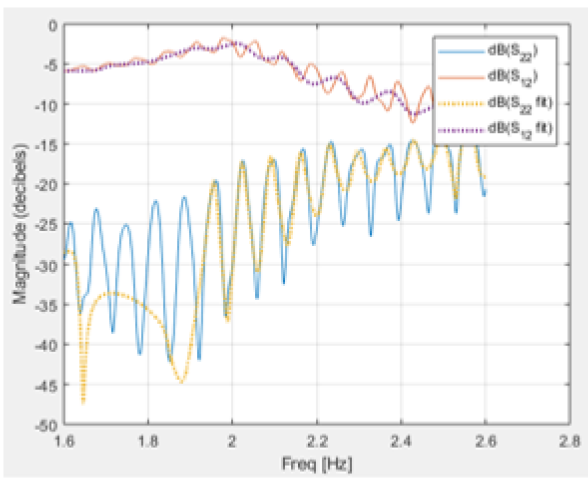

Fitting of the 2 m surface wave link's experimental S-parameter

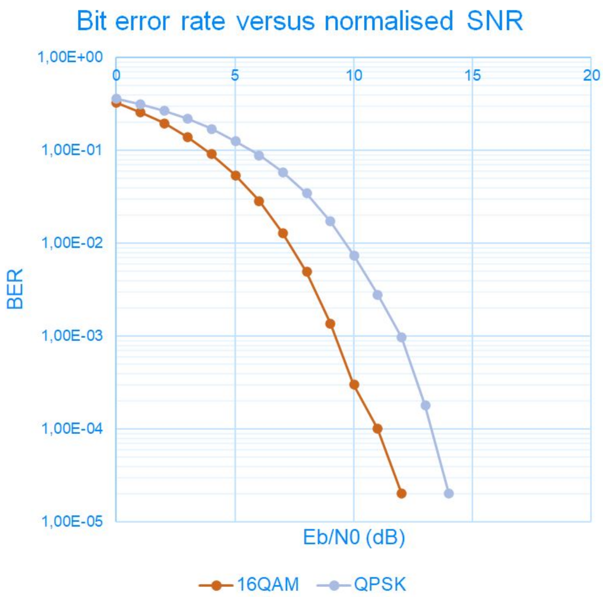

Bit error rate against normailised SNR for different modulations through Simulink channel